Cutting bubbles : an experimental and numerical investigation of micro-structured bubble column

Cutting Bubbles

An experimental and numerical investigation of micro-structured bubble column.

PROEFSCHRIFT

ter verkrijging van de graad van doctor aan de Technische Universiteit Eindhoven, op gezag van de rector magnificus, prof.dr.ir. F.P.T. Baaijens, voor een commissie aangewezen door het College voor Promoties, in het openbaar te verdedigen op dinsdag 1 november 2016 om 16.00 uur

door

Krushnathej Thiruvalluvan Sujatha

geboren te Tiruvallur, India

Dit proefschrift is goedgekeurd door de promotoren en de samenstelling van de promotie commissie is als volgt:

voorzitter:	prof.dr.ir. L.P.H. de Goey	
1^e promotor:	prof.dr.ir. N.G. Deen	
2^e promotor:	prof.dr.ir. J.A.M. Kuipers	
leden:	prof.Dr.-Ing.habil. U. Hampel	Technische Universität Dresden
	prof.dr. D. Lohse	Universiteit Twente
	prof.dr. R.F. Mudde	Technische Universiteit Delft
	prof.dr. J.G.M. Kuerten	
	prof.dr.ir. M. van Sint Annaland	

Het onderzoek dat in dit proefschrift wordt beschreven is uitgevoerd in overeenstemming met de TU/e Gedragscode Wetenschapsbeoefening.

To my family and friends

This dissertation is approved by the promotor:

prof.dr.ir. N.G. Deen

and
prof.dr.ir. J.A.M. Kuipers

The research reported in this thesis was financially supported by the European Research Council under the grant agreement no. 259521 (Cutting Bubbles).

Nederlandse titel: "Cutting Bubbles: Een experimentele en numerieke onderzoek van micro-gestructureerde bellenkolom."

Printed by: Gildeprint Drukkerijen, Enschede

Typeset using LaTeX

A catalogue record is available from the Eindhoven University of Technology Library
ISBN 978-90-386-4166-9
Author email: tskrushna@gmail.com

Table of contents

Summary

Cutting Bubbles: An experimental and numerical investigation of micro-structured bubble column

Bubbly flows are dispersed two-phase flows involving a gas and a liquid phase and are typical for the flow in a bubble column reactor. The gas is injected in the form of bubbles into a quiescent liquid in a cylindrical bubble column. Bubble columns are often encountered in the chemical industry, for instance in petrochemical, biochemical or pharmaceutical industry. They are the preferred type of reactors for gas-liquid contact owing to their simple design, ease of operation, good heat and mass transfer. However, bubble coalescence and back mixing often affect the performance of an industrial bubble column reactor. In this thesis, a novel micro-structured bubble column reactor is proposed to overcome the disadvantages of a conventional bubble column reactor. The micro-structuring is provided in the form of wire meshes. The wire meshes serve the purpose of cutting the large bubbles into smaller daughter bubbles, thereby increasing the interfacial area. The bubble cutting also results in an increase in the gas holdup due to an increase in residence time of the bubbles in the column. This work is a part of the ERC-funded project "Bubbles on the cutting edge", to investigate the proof of principle of a micro-structured bubble column (MSBC) equipped with wire mesh internals.

The configuration of the wire mesh is characterized by the wire diameter and the mesh opening or pitch. Non-intrusive experimental techniques such as digital image analysis, particle image velocimetry, oxygen concentration sensing and ultra-fast X-ray tomography are employed in this study. Different gas-liquid systems are investigated to characterize the performance of the MSBC reactor for physical absorption (air-water) and chemical absorption (carbon dioxide-sodium hydroxide). A detailed volume of fluid-discrete bubble model (VoF-DBM) model is employed for the simulation of MSBC reactor with bubble cutting for the case of chemisorption. The simulation results are compared with the experimental data in order to validate the VoF-DBM model.

Visual observation is an important method that is employed to identify the different flow regimes in a micro-structured bubble column. Three different hydrodynamic regimes are observed in the pseudo-2D MSBC for various mesh configurations in an air-water system and they are as follows: i) gas pocket formation below the mesh, ii) bubble cutting, iii) bubble cutting and re-coalescence. An advanced digital im-

age analysis based on shadowgraphy is used to distinguish individual bubbles in a cluster. Bubble size distribution is determined experimentally for a column with different mesh configurations and compared with the results obtained in a conventional bubble column without wire mesh. The bubble size distribution below and above the mesh is an important parameter that determines the efficiency of the wire mesh in a micro-structured bubble column. The bubble cutting is a function of wire diameter, mesh opening and superficial gas velocity. A small wire diameter and a mesh opening smaller than the average bubble size has good bubble cutting characteristics. The particle image velocimetry measurements show that the presence of a wire mesh generates liquid circulation cells above and below the mesh, thereby reducing liquid back-mixing. The wire mesh also enhances the bubble velocity fluctuations, that can favorably affect the mass transfer coefficient.

The physical absorption of oxygen from air into water is used to characterize the mass transfer performance of different mesh configurations. A non-intrusive planar optical oxygen sensor is used to determine the dissolved oxygen concentration in water. The response time of the optical sensor is determined to be 3 seconds. The mass transfer coefficient k_La of a single wire mesh (3.7 mm mesh opening) is shown to increase by 25% at a high superficial gas velocity of 40 mm/s. The wire mesh has a better performance than a dense Sulzer packing (SMV) at high superficial gas velocities, as it offers lower hydrodynamic resistance to the flow of bubbles. Low hydrodynamic resistance is essential for efficient cutting behavior and better performance in terms of the mass transfer.

The effect of the gas-liquid surface tension is investigated by performing experiments in a dodecane-nitrogen system instead of conventionally used air-water system. Pure dodecane has froth formation at the top due to the formation of small bubbles, as it is a non-coalescing system. Bubble cutting takes place even at low superficial gas velocity and small mesh openings due to the low surface tension in the dodecane-nitrogen system. This is markedly different from the air-water system, where a larger superficial gas velocity and mesh opening (3.7 mm) is required for bubble cutting. It is important to use industrial organic media in pilot plant studies, to obtain a better idea of the hydrodynamic behavior in such systems. Increasing the number of mesh stages in the MSBC changes the overall hydrodynamics of the system from the heterogeneous to a homogeneous regime. Hence, the use of multiple meshes enhances bubble cutting or breakup evident by the increase in gas holdup.

Chemisorption of CO_2 into $NaOH$ is a fast reaction limited by the mass transfer rate from the gas phase to the liquid. The time taken for neutralization of $NaOH$ is a strong indicator for the performance of the wire mesh. Experiments were performed in a pseudo-2D MSBC reactor for the chemisorption of CO_2 into $NaOH$. The Sulzer packing and a wire mesh with a 3.7 mm mesh opening show good cutting characteristics in terms of the resulting bubble size distribution. This increases the interfacial area in turn resulting in an increased gas holdup and better mass transfer performance. Since the chemisorption is mass transfer limited the reaction times decrease significantly in the presence of the internals. The multi-mesh configuration with six mesh stages is seen to have a better performance than a single mesh due to the enhanced bubble cutting and increased gas holdup. The performance of a

multi-mesh configuration with ten stages is hindered by the decrease in back-mixing and reduction in mass transfer due to bubble swarm effects. The volume of fluid-discrete bubble model (VoF-DBM) with bubble cutting model is validated with the experiments. The sub-model for bubble cutting has the major drawback that it is independent of the superficial gas velocity. Therefore, more work should be done to develop closures from direct numerical simulations (DNS) to improve the cutting model.

A micro-structured square bubble column reactor equipped with the 3.7 mm wire mesh, was investigated by using an ultra-fast X-ray tomography technique. The effect of superficial gas/liquid velocity on the hydrodynamics of the MSBC was investigated at different heights of the column. The bubble size distribution and the bubble velocity for different heights of the column is extracted by digital image analysis and cross-correlation respectively. The spatial and temporal resolution of X-ray tomography is sufficient to resolve details of the flow-structure, such as the presence of lamellar liquid films between the large bubbles after they pass through the wire mesh. The bubble cutting or breakup mainly occurs at high superficial gas velocity. The superficial liquid velocity does not have a significant effect on the bubble cutting. The bubble velocity obtained at different positions of the column show that the bubbles decelerate on approaching the mesh and accelerate after leaving the mesh.

The insights and the experimental results obtained in this work can be used to optimize bubble column reactors and to validate the Euler-Lagrange model for a laboratory scale bubble column reactor.

Samenvatting

Cutting Bubbles: An Experimental and numerical investigation of micro-structured bubble column

Bellenstromingen zijn gedispergeerde tweefasenstromingen van een gas en een vloeistof en zijn karakteristiek voor de stroming in een bellenkolom. Gas wordt geïnjecteerd in de vorm van bellen in een stilstaande vloeistof in een cilindrische kolom. Bellenkolommen worden veel gebruikt in de chemische industrie, bij voorbeeld in de petrochemische, biochemische of farmaceutische industrie. Dit type reactor heeft vaak de voorkeur om gassen en vloeistoffen met elkaar in contact te brengen, vanwege het eenvoudige ontwerp en operatie en goede warmte- en stofoverdracht. Daarentegen kunnen coalescentie van bellen en terugmenging de prestaties heeft van dit type reactor nadelig beïnvloeden. In dit proefschrift wordt een nieuw type micro-gestructureerde bellenkolom voorgesteld om de nadelen van conventionele bellenkolommen weg te nemen. De micro-structurering wordt aangebracht door middel van fijne draadroosters ("gaas"). De draadroosters hebben als doel om grote bellen in kleinere bellen te snijden, waarmee het gas-vloeistof contactoppervlak vergroot wordt. Het snijden van bellen leidt ook tot een hogere gasfractie vanwege de langere verblijftijd van bellen in de kolom. Dit werk maakt deel uit van een door de ERC gefinancierd project dat tot doel heeft om een 'proof-of-principle' te geven van een micro-gestructureerde bellenkolom (MSBC) voorzien van draadrooster internals.

De configuratie van het draadrooster wordt gekarakteriseerd door de diameter van de draad en de roosteropening of steek. Niet-intrusieve meettechnieken zijn toegepast in deze studie, zoals digitale beeld analyse, 'particle image velocimetry', zuurstof concentratie meting en ultrasnelle Röntgentomografie. Verschillende gas-vloeistof systemen zijn onderzocht om de prestaties van de MSBC reactor te karakteriseren voor de fysische absorptie (lucht-water) en chemische absorptie (kooldioxide-natronloog). Een gedetailleerd 'volume-of-fluid'-discrete bellen model (VoF-DBM) is gebruikt voor de simulatie van een MSBC reactor met inachtneming van het snijden van bellen voor de casus van chemisorptie. De simulatie resultaten zijn vergeleken met experimentele data om het VoF-DBM model te valideren.

Visuele observatie is een belangrijke methode voor het identificeren van verschillende stromingsregimes in een mictro-gestructureerde bellenkolom. Drie verschillen hydrodynamische regimes zijn geobserveerd in een pseudo-2D MSBC voor verscheidene rooster configuraties in een lucht-water systeem. Deze zijn als volgt: i) gas bubbel

vorming onder het rooster, ii) bel snijden, iii) bel snijden en hercoalescentie. Een geavanceerde digitale beeldanalyse gebaseerd op schaduwgrafie is gebruikt om bellen in een cluster te onderscheiden. De belgrootteverdeling is experimenteel bepaald voor een kolom met verschillende rooster configuraties en vergeleken met de resultaten van een conventionele bellenkolom zonder draadrooster. De belgrootteverdeling zowel onder als boven het rooster is ene belangrijke parameter die de efficiency van het draadrooster bepaald in een micro-gestructureerde bellenkolom. Het snijden van bellen hangt af van de draaddiameter, de roosteropening en de superficiële gassnelheid. Een kleine draaddiameter en een roosteropening kleiner dan de gemiddelde belgrootte hebben goede karakteristieken voor het snijden van bellen. De 'particle image velocimetry' metingen laten zien dat door de aanwezigheid van een draadrooster vloeistof circulatie cellen onder en boven het rooster worden gevormd, waardoor de terugmenging van vloeistof wordt beperkt. Het draadrooster vergroot ook snelheidsfluctuaties van de bellen, hetgeen de stofoverdrachtscoëfficiënt ten goede komt.

De fysische absorptie van zuurstof uit lucht naar water is gebruikt om de stofoverdrachtsprestaties van verschillende rooster configuraties te karakteriseren. Een niet-invasieve vlakke zuurstofsensor is gebruikt om de in water opgeloste zuurstofconcentratie te meten. De responstijd van de optische sensor is bepaald op 3 seconden. De stofoverdrachtscoëfficiënt k_La van een systeem met een enkel draadrooster (3.7 mm roosteropening) blijkt 25% toe te nemen bij een superficiële gassnelheid van 40 mm/s. Het draadrooster werkt beter dan een dichte Sulzer pakking (SMV) bij hoge superficiële gassnelheden, omdat het minder hydrodynamische weerstand oplevert voor een stroming met bellen. Een lage hydrodynamische weerstand is essentieel voor een het efficiënt opsnijden van bellen en voor de stofoverdrachtsprestaties.

Het effect van de gas-vloeistof oppervlaktespanning is onderzocht door experimenten uit te voeren voor een dodecaan-stikstof systeem in plaats van het conventionele lucht-water systeem. Gebruik van pure dodecaan leidt tot schuimvorming in de top vanwege de vorming van kleine bellen, doordat het systeem niet-coalescerend is. Het snijden van bellen vindt zelfs plaats bij lage superficiële gassnelheden en kleine roosteropeningen als gevolg van de lage oppervlaktespanning in het dodecaan-stikstof systeem. Dit is wezenlijk anders dan in een lucht-water systeem, waar een hogere superficiële gassnelheid en roosteropening (3.7 mm) nodig zijn om de bellen te snijden. Het is belangrijk om industriële stoffen te gebruiken in pilot-plant studies om een beter idee te krijgen van het hydrodynamisch gedrag in dergelijke systemen. Het gebruik van meerdere draadroosters bevordert het snijden en opbreken van bellen, hetgeen blijkt uit de toegenomen gasfractie.

Chemisorptie van CO_2 in $NaOH$ is een snelle reactie die wordt gelimiteerd door stoftransport van de gas- naar de vloeistoffase. De tijd benodigd voor de het neutraliseren van $NaOH$ is een sterke indicator voor de prestaties van het draadrooster. Experimenten zijn verricht in een pseudo-2D MSBC reactor voor de chemisorptie van CO_2 in $NaOH$. De Sulzer pakking en een draadrooster met een opening van 3.7 mm vertoont goede karakteristieken voor wat betreft de belgrootteverdeling. Dit verhoogt het contactoppervlak hetgeen leidt tot een hogere gasfractie en betere stofoverdracht. Aangezien de chemisorptie door stoftransport gelimiteerd is, reduceert de reactietijd significant in de aanwezigheid van internals. De configuratie met meerdere draadroos-

ters (zes roosters) blijkt betere prestaties te leveren dan een systeem met een enkel rooster, omdat meer bellen gesneden worden en de gasfractie toeneemt. De prestaties van een kolom met tien draadroosters wordt gehinderd door een afname van de terugmenging en een afname in stofoverdracht door zwermeffecten. Het 'volume-of-fluid'-discrete bellen model (VoF-DBM) met een belsnijmodel is gevalideerd met behulp van experimenten. Het belsnijmodel heeft het grote nadeel dat het afhangt van de superficiële gassnelheid. Nader onderzoek is daarom vereist voor het ontwikkelen van sluitingsrelaties uit directe numerieke simulaties (DNS) die tot een beter belsnijmodel leiden.

Een micro-gestructureerde bellenkolom reactor voorzien van een 3.7 mm draadrooster is onderzocht met een ultrasnelle Röntgentomografie techniek. Het effect van de superficiële gas/vloeistofsnelheid op de hydrodynamica in de MSBC is onderzocht op verschillende hoogtes in de kolom. De belgrootteverdeling en de belsnelheid op verschillende hoogtes in de kolom zijn respectievelijk bepaald aan de hand van digitale beeldanalyse en kruiscorrelatie. De spatiële en temporele resolutie van de Röntgentomografie is voldoende om de details van de stroming op te lossen, zoals de aanwezigheid van lamelachtige vloeistoffilms tussen grote bellen nadat ze het draadrooster gepasseerd zijn. Het snijden of opbreken van bellen treedt voornamelijk op bij hoge superficiële gassnelheid. Deze laatste heeft geen significant effect op het snijden van bellen. De belsnelheid verkregen op verschillende hoogtes in de kolom laat zien dat bellen decelereren zodra ze het rooster naderen en accelereren nadat ze het rooster verlaten hebben.

De inzichten en experimentele resultaten die verkregen zijn in dit werk kunnen worden gebruikt om bellenkolommen te optimaliseren en om het Euler-Lagrange model te valideren voor een lab schaal bellenkolom reactor.

CHAPTER 1

INTRODUCTION

1.1 Bubble column reactors

Bubble column reactors are simple cylindrical vessels used in the industry to achieve efficient contact between the gas and liquid phase. They are used in the chemical, biochemical, petrochemical, pharmaceutical, metallurgical industries for chlorination, alkylation, hydrogenation, oxygenation, flue-gas treatment, synthetic fuel production (e.g. Fischer Tropsch process) and biochemical processes such as fermentation and biological waste-water treatment. A conventional bubble column reactor consists of a vertical vessel with no internals. The gas is introduced from the bottom into a quiescent liquid phase. It is possible to feed liquid at the bottom or top of the bubble column and operate it in co-current or counter-current mode with respect to the gas flow.

On the basis of superficial gas velocity and column diameter, three distinct flow regimes are observed in bubble columns: homogeneous bubbly flow, heterogeneous/churn-turbulent flow and slug flow. The homogeneous regime is observed at low superficial gas velocities. This regime is characterized by uniform bubble size distribution and close to plug flow behavior in the gas phase as all the bubbles rise in the column. Bubble coalescence and breakup do not occur in this regime and the average bubble size is governed by the sparger design and the system properties. The heterogeneous flow regime occurs at high superficial gas velocities with large gas throughput. The turbulence induced by high velocities results in a wide bubble size distribution and formation of very large bubbles due to coalescence. The mean bubble size is controlled by the equilibrium between coalescence and breakup. This flow regime is of particular interest to the industry to enable high production rates and efficient operation. The slug flow regime can be seen in columns with small diameter, operated at high gas

velocity. This regime is evident by the intermittent occurrence of large bubble slugs occupying the entire cross section of the column. A detailed review of bubble column reactors can be found in the following articles: Shah et al. (1982); Baird (1992); Deen et al. (2000); Kantarci et al. (2005).

Bubble columns are generally applied for systems involving mass transfer i.e. from gas to liquid or liquid to gas phase. The efficiency of these reactors are mainly affected by the rate of mass transfer between the phases involved, due to high coalescence and back-mixing phenomena. The rate of mass transfer is proportional to the interfacial area, mass transfer coefficient and concentration gradient of a species between the gas and liquid phase. Therefore the mass transfer rate can be enhanced by increasing one or more of the relevant parameters. A novel micro-structured bubble column (MSBC) is proposed to overcome the drawbacks and enhance the mass transfer rate. The applied micro-structuring is a wire-mesh that can be placed at various heights in a multi-stage configuration. The wire mesh in the MSBC serves the purpose of cutting large bubbles into smaller bubbles, leading to higher interfacial area. Since small bubbles have lower rise velocities, the residence time of the bubbles is also increased. The MSBC configuration with wire mesh is promising over conventional trays or packings, as it is expected to offer lower pressure drop due to its open structure. The MSBC reactor concept is mainly useful for systems with fast reaction limited by gas-liquid mass transfer. It is important to demonstrate the proof-of-principle in a small laboratory scale MSBC reactor and fully understand the MSBC reactor concept. An introduction to different experimental techniques and the multi-scale simulation strategy can be found in sections 1.2 and 1.3 respectively.

1.2 Experimental techniques for multiphase flows

Several experimental techniques have been developed to study the characteristics of multiphase flows in gas-liquid, gas-solid and gas-liquid-solid reactors; for e.g. bubble columns, fluidized bed reactors and slurry bubble columns respectively. Experiments are required to obtain information on the local and global quantities such as bubble size (distribution), gas holdup, interfacial area, pressure drop, velocity, dispersion coefficient, mass/heat transfer coefficient, pH, temperature, concentration, flow regime and mixing behavior. Reliable experimental techniques are necessary to enable better understanding of the complex behavior of multiphase reactors. They are important for the development of empirical correlations for industrially relevant conditions and also for the validation of advanced computational fluid dynamics (CFD) models. The study of multiphase flows is quite complex due to the large range of length and time scales occurring in these flows. Therefore, it is important to choose an experimental technique with adequate resolution to study the parameter of interest. Experimental techniques can be classified based on the following methods: i) resolution in space (local, global) and time (time-averaged, transient) and ii) intrusiveness of the measurement (invasive or non-invasive). Amongst these techniques, non-invasive methods are of particular interest for lab scale studies because they can extract information without altering the flow characteristics. Even though intrusive methods interfere with the flow they have the advantage that they can be applied to industrial condi-

Technique	results	spatial resolution	intrusiveness
X-ray tomography, wire mesh sensor, electrical capacitance tomography	bubble size bubble velocity gas holdup	cross-section	non-invasive invasive non-invasive
photography and digital image analysis	bubble size bubble velocity gas holdup	2D/3D	non-invasive
magnetic resonance imaging	liquid velocity gas holdup		
particle image velocimetry	liquid velocity bubble velocity		
4-point optical probe	bubble velocity bubble size	local	invasive
laser doppler anemometry	liquid velocity		non-invasive
phase doppler anemometry	liquid velocity bubble size bubble velocity		non-invasive
conductivity probe	dispersion coefficient		invasive
pH probe	pH, concentration		invasive
oxygen probe	concentration		non-invasive
infrared camera	temperature		non-invasive

Table 1.1: An overview of experimental methods for bubbly flows

tions (for e.g. high gas holdups, opaque reactor walls), in contrast to non-intrusive techniques based on optical imaging. A brief overview of experimental methods used for bubbly flow is presented in Table 1.1. For a detailed review of measurement techniques, we refer to Chaouki et al. (1997); Boyer et al. (2002); Powell (2008).

1.3 Numerical modeling

A multi-scale modeling strategy is employed to investigate the large length and time scales involved in multiphase reactors. In this strategy, the smaller scale models provide closures for larger scale models, to enable accurate representation of small scale phenomena in coarse-grained models with reasonable computational effort. In this multi-scale strategy the smallest scales are modeled by direct numerical simulations (DNS). Volume of fluid (VoF), front tracking (FT), immersed boundary methods

(IBM) and level-set (LS) methods are some examples of the DNS models applied to study bubbly flows. In DNS models, all details of the flow are resolved using Navier-Stokes equations based on first principles without any prior assumptions. However, the models are restricted to a maximum of $\mathcal{O}(100)$ bubbles due to high computational costs.

Euler-Lagrange models or discrete bubble models (DBM) are available to simulate the intermediate scales. These models solve the volume-averaged Navier-Stokes equations for the liquid phase in Eulerian domain and track the bubbles in a Lagrangian domain based on the Newtonian equations of motion. The various force closures necessary for the model are provided by empirical correlations or DNS studies. Turbulence is modeled using a sub-grid scale turbulence model by means of defining a turbulent viscosity (i.e. Smagorinsky or Vreman model). Collisions between bubble-bubble and bubble-wall are tracked explicitly. Since the bubbles are treated individually in the DBM, bubble coalescence and breakup can also be processed easily based on theoretical models. These models are useful to simulate laboratory scale bubble columns with $\mathcal{O}(10^6)$ bubbles but are nowhere near to handle the computational demand of modeling industrial scales, which contain $\mathcal{O}(10^8 - 10^{10})$ bubbles.

The largest scales are described by using an Euler-Euler model or two fluid model (TFM). In this model both the liquid and gas are modeled as inter-penetrating continuum and their motion is solved using coupled momentum equations. Since the bubbles are treated as continuous phase the interactions between bubble-bubble, bubble-wall and bubble-liquid are not captured by this model. Therefore closure relations developed from DBM and DNS studies are necessary to describe these interactions. TFM is computationally least expensive and hence can be used to model industrial scale bubble columns.

1.4 Objectives and outline

The importance of developing a novel MSBC reactor was discussed in section 1.1. The European Research Council (ERC) project "Cutting Bubbles" includes the study of the MSBC by means of a combined multi-scale experiment and simulation approach. Segers et al. (2013) used an immersed boundary method to develop a drag correlation for liquid flow past crossing cylinders inside a wire-mesh. Segers (2015) also used a combined IBM-VoF model to investigate bubble cutting in cylindrical wires. Baltussen (2015) has studied the effect of a single bubble being cut by a wire and a wire mesh using a volume of fluid (VOF) method of van Sint Annaland et al. (2003). The simulations of single bubble cutting in a cylindrical wire is validated by experiments performed in a glycerol-water mixture with air bubbles. Jain et al. (2013) also performed simulations to study bubble cutting in an air-water system. Jain et al. (2015) incorporated the drag model of Segers et al. (2013) in a hybrid volume of fluid-Euler-Lagrange model to study bubble cutting in a laboratory scale MSBC reactor with chemisorption. The objective of the work presented in this thesis is to perform detailed experiments to verify the proof-of-principle and to validate the VoF-DBM simulation model developed by Jain et al. (2015). A pseudo 2D laboratory scale MSBC reactor with a modular insert will be used to investigate various configurations

of wire-mesh for various gas and liquid superficial velocities. The performance of wire mesh will be compared with a sulzer static mixer (SMV) that is commonly used in the industry. Different gas-liquid systems will be used to investigate hydrodynamics, mass transfer and chemisorption behavior in the MSBC.

The thesis is organized as follows: In chapter 2, the effect of the wire mesh configuration (i.e. mesh opening and wire diameter) is investigated in a pseudo 2D micro-structured bubble column (MSBC). The experiments are performed in an air-water system for various gas velocities. Different flow regimes are identified as a function of mesh opening and superficial gas velocity. An advanced digital image analysis (DIA) technique is used to quantify the bubble cutting and estimate the bubble size distribution, local gas holdup and interfacial area for the cases with and without micro-structuring. A conventional particle image velocimetry (PIV) technique is used to obtain instantaneous and time-averaged bubble velocities in the MSBC.

In chapter 3, the effect of the wire mesh is studied for the physical absorption of oxygen from air into water. The local concentration of dissolved oxygen in liquid is measured by using a non-invasive optical oxygen sensor. An mathematical model for oxygen absorption is discussed in this chapter to estimate the global mass transfer coefficient in the MSBC reactor. This is used to characterize the performance of the wire mesh in terms of mass transfer.

Chapter 4 investigates the bubble cutting behavior for a dodecane - nitrogen system using the digital image analysis technique developed in chapter 2. Dodecane is an ideal model fluid for hydrodynamics experiments as it is less prone to contamination in comparison with distilled water.

Chapter 5 investigates the effect of wire mesh configuration for the chemical absorption of CO_2 into sodium hydroxide ($NaOH$). The performance of the wire mesh is evaluated by measuring the local pH at the top of the reactor and the evolution of holdup with respect to time. The bubble size distribution can be estimated from the images of the column using the DIA technique. The effect of stacking multiple wire meshes on the performance of MSBC is studied for chemisorption. The discrete bubble model (DBM) is introduced in this chapter and the experimental results are used for validation of the DBM simulation.

In Chapter 6, the bubble cutting in a square micro-structured bubble column is investigated by an ultra-fast X-ray tomography technique. The pseudo-vertical flow structure, bubble size distribution and bubble velocity is obtained to characterize the effect of various superficial gas/liquid velocity. The bubble size distribution and bubble velocity is obtained by virtue of digital image analysis and cross-correlation technique respectively.

Finally, in chapter 7 the preliminary results of single bubble cutting in a wire mesh are presented, along with the recommendations for future work.

CHAPTER 2

Bubble cutting in an air-water system: Effect of superficial gas velocity*

r A novel micro-structured bubble column reactor (MSBC) is studied experimentally in this chapter. Micro-structuring is realized by using a wire mesh inserted in a pseudo-2D bubble column reactor. Different flow configurations of the wire mesh are evaluated by means of visual observation. Three different regimes with bubble cutting, bubble cutting followed by re-coalescence and gas pocket formation were observed for different wire meshes for superficial gas velocities ranging from 5 to 50 mm/s. An advanced digital image analysis technique (DIA) was used to determine the effect of wire mesh on the bubble size distribution, gas holdup and interfacial area. Detailed experiments were performed for wire meshes with mesh openings of 3.3 mm, 3.7 mm and 5.6 mm for superficial gas velocities ranging from 5 to 30 mm/s. Bubble cutting is observed at 3.7 mm mesh opening for superficial gas velocities up to 15 mm/s. At higher superficial gas velocities, the bubble breaks up to very small bubbles and bypasses the wire mesh unaffected.

2.1 Introduction

Bubble columns are widely used as gas-liquid contactors in the chemical industry. The simple design involves a vertical cylinder with no internals, operated in the co-current, counter-current or semi-batch mode. In the co-current operation both the gas and liquid are sparged using a distributor, whereas in the semi-batch mode the liquid is a batch phase with gas sparging. Bubble columns run in counter-current mode are useful for applications that require better mass transfer than co-current

*This chapter is based on: Sujatha et al. (2015)

columns, e.g. oxygen mass transfer in waste water treatment. The key advantages of conventional columns are their simple design, relatively easy operation and good mixing characteristics. But, their undesirable characteristics at high flow-rates are considerable degree of back-mixing in the gas and liquid phase, low interfacial area due to high coalescence rates and short gas phase residence time. Several alternative configurations are proposed in literature (Shah et al., 1982; Baird, 1992; Deen et al., 2000; Kantarci et al., 2005), to avoid the undesirable effects for industrial operation. To overcome these drawbacks, a novel micro-structured bubble column (MSBC) reactor is proposed.

Structuring of the bubble column is preferred to reduce channeling and promote radial mixing. It is achieved by using sieve trays, hollow fibers, screens or foam packings. Table 6.1 gives a summary of the different kinds of packings used in bubble columns, operating conditions and characteristic dimensions. Meikap et al. (2001) used a multi-staged vertical cylindrical bubble column made of perspex fitted with a total of five disks with perforations (3 contraction disks and 2 expansion disks). The contraction disks caused large bubbles to breakup into irregular shaped bubbles accompanied by a swarm of smaller bubbles. Whereas in the expansion zone, the bubbles change in size due to coalescence, breakup and surface stretching or contraction. The introduction of the hollow disks increases the mass transfer rate and gas holdup due to higher interfacial area (Meikap et al., 2002, 2004) caused by bubble breakup and turbulence. Höller et al. (2000) used a bubble column setup of hollow acrylic cylinders staged with structured fibrous catalytic layers. Their study concluded that the hydrodynamics parameters such as pressure drop and liquid circulation mainly depend on the distance between the threads. The mass transfer coefficient in the bubble column with staged fibrous layers was found to be 10 times higher than bubble column without internals (Höller et al., 2001). Krishna (Dreher and Krishna, 2001; Baten. and Krishna, 2003) performed residence time distribution (RTD) studies to study the effect of a porous plate on the liquid back-mixing in a modified bubble column. Their experiments and simulations revealed that the introduction of sieve trays with small open area (18.6%) severely affects the liquid circulation between compartments and the liquid exchange velocity is practically independent of the column diameter. Yang et al. (2012) analyzed the interaction between the rising bubbles and the trays, to determine the bubble size distribution and the bubble breakup frequency. They reported that the main effect of the sieve tray is the added drag force and bubble breakup depending on the sieve pore size. Bubble breakup occurred when the sieve pore size was larger than the Sauter mean diameter, otherwise the bubbles were slowed down.

Chen and Yang (1989) conducted hydrodynamics and mass transfer experiments in a bubble column partitioned by 37 wire-mesh screen plates (6-mesh screen plates with a fractional free area of 0.64 and a wire diameter of 0.58 mm) in columns with three different diameters (0.05, 0.075, 0.15 m). This configuration produced nearly identical bubbles of homogeneous size distribution, with small back-mixing of the liquid phase, large gas holdup and large mass transfer coefficient. The mass transfer coefficient increased with increasing superficial gas and liquid velocities, and the effect of column diameter was negligible. However, they did not study the effect of the wire

diameter.

Ito et al. and several other researchers (Prasser et al., 1998, 2001; Wangjiraniran et al., 2003; Prasser et al., 2005; Ito et al., 2011) studied the intrusive effect of the wire mesh on the liquid flow. Bubble deformation, fragmentation, deceleration, hydraulic resistance, turbulence generation and disturbance of flow profile were the most important intrusive effects caused by the wires. They concluded that the dependency of the bubble size on the intrusiveness of the wire mesh needs further research.

In this work, a micro-structured bubble column (MSBC) is studied using the wire mesh in a bubble column reactor. The effect of the wire mesh in two-phase bubbly flow is studied by using non intrusive experimental techniques such as digital image analysis (DIA) and particle image velocimetry (PIV). The effect of the mesh opening and wire diameter is determined for several wire mesh layouts. Experiments are performed by varying the superficial gas velocities in the MSBC reactor ranging from 5 to 50 mm/s. Visual observation is used for preliminary identification of different phenomena occurring in the MSBC reactor. Detailed experiments were performed for wire meshes with mesh openings 3.3 mm, 3.7 mm and 5.6 mm for superficial gas velocities 5 to 30 mm/s. Later, results of bubble size distribution, gas holdup, interfacial area and bubble velocity are used to analyze the impact of the wire mesh on bubble cutting and liquid circulation in the bubble column.

2.2 Digital image analysis

2.2.1 Image analysis algorithm

The digital image analysis (DIA) technique (Lau et al., 2013a,b) was developed to determine the mean diameter d_{eq}, bubble size distributions and gas holdup in pseudo-2D bubble column reactor. The image analysis algorithm has four main operations: a) image filtering b) separation of bubbles into solitary and overlapping bubbles c) segmentation of overlapping bubbles using watershedding technique d) combination of solitary and overlapping bubble images. Image filtering involves operations to obtain a desired image and removal of the inhomogeneous illumination using an Otsu filter Otsu (1975). This filter determines the threshold for separating the bubbles from the background, by thresholding individual blocks of an image. The edges of the bubbles are detected by a canny edge detection algorithm. Objects with area smaller than 100 square pixels are filtered as noise in original DIA of Lau et al. (2013b). The images are separated into solitary bubbles and overlapping bubbles using roundness as a separation criteria. The images with solitary bubbles are segmented by marking the bubbles whereas the overlapping bubbles are segmented using the watershed algorithm proposed by Meyer (1994a). Watershedding an image is analogous to flooding a catchment basin to determine the valley(minima) and contour peaks(maxima) in a topology. In the images, the center of the bubbles are the minima and the edges are the contours of the maxima. During watershed segmentation, the entire topology of the image is flooded by allowing water to rise from the points of minima to form catchment basins, creating watershed lines. The watershed lines are the divide lines between overlapping bubbles. The segmented images are used to determine the pixel area of each bubble object, and subsequently used to determine the average bubble diameter.

References	Type of packing	Operating conditions		Characteristic dimensions			
		V_g (m/s)	V_l (m/s)	D_c (m)	H (m)	D_w (mm)	M_O (mm)
Meikap et al. (2001)	contraction or expansion disks	0.106 - 0.1916	0.0024-0.0096	0.1905	2	-	-
Meikap et al. (2002)	contraction or expansion disks	0.106 - 0.1916	0.0024-0.0096	0.1905	2	-	-
Meikap et al. (2004)	contraction or expansion disks	0.106 - 0.1916	0.0024-0.0096	0.1905	2	-	-
Höller et al. (2000)	fibrous catalytic layers	0-0.6	0-0.015	0.0024	0.0015	0.3 0.7 2.4	0.3 0.6 1.3
Höller et al. (2001)	fibrous catalytic layers	0-0.6	0-0.06	0.0024	0.0015	0.3 0.7	0.3 0.6
Dreher and Krishna (2001) Baten. and Krishna (2003)	porous plate or sieve trays	0.05-0.4	-	0.10 0.15 0.38	6 4 4	10	-
Yang et al. (2012)	sieve tray	0-0.18	-	0.15	1.70	1.01-16.9	-
Chen and Yang (1989)	wire mesh screen	0.026-0.08	0-0.033	0.05 0.075 0.15	3	0.58	3.36
Prasser et al. (1998, 2001) Prasser et al. (2005)	wire mesh sensor	0.02-0.4	0-0.69	0.042		0.125	3
Wangjiraniran et al. (2003)	wire mesh sensor	0.0025 0.02 0.05	0.15	-	-	0.125	3
Ito et al. (2011)	wire mesh sensor	0.55-1.2	0.05-1.2	-	-	0.125	3

Table 2.1: Summary of literature study on different structured packings, operating conditions and characteristic dimensions. V_g is superficial gas velocity, V_l is superficial liquid velocity, D_c is column diameter, H is column height, D_w is wire or hole diameter, M_O is mesh opening.

In DIA technique, errors can occur due to different sources such as: imaging error, filtering errors, separation errors, segmentation error and computational error. The measurement accuracy of DIA is estimated by using artificial images as elaborately discussed in the paper of Lau et al. (2013a,b). For objects between 10-30 pixels, the maximum and minimum errors are estimated to be +2% and -6% respectively. For objects greater than 30 pixels, the error is estimated to be between +0.5% and -1.0%.

$$d_{eq} = \sqrt[2]{\frac{4A}{\pi}} \tag{2.1}$$

The Sauter mean diameter of a bubble is calculated from the equivalent diameter using the following equation. It is commonly used in process industry for the calculation of gas holdup and interfacial area:

$$d_{32} = \frac{\sum_{k=0}^{n} d_{eq,k}^3}{\sum_{k=0}^{n} d_{eq,k}^2} \tag{2.2}$$

2.2.2 Modifications to image analysis algorithm

Some modifications are made to the image analysis algorithm Lau et al. (2013a,b) to use it for the case with a wire mesh. The modified image analysis algorithm is illustrated in Fig. 2.1. The presence of the wire mesh in the image I_0 causes detection of false bubbles. Therefore the location of wire mesh pixels are determined in image I_0 and replaced by background pixels, as shown in image I_1. As described in previous section, objects smaller than 100 square pixels are usually removed in the filtering process, resulting in image I_2. As a consequence, small bubbles (less than 100 square pixels) in the image are filtered as noise and this is undesirable. Therefore, small bubbles (10 to 100 square pixels) are preserved by using two extra filter operations, in addition to the original filter process. The two filter steps are as follows: i) image normalization using CLAHE (Contrast limited adaptive histogram equalization) resulting in image J_1 and ii) stretching pixel values over the entire image scale resulting in image J_2. The filtered image with small bubbles (10 to 100 square pixels) J_3 are obtained by masking J_2 with I_2. The pixel area of each bubble object in image J_3 is used to determine the average bubble diameter and combined with data from original image analysis algorithm.

Another difference with the work of Lau et al. (2013a,b) is that the resolution of the images is improved by using a better camera. 16 bit images are used instead of 8 bit images to avoid loss of any details in the image. Moreover, images were obtained with a higher resolution, the effects of which are illustrated in Fig. 2.2. It can be seen that at the higher resolution small bubbles of about 0.5 mm can be discerned.

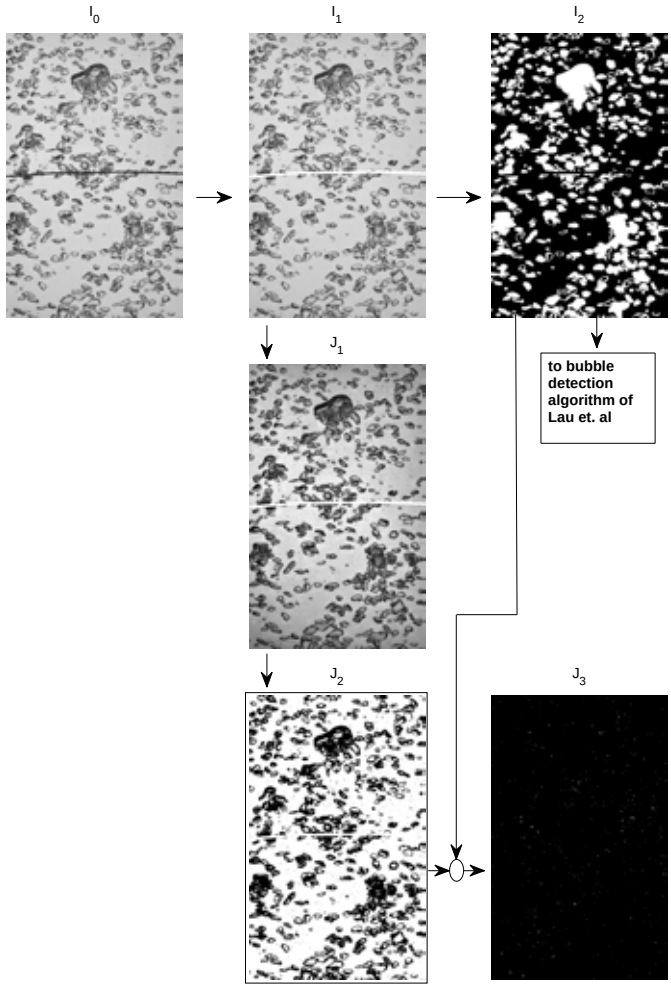

Figure 2.1: Modified image analysis algorithm. I_0 - original image, I_1 - image without wire mesh, I_2 - image after objects smaller than 100 square pixels are filtered, J_1 - resulting image after normalization of I_1 with CLAHE, J_2 - resulting image after stretching histogram over entire intensity scale on J_1, J_3 - image obtained by masking J_2 with I_2 .

2.3 Particle image velocimetry

Bubble velocities were measured using particle image velocimetry (PIV), where the shadow images of the bubbles were ued as 'tracers' of the gas phase velocity. A high speed camera is used to capture images of the bubbly flow in the column. Pairs of subsequent images are coupled and divided into small interrogation areas for process-

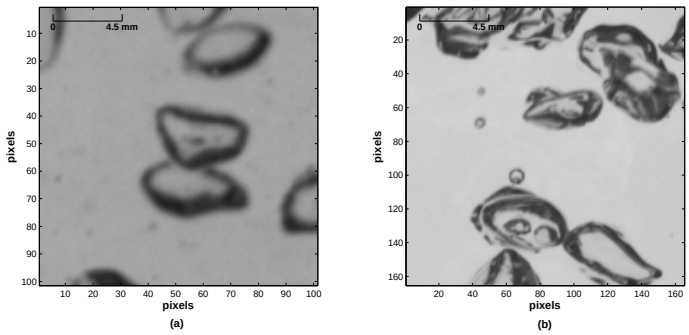

Figure 2.2: Close-ups of camera recordings obtained from cameras with different spatial resolutions. Left: 0.18 mm/pixel, right: 0.11 mm/pixel.

ing. The volume averaged displacement $\vec{s_d}(x,t)$ of the bubbles within the interrogation area of the subsequent images are obtained by cross-correlation analysis. When the interrogation areas contain a sufficient number of bubbles, the cross-correlation consists of a dominant correlation peak embedded in a background of noise peaks. The tallest peak is usually identified as the displacement-correlation peak, and its location corresponds to the bubble displacement. Provided that the time between subsequent images (Δt) is sufficiently small, the volume averaged bubble velocity within the interrogation areas $\vec{v}(x,t)$ is then determined by dividing the measured bubble displacement by the image magnification factor M and Δt:

$$\vec{v}(x,t) = \frac{\vec{s_d}(x,t)}{M\Delta t} \tag{2.3}$$

In this work, we will particularly focus on the average vertical bubble mean and fluctuating velocities across the width of the pseudo-2D bubble column just above the wire mesh. The PIV camera is equipped with a Nikkor 50 mm 1.8 AF lens and is placed at a distance of 2 m to capture the whole column. A total of 5000 images at a sampling frequency of 50 Hz, which corresponds to 100 s, is recorded in one measurement. The images are paired (time delay=0.02 s) and processed using the PIV software (DaVis), developed by LaVision. A $32 \times 32 pix^2$ interrogation area was used for cross correlation analysis in combination with a post-processing technique using a median test to remove spurious vectors.

2.4 Material and methods

A flat pseudo-2D bubble column reactor of dimensions (width W=0.2 m, depth D=0.03 m, height H=1.3 m) is chosen for experiments. Experiments are carried out in the MSBC for an air-water system. The reactor walls are constructed of transparent glass to enable visual observation by the eye or using a camera. The glass wall has a slit on the front and the back faces (slit dimensions are 200 mm×15 mm.) at a height of 1 m from the bottom plate, to allow for the liquid to overflow to a

Mesh #	wire diameter (mm)	mesh opening (mm)	open area (%)
4	0.80	5.6	76
6	0.55	3.7	76
6	0.90	3.3	62
8	0.50	2.7	71
10	0.31	2.2	75
12	0.31	1.8	73
18	0.22	1.2	71

Table 2.2: Overview of different wire meshes used for experiments.

storage vessel. A liquid pump is used to recirculate the liquid into the column at a set flow-rate, through a liquid distributor plate. The liquid distributor plate has perforations of 3.2 mm diameter, arranged in a 60 degree staggered configuration with a distance of 4.5 mm between neighboring perforations. The gas is fed into the column via a group of fifteen (15) gas needles centrally arranged in the distributor plate. The needles have a length (L) = 50 mm, inner diameter (I.D.) = 1 mm and outer diameter (O.D.) = 1.5875 mm. The needles extend 10 mm above the bottom plate and are spaced with a center-to-center distance of 9 mm. An array of five needles is classified as a group, and each group of nozzle is connected to a mass flow controller. Subsequently, three mass flow controllers are used to control the gas flow rates in the column. Both the gas and liquid are fed into the reactor from the bottom by means of the distributor assembly. A schematic figure of the experimental setup is shown in Fig. 2.3. Micro-structuring in the reactor is realized by means of thin wires of various dimensions arranged in a woven mesh structure. The wire mesh can be mounted onto the column by using the modular insert, designed for this purpose. The modular insert design allows full flexibility to attach one or more wire meshes at different locations of the insert. The dimensions of the column including the insert are as follows: width=0.14 m, depth=0.03 m, height=1.3 m. The location of the wire mesh was fixed for the experiments at a distance of 0.518 m from the bottom distributor plate. Table 2.2 outlines the overview of different wire-mesh lay-outs used for experiments.

A CMOS camera with resolution of 2016 $\times$ 2016 *pixels* is used to capture the images of two-phase bubbly flow by using back-lighting to obtain maximum contrast between the bubbles and the background. In this chapter, the DIA technique has been extended to the MSBC. The MSBC is divided into five different sections for the purpose of imaging and 4000 images are captured at 50 Hz for each section, for all velocities and mesh configurations. The images from each section have a size of 0.21 m$\times$0.14 m and a small overlap of 0.05 m. Repeatability of experiments was verified by checking the overlapping regions of images from different sections. The resolution of the image is 0.11 mm/pixel. Objects with area smaller than 10 square pixels are

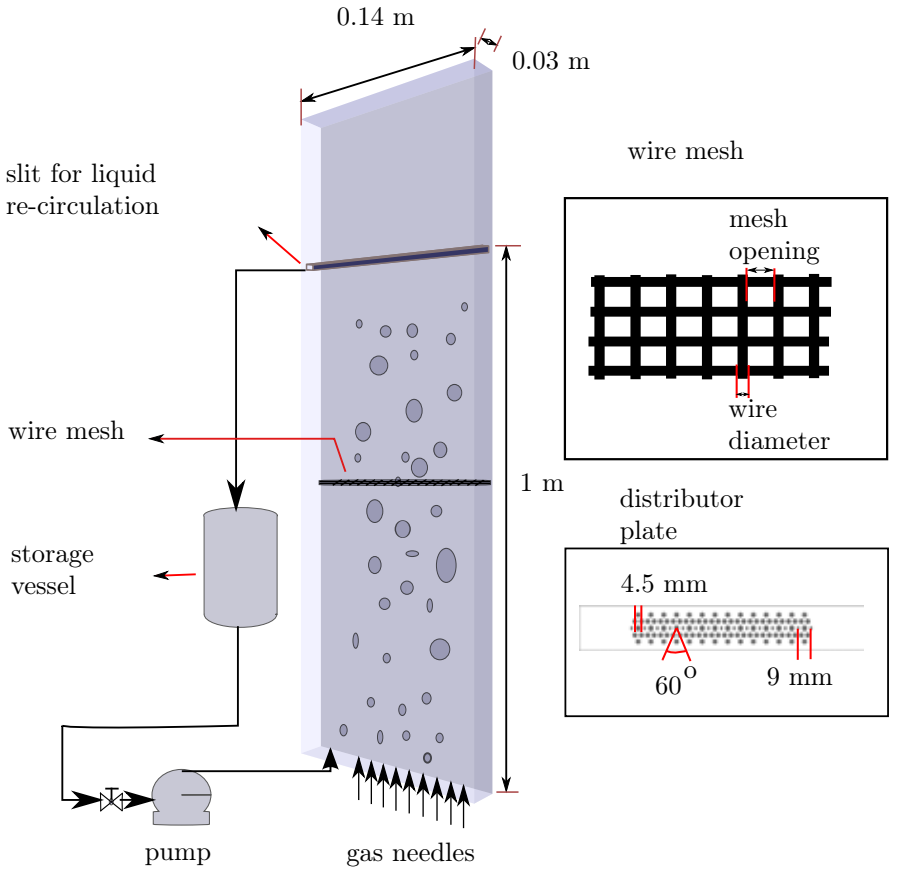

Figure 2.3: A schematic diagram of micro-structured bubble column.

filtered as noise. For a circular object with area 10 square pixels, the bubble diameter can be calculated as 3.6 pixels. Therefore the minimum detectable bubble size by DIA technique is 0.39 mm at the applied spatial resolution.

2.5 Results and discussion

2.5.1 Visual observation

Images are obtained using the high-speed camera operated at 50 Hz, for a velocity of 5-30 mm/s for different wire meshes. Four different phenomena can be observed by varying superficial gas velocities and wire meshes: bubble cutting, bubble cutting and immediate re-coalescence, gas cap formation and gas by-passing (Refer Table 2.3).

It can be inferred from visual observation that the 3.3 mm wire mesh opening causes deceleration of the bubbles and bubble bypass. The 3.7 mm mesh causes some bubble cutting as shown in Fig. 2.4. Finally, at a 5.6 mm mesh opening cutting

and re-coalescence occurs (see Fig. 2.6). When the mesh opening was smaller than 3.3 mm, the formation of a gas cap was observed as shown in Fig. 2.5. Fig. 2.6, shows a lamellar separation layer between the two bubbles after they are cut. As the bubbles rise in the column, the lamellae disappear and the bubbles re-coalesce to form a large bubble. At high velocities above 20 mm/s, there are distinct liquid circulation patterns observed below the wire mesh, thereby reducing the liquid back-mixing inside the reactor.

The variation in large scale flow structures present in the MSBC equipped with a wire mesh can be observed in Fig. 2.7 and Fig. 2.8. A series of snapshots of the different mesh configurations are shown for two different velocities, i.e. 15 mm/s and 30 mm/s respectively.

The effect of wire diameter is determined by comparing experiments done for different wire diameters (0.55 and 0.9 mm) at almost same mesh opening (3.7 and 3.3 mm). It is observed that thin wires do a better job in cutting the bubbles than the thick wires.

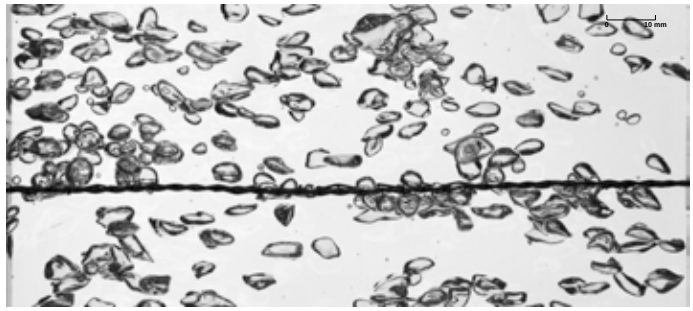

Figure 2.4: Bubble cutting with a 3.7 mm wire mesh at a superficial gas velocity of 15 mm/s. Small bubbles can be noticed above the wire mesh.

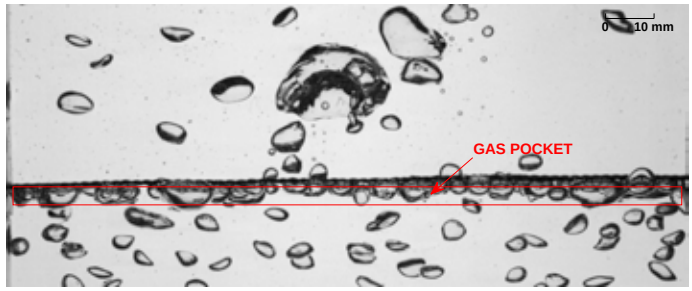

Figure 2.5: Bubble cutting with a 2.2 mm wire mesh at superficial gas velocity of 15 mm/s. Gas pocket formation can be noticed below the wire mesh.

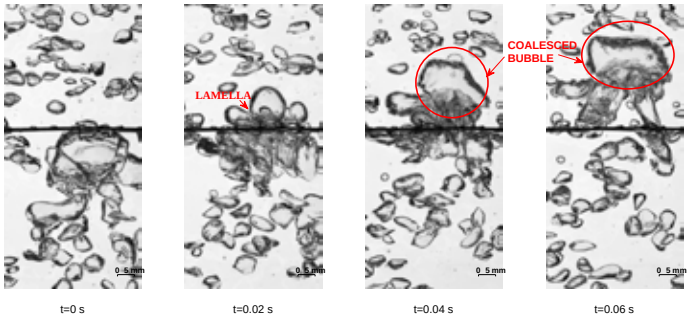

Figure 2.6: Bubble cutting with a 5.6 mm wire mesh at a superficial gas velocity of 15 mm/s. Lamella formation and re-coalescence of bubbles can be observed.

mesh opening [mm]	superficial gas velocity [mm/s]						
	5	10	15	20	30	40	50
5.6	+	+	+	+	+	++	++
3.7	+	+	+	+	++	++	++
3.3	+	-	-	+	+	++	++
2.7	×	×	×	-	-	++	++
2.2	×	×	×	×	-	++	++
1.8	×	×	×	×	×	×	++
1.2	×	×	×	×	×	×	×

Table 2.3: Flow regime map for micro-structured bubble column: (+) bubbles move through the wire mesh and bubble cutting occurs. (++) bubbles flow through wire mesh but re-coalesce immediately and bubble cutting occurs . (-) bubbles retained with no by-pass. (×) gas cushion formation with by-pass.

2.5.2 Bubble size distribution and gas holdup using digital image analysis (DIA)

The number density function (NDF) for a particular bubble diameter class is the ratio of number of bubbles in a particular diameter class(Δd_{eq}) to the sum of number of bubbles in all size classes. Therefore, the NDF of each size class(Δd_{eq}) is calculated from the number of bubbles and average bubble diameter as follows:

$$NDF_{\Delta d_{eq}} = \frac{N_{\Delta d_{eq}}}{\sum_{\Delta d_{eq,min}}^{\Delta d_{eq,max}} N_{\Delta d_{eq,k}}} \tag{2.4}$$

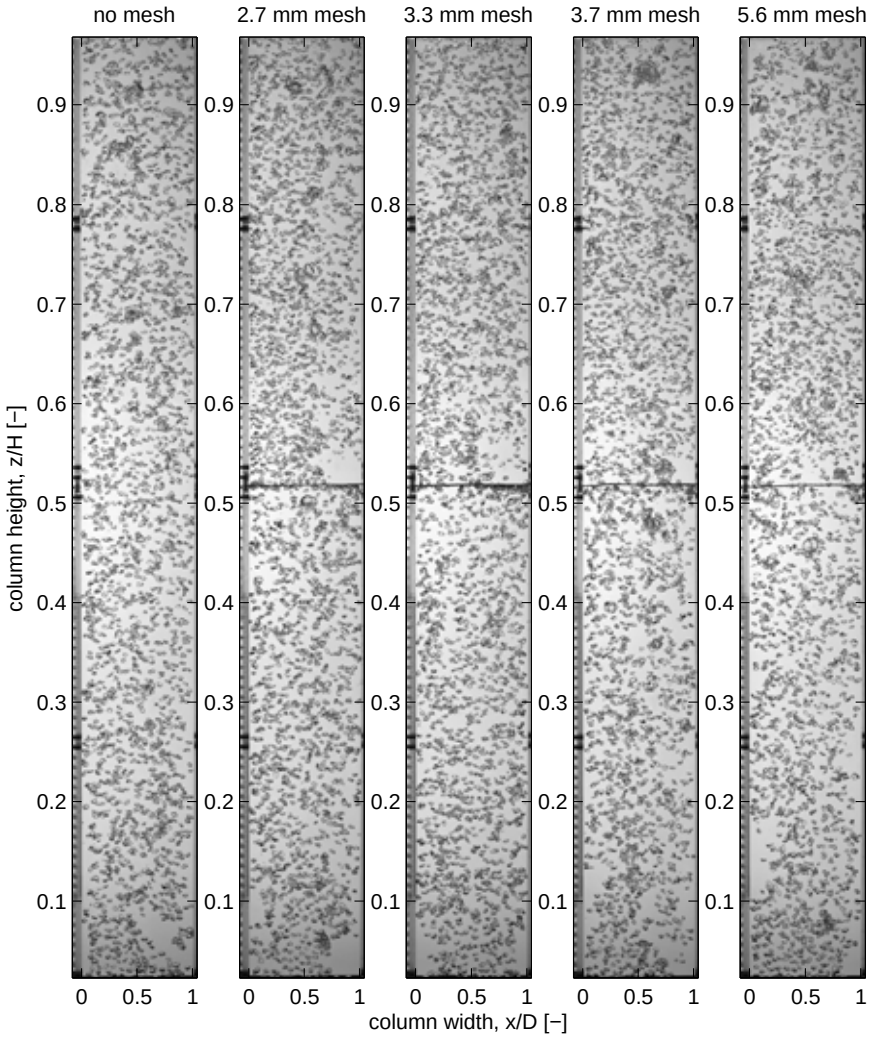

Figure 2.7: Comparison of bubble cutting at a superficial gas velocity of 15 mm/s for cases with meshes and no mesh. Images from left to right: no mesh, 2.7 mm mesh opening, 3.3 mm mesh opening, 3.7 mm mesh opening and 5.6 mm mesh opening.

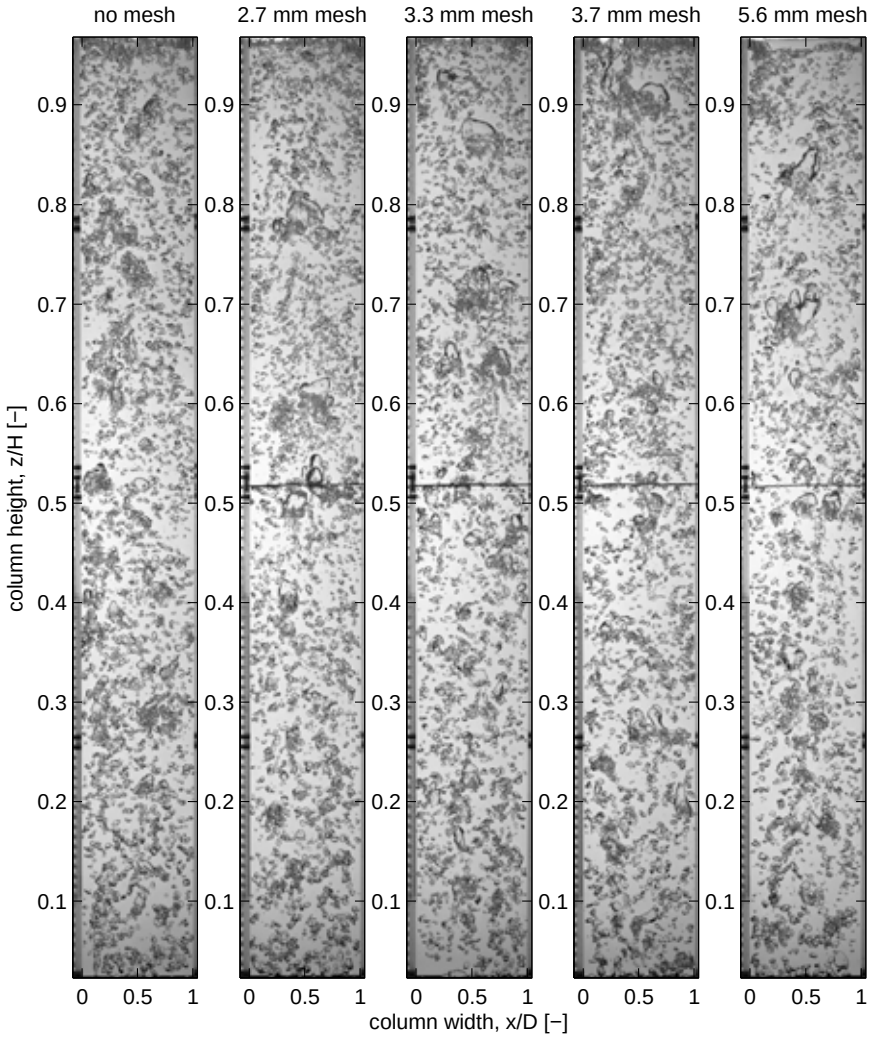

Figure 2.8: Comparison of bubble cutting at a superficial gas velocity of 30 mm/s for cases with meshes and no mesh. Images from left to right: no mesh, 2.7 mm mesh opening, 3.3 mm mesh opening, 3.7 mm mesh opening and 5.6 mm mesh opening.

Bubble size distributions for different wire meshes (3.3 mm, 3.7 mm and 5.6 mm mesh openings) are compared with the case without wire mesh, for section 3 (41-62 cm) as shown in Fig. 2.9. At low superficial gas velocities (5-15 mm/s), the bubble size distribution has one dominant peak around 4 mm that tends to shift towards lower diameters in the presence of the wire mesh. The peak shifts towards lower diameters because the bubbles are cut in the presence of wire mesh, as can be seen above the wire mesh in Fig. 2.4. At higher superficial gas velocities (20-30 mm/s), the wire mesh does not contribute favorably to bubble cutting. From Fig. 2.10, it can be concluded that the bubble size distributions are almost identical in all the sections of the column, except the top region (73-94 cm). A large fraction of small bubbles accumulate at the top section of the bubble column, as an effect of liquid down flow circulation. The residence times of these small bubbles are very high due to the strong liquid circulation, which makes it difficult for the bubbles to escape the column. These small bubbles were not observed in the results of Lau et al. (2013a,b), since any objects smaller than 0.9 mm were removed from the images as noise.

The gas holdup is determined for the air-water system by liquid expansion measurements. It is calculated by the following formula:

$$\varepsilon_{(g,H)} = \frac{h_f - h_0}{h_f} \tag{2.5}$$

where h_f is the height of the gas-liquid dispersion and h_0 is the initial height of the liquid. The integral gas holdup can be also calculated from the DIA using the method used by Lau et al. (2013b):

$$\varepsilon_{(g,DIA)} = \frac{\sum_{k=0}^{n} \frac{\pi d_{32,k}^3}{6}}{(W - 2d_{32})(H - 2d_{32})D} \tag{2.6}$$

Where $W \times D \times H$ are the dimensions of the field of view. The gas holdup is determined by height expansion measurements and DIA experiments. Fig. 2.11 shows the gas holdup vs superficial gas velocity for different cases with and without wire mesh. It can be observed from the DIA results that the gas holdup is higher for the 3.3 and 3.7 mm mesh openings than the case without wire mesh and 5.6 mm mesh opening. At high superficial gas velocity (30 mm/s) the gas holdup from DIA shows a large deviation from the gas holdup from expansion measurements, which is due to the limitation of the DIA algorithm to detect all bubbles at high gas holdups. This issue was also observed by Lau et al. (2013a,b) and can mainly be attributed to the separation and segmentation errors that are associated with non-spherical bubbles found at high velocities and high gas holdups. Non-spherical bubbles can cause errors during separation of bubbles into solitary and overlapping bubble objects, i.e. non-spherical bubbles can be interpreted as a cluster of bubbles. These non-spherical bubbles have multiple edges in the image due to their complex shape, which are

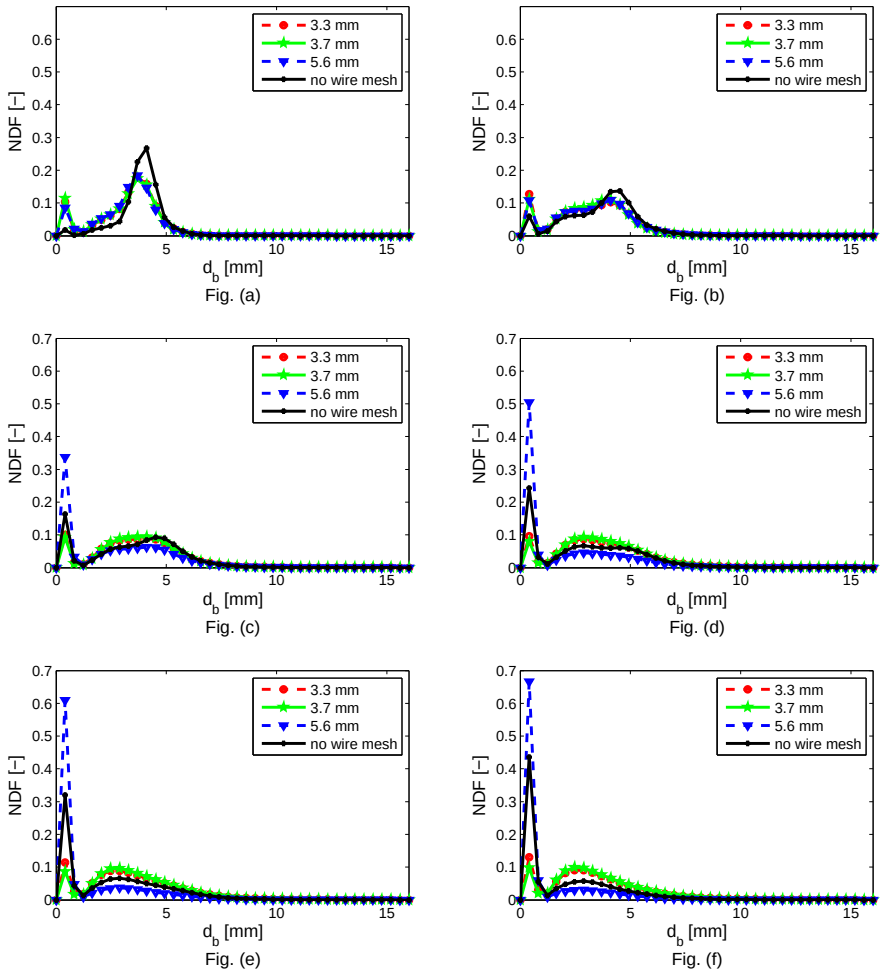

Figure 2.9: Evolution of bubble size distributions of section 3 (section with wire mesh placed in the middle) for increasing superficial gas velocities and with different wire mesh openings: (a) 5 mm/s, (b) 10 mm/s, (c) 15 mm/s, (d) 20 mm/s, (e) 25 mm/s and (f) 30 mm/s.

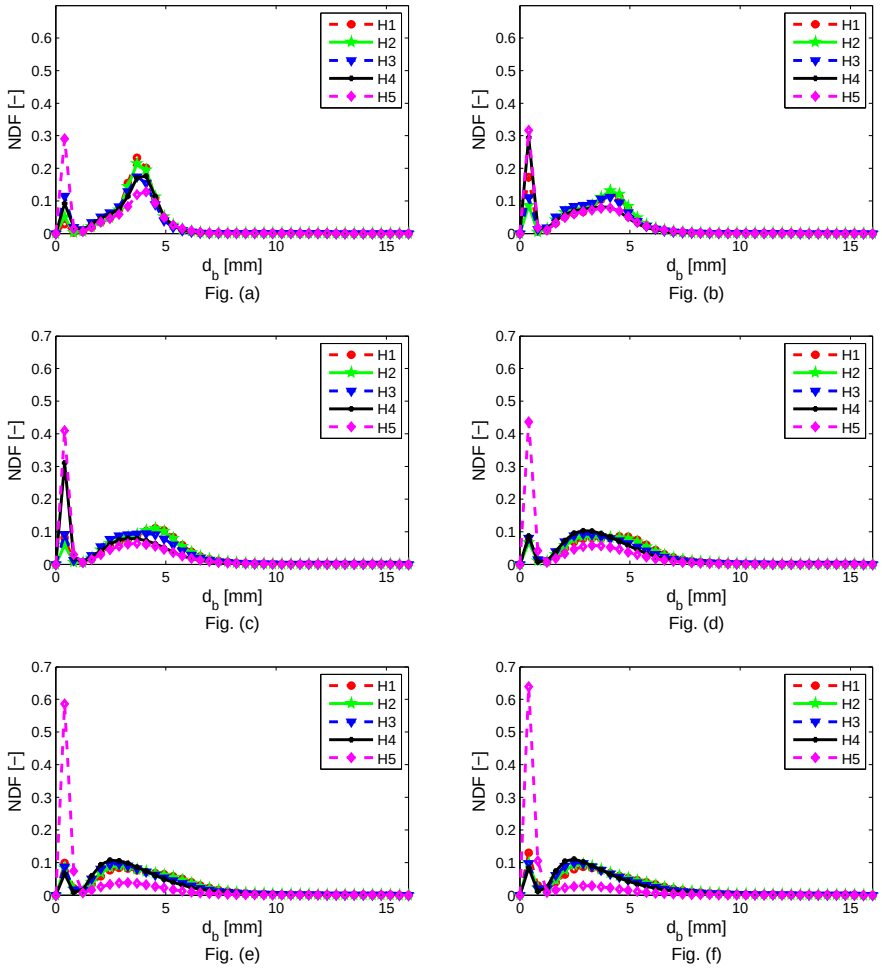

Figure 2.10: Evolution of bubble size distributions of all sections for increasing superficial gas velocities and with 3.7 mm mesh opening: (a) 5 mm/s, (b) 10 mm/s, (c) 15 mm/s, (d) 20 mm/s, (e) 25 mm/s and (f) 30 mm/s. The height of the sections is as follows: H1= 0.09 to 0.30 m, H2= 0.25 to 0.46 m, H3= 0.41 to 0.62 m, H4= 0.57 to 0.78 m and H5= 0.73 to 0.94 m.

detected as separation lines during segmentation. Therefore they are misidentified as a cluster of overlapping bubbles resulting in over-segmentation. Smaller bubbles have lower contribution to the gas holdup thus resulting in an under-prediction of the gas holdup compared to gas holdup obtained from the height expansion. The interfacial area is a measure of the effect of the wire mesh inside the MSBC. The meshes with openings of 3.7 mm and 3.3 mm lead to a larger interfacial area than the case with no wire mesh, as shown in Fig. 2.12. For the wire mesh with 5.6 mm opening the interfacial area is decreased due to greater coalescence in the bubble column.

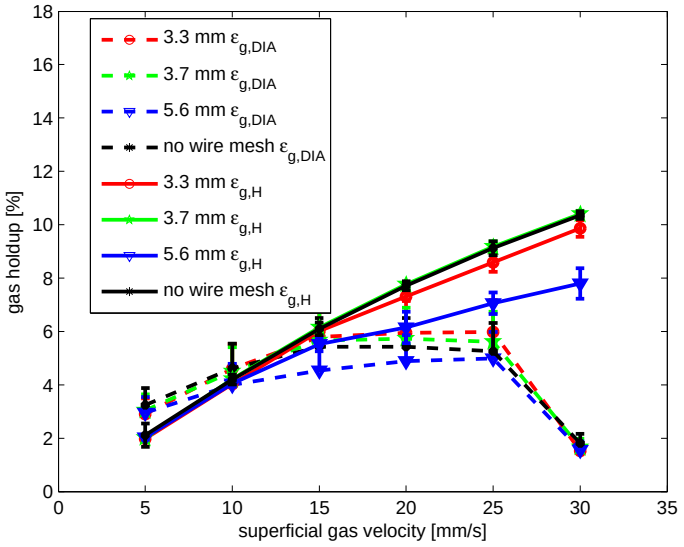

Figure 2.11: Gas holdup versus superficial gas velocity for different wire mesh openings. Solid lines with markers indicate gas holdup obtained from liquid expansion experiments. Dashed lines with markers indicate gas holdup determined by DIA technique. Error bars in gas holdup measurements are included, for both expansion measurements and DIA.

The bubble size distribution above and below the wire mesh are plotted in Fig. 2.13. This figure clearly shows that above the wire mesh the bubble size distribution shifts towards small bubble diameters.

An experimentally recorded image along with corresponding instantaneous and time averaged gas velocity maps is shown in Fig. 2.14, for the 3.7 mm mesh opening at a superficial gas velocity of 15 mm/s. It can be observed that the bubbles form a bubble plume that rises in the middle of the column leading to higher velocities in that region as compared to the sides of the column. Some vortices can also be observed in the column below the wire mesh but they disappear above the mesh. The intrusive effect of wires was also observed by Ito et al. (2011) and Wangjiraniran et al. (2003), but they studied wire mesh sensors with a small vertical spacing between wire planes. It is evident that the presence of the wire mesh disturbs the bubble plume

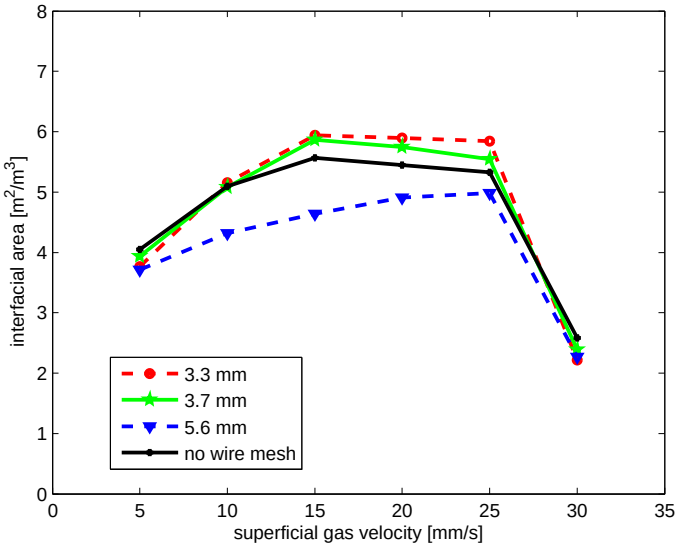

Figure 2.12: Interfacial area versus the superficial gas velocity for different wire mesh openings.

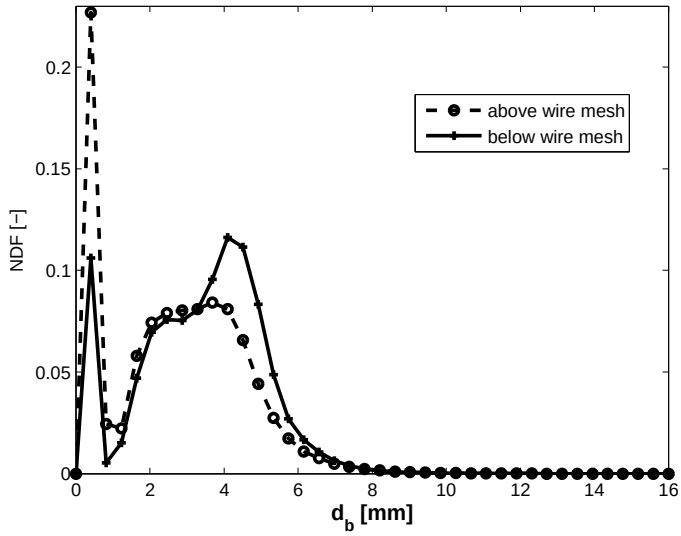

Figure 2.13: Evolution of bubble size distribution above and below the wire mesh at a superficial gas velocity of 10 mm/s. The mesh opening is 3.7 mm.

and spreads the bubbles along the width of the column as shown in Fig. 2.7, Fig. 2.8 and Fig. 2.14. This leads to a deceleration of the bubbles in the plume, thereby increasing the bubble residence time. A comparison of the bubble rise velocity and velocity fluctuations for the 3.7 mm mesh opening and no mesh case at a height just above the wire mesh (z/H=0.0525) is shown respectively in Fig. 2.15 and Fig. 2.16. At a superficial gas velocity of 25 mm/s , the bubbles at the center of the column (x/D=0.5 and z/H=0.0525) are found to decelerate by a velocity of 0.05 m/s, in the presence of the 3.7 mm wire mesh.

The presence of the wire mesh leads to significant fluctuating bubble velocities as seen in Fig. 2.16. The fluctuations in the bubble rise velocity are expected to lead to a quicker surface renewal of the liquid film around the bubbles which should positively affect the mass transfer coefficient in application concerning mass transfer and chemical reactions that are limited by the gas-liquid mass transfer rates.

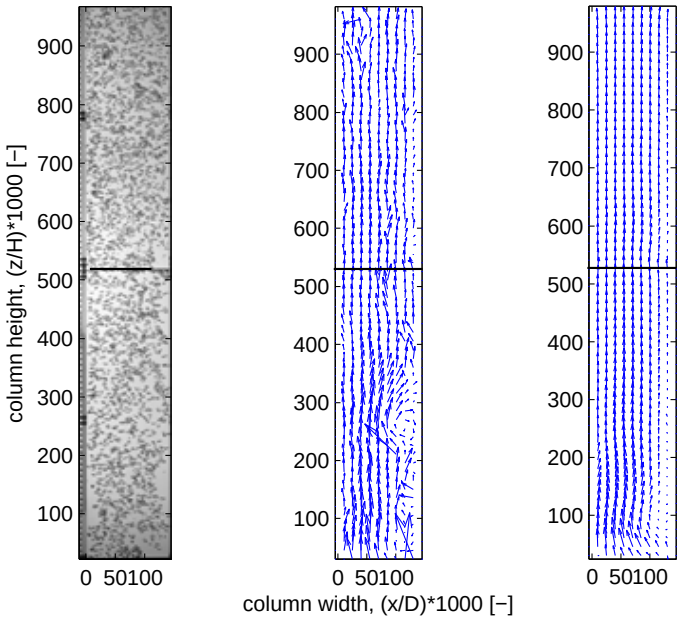

Figure 2.14: Instantaneous bubble position showing flow-structures observed during experiments at 15 mm/s for 3.7 mesh opening (left), corresponding instantaneous gas velocity from PIV (center) and time-averaged gas velocity (right). Wire mesh is located at a distance of 0.518 m from bottom distributor and is denoted by a solid line.

2.6 Conclusions

In this work, a micro-structured bubble column (MSBC) was studied using wire meshes. The hydrodynamics of the MSBC reactor is studied using an advanced

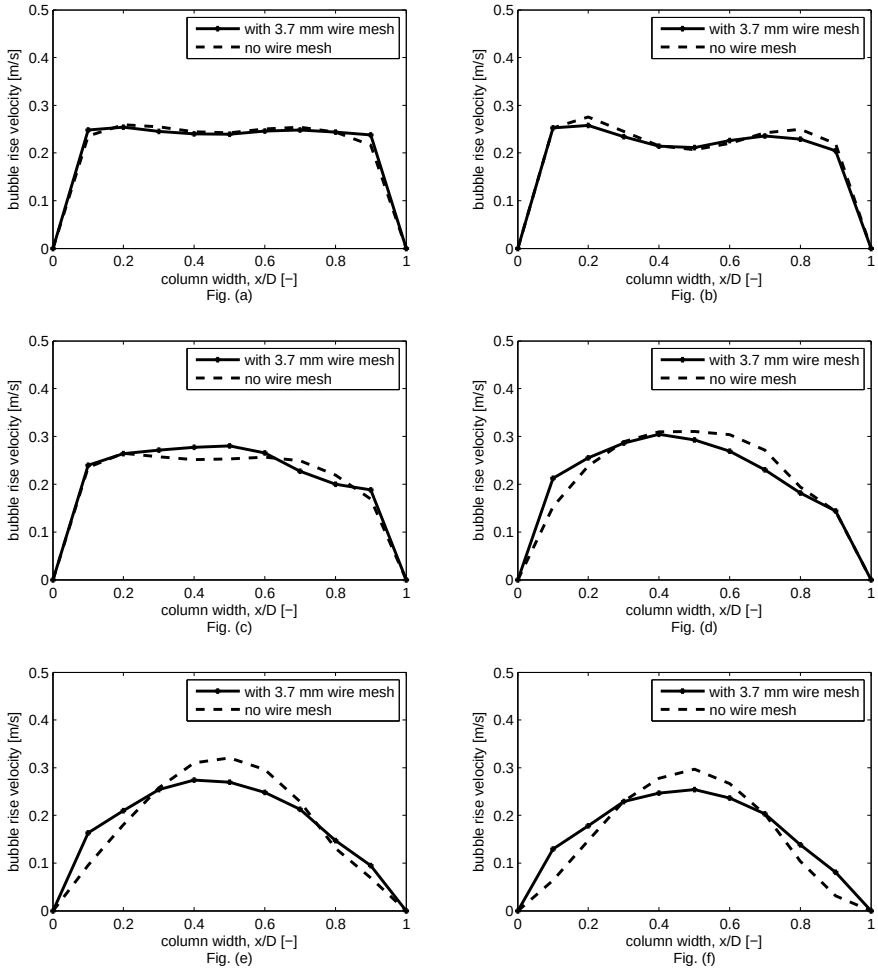

Figure 2.15: Time averaged bubble velocity profiles just above the wire mesh (at column height of 0.525 m) at increasing superficial gas velocity to compare cases with 3.7 mm wire mesh and without wire mesh: (a) 5 mm/s, (b) 10 mm/s, (c) 15 mm/s, (d) 20 mm/s, (e) 25 mm/s and (f) 30 mm/s.

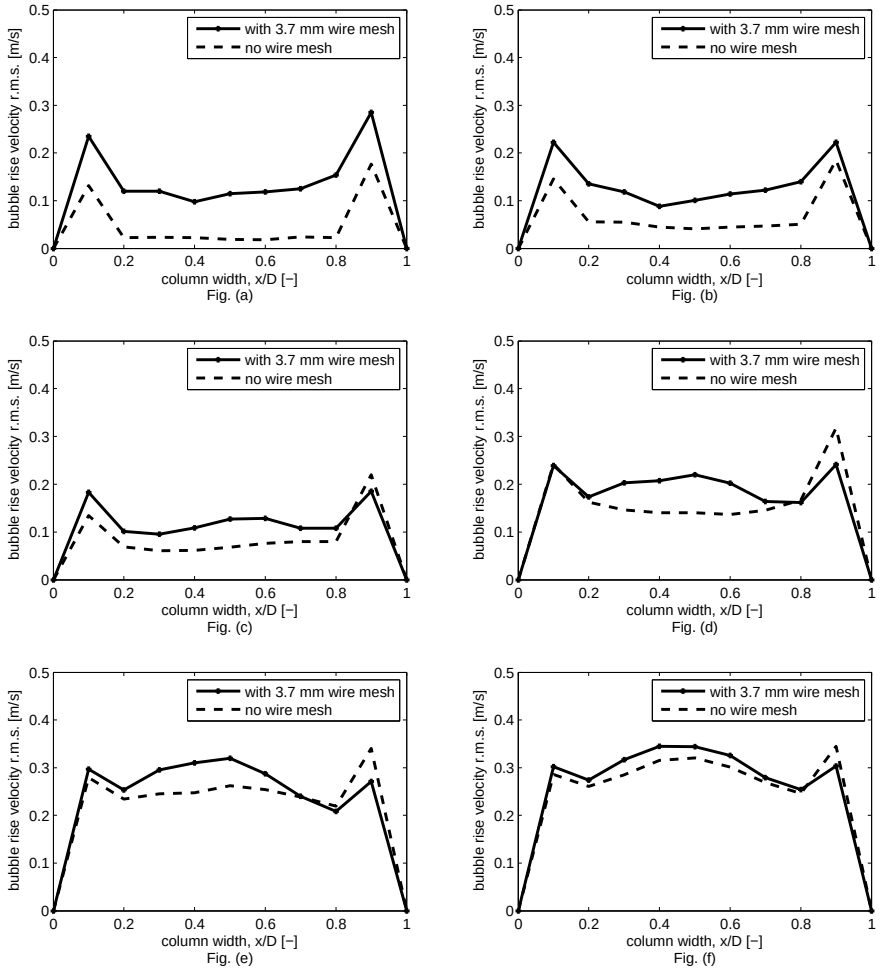

Figure 2.16: Time averaged bubble velocity fluctuation profiles just above the wire mesh (at column height of 0.525 m) at increasing superficial gas velocity to compare cases with 3.7 mm wire mesh and without wire mesh: (a) 5 mm/s, (b) 10 mm/s, (c) 15 mm/s, (d) 20 mm/s, (e) 25 mm/s and (f) 30 mm/s.

digital image analysis (DIA) technique. The DIA technique performs satisfactorily for gas velocities up to 25 mm/s. At higher superficial gas velocities, the bubble detection is hampered by the high gas holdup. In those cases, it is recommended to use other techniques, like X-ray tomography.

The bubble cutting was found to be a function of wire diameter, the mesh opening and also the superficial gas velocity. A small wire diameter and a mesh opening smaller than the average bubble size have good bubble cutting characteristics, in particular, the 3.7 mm mesh opening with 0.55 mm wire diameter. In case the mesh opening was smaller than 3.3 mm, the bubbles were slowed down by the wire mesh and the formation of a gas cap was noticed. In the 5.6 mm wire mesh opening, the bubbles bypass the wire mesh as the bubbles are smaller than the openings.

Bubble cutting was observed for superficial gas velocities in the range of 5 to 15 mm/s and for higher gas velocities bubble cutting was insignificant. The presence of the wire mesh generates liquid circulation cells above and below the wire mesh, thereby reducing liquid back-mixing. The wire mesh also has an intrusive effect on the bubble plume and generates enhanced velocity fluctuations above the wire mesh, that might favorably affect the mass transfer coefficient. The holdup and interfacial area in the MSBC were observed to be higher than in a conventional bubble column without any internals for mesh openings smaller than the average bubble diameter.

Nomenclature

μ	dynamic viscosity	$\left[kg.m^{-1}.s^{-1}\right]$
ε	gas holdup	$[-]$
A	area	$[m^2]$
D	depth	$[m]$
d	diameter	$[m]$
H	height	$[m]$
h	height of liquid-gas dispersion	$[m]$
W	width	$[m]$
0	initial	
eq	equivalent	
f	final	
g	gas	
H	height expansion	
k	index	
DBM	discrete bubble model	
DIA	digital image analysis	
DNS	direct numerical simulations	
FT	front tracking	
IBM	immersed boundary method	
LS	level-set	
MSBC	micro-structured bubble column	
PIV	particle image velocimetry	
TFM	two fluid model	
VoF	volume of fluid	

CHAPTER 3

Effect of bubble cutting on physical absorption in micro-structured bubble column

In this work, a micro-structured bubble column reactor (MSBC) is studied experimentally for the absorption of oxygen into water. To this end, a pseudo-2D bubble column reactor is used, where the micro-structuring is realized by virtue of wire meshes. These serve as devices that can periodically cut large bubbles into smaller ones. MSBC performance is evaluated by measuring the volumetric mass transfer coefficient (k_La) and the interfacial area (a). The former is determined by dynamic absorption measurements using a non-intrusive oxygen sensor. Whereas, the latter is determined by means of an advanced digital image analysis technique (DIA) for superficial gas velocities up to 25 mm/s. The individual mass transfer coefficient k_L can be derived indirectly from the combined measurements of (k_La) and a. Results are reported for wire meshes of different openings (3.3 mm, 3.7 mm and 5.6 mm) and compared with a commercially available Sulzer packing (SMV).

3.1 Introduction

Bubble column reactors are frequently used in the chemical industry for processes for contacting a gas and a liquid phase. These reactors usually comprise of cylindrical vessels in which gas is sparged from the bottom in the form of bubbles into a quiescent liquid. The bubbles induce mixing of the liquid phase and leave the liquid at the top through the gas-liquid interface. Some applications of bubble columns include oxygen absorption into water for biological waste-water treatment, reactions limited by gas-liquid mass transfer and fermentation. The main advantages of bubble columns are

the simple design, ease of operation, high gas-liquid interfacial area and good mixing characteristics (Shah et al., 1982; Baird, 1992; Deen et al., 2000). However, at high gas flow-rates, they exhibit a considerable degree of back-mixing in the gas and liquid phase, low interfacial area due to high coalescence rates and short gas-phase residence time. Therefore, the mass transfer rate attained at high gas flow-rate is significantly reduced in a conventional bubble column.

Several modifications have been proposed in the literature to overcome the disadvantages of conventional bubble columns. Internal structuring has been applied to reduce channeling and promote meso-scale mixing. A few examples of applied internals are: sieve trays, hollow fibers, screens, foam packing and static mixers. Hydrodynamics (Meikap et al., 2002; Baten. and Krishna, 2003; Chen and Yang, 1989; Yang et al., 2012; Höller et al., 2000), mixing (Dreher and Krishna, 2001; Lakota et al., 2001) and mass transfer studies (Meikap et al., 2004; Höller et al., 2001; Lakota et al., 2002) have been performed in bubble columns employing different internals.

The gas-liquid mass transfer rate in bubble columns is a complex function of different variables such as the concentration difference of components between the gas-liquid interface and the bulk, the interfacial area and the liquid or gas-side mass transfer coefficient. If the gas solubility in the liquid is low, such as oxygen or nitrogen in water, the resistance lies on the liquid side and such a system is said to be liquid phase controlled. In this situation, the overall mass transfer coefficient is fully determined by the liquid-phase mass transfer coefficient, k_L. The volumetric mass transfer coefficient depends on both k_L and the specific surface area a, and is the product of these two parameters. In practice, it is easier to measure the volumetric mass transfer coefficient (k_La), rather than the individual mass transfer coefficient (k_L). In terms of the penetration theory for mass transfer, k_L depends on the ratio of the square root of diffusivity of dissolved gas in the liquid and the contact time of liquid parcels with the gas bubble. The contact time of the liquid parcel with the bubble is assumed to be constant and depends on the relative velocity of the gas bubble and the liquid. Hence, a higher rise velocity of bubbles, leads to an increase in k_L. However, this effect is counter-balanced by lower values of the interfacial area (a). According to Koynov et al. (2005), bubbles that travel together in swarms are disturbed by the wakes of neighboring bubbles. Moreover, bubbles moving in swarms are subject to mutual hindrance leading to lower relative velocities. Therefore, the concentration of dissolved gas in the liquid depends on the cumulative mass transfer from all the bubbles in the swarm. Henceforth, the mass transfer in a bubble swarm is lower, compared to that of a single bubble.

Akita and Yoshida (1973, 1974) performed experiments for absorption of oxygen into different liquids and they studied the effect of column diameter on interfacial area, gas holdup and mass transfer coefficient. Correlations were determined from experimental data for gas holdup (ε_G), interfacial area (a) and volumetric mass transfer coefficient (k_La) as given by the Eqn. 3.1, Eqn. 3.2 and Eqn. 3.3 respectively.

$$\frac{\varepsilon_G}{(1-\varepsilon_G)^4} = 0.20We^{0.125}Ga^{0.0833}Fr \tag{3.1}$$

$$aD_c = \frac{1}{3} We^{0.5} Ga^{0.5} \varepsilon_G^{1.13} \tag{3.2}$$

$$\frac{k_L a D_c^2}{D_{AB}} = 0.6 Sc^{0.5} We^{0.62} Ga^{0.31} \varepsilon_G^{1.1} \tag{3.3}$$

where Sc = Schmidt number, We is the Weber number, Ga is the Galileo number, Fr is the Froude number, D_c is the equivalent column diameter, D_{AB} is the diffusivity of gas (A) into liquid (B) and ε_G is the gas holdup.

The presence of internals leads to a decrease in the average bubble size and causes a decrease in k_L (Youssef, 2010; Lo, 2012). The decrease in k_L in the presence of internals was found to be a consequence of the decrease in the turbulent intensity of the system (Fortescue and Pearson, 1967; Lamont and Scott, 1970). However, in the presence of internals, bubble coalescence and breakup leads to a net increase in the interfacial area. This directly results in a significant increase in the volumetric mass transfer coefficient (Meikap et al., 2004). Therefore, it is important to determine the values of k_L and a separately, to enable a proper characterization of the mass transfer in a bubble column with/without internals.

In general, the addition of internals enhances the mass transfer coefficient for increasing superficial gas velocities. Meikap et al. (Meikap et al., 2002, 2004) used a diffusion controlled chemical reaction, for determination of the mass transfer characteristics in a multi-stage bubble column. They studied the effect of superficial gas and liquid velocity on $k_L a$ and k_L. $k_L a$ was found to be in order of 0.12 to 0.30 s^{-1} and the value of k_L varied from $4.2{\times}10^{-2}$ to $6{\times}10^{-2}$ m/s for the modified bubble column, staged with contraction/expansion disks. The mass transfer coefficient values for the modified column are always higher than those for a conventional bubble column without internals.

Lakota et al. (Lakota et al., 2001, 2002) investigated the liquid phase back-mixing and mass transfer characteristics for a structured packing composed of Sulzer static mixers (SMV 16). Steady-state dispersion measurements in the structured bubble column with KCl as a tracer revealed a 50% reduction in the liquid axial dispersion coefficient at low gas velocities and only 20% reduction at high gas velocities. Steady-state measurement of oxygen concentration using a polarographic electrode was performed to determine the volumetric mass transfer coefficient ($k_L a$), in both empty and structured columns. $k_L a$ was found to increase with increasing superficial gas velocity and had a weak dependence on the superficial liquid velocity.

Höller et al. (2001) used woven fibrous layers and studied the hydrodynamic parameters such as residence time distribution (RTD) and $k_L a$ in an air-water system, for varying superficial gas and liquid velocities. They studied the effect of the major design parameters such as the thread diameter, the distance between woven threads and the distance between fibrous layers. They found that the volumetric mass transfer coefficient $k_L a$ in the staged bubble column is a function of both gas and liquid superficial velocity, contrary to conventional bubble columns. At superficial gas velocities above 150 mm/s, the $k_L a$ values are independent of the fabric structure as the gas distribution is less favorable.

Sujatha et al. (2015) studied a novel Micro-Structured Bubble Column (MSBC) reactor, where the micro-structuring is realized by using a wire mesh. They performed experiments by varying the superficial gas velocity from 5-50 mm/s and determined different flow regimes in the MSBC reactor by visual observation. Three different regimes with respectively bubble cutting, bubble cutting followed by re-coalescence and gas pocket formation were observed for different wire meshes. An advanced digital image analysis technique was used to determine the effect of wire mesh on bubble size distribution and gas holdup.

In this work, the mass transfer performance of a micro-structured bubble column (MSBC) reactor will be evaluated by determination of the volumetric mass transfer coefficient ($k_L a$) and interfacial area (a). The mass transfer phenomena in a pseudo-2D bubble column are investigated for the absorption of oxygen from air into water. The concentration of oxygen is measured by using a non-intrusive planar optical oxygen sensor. The effect of internals (different wire meshes and a Sulzer packing) on the mass transfer is studied for superficial gas velocities ranging from 5 to 40 mm/s.

3.2 Digital Image Analysis

The digital image analysis (DIA) technique used in this work, was developed by Lau et al. (2013a); Sujatha et al. (2015). This technique is used to determine the equivalent diameter of bubble d_{eq}, the bubble size distribution and the gas holdup in a bubble column reactor. The proposed image analysis algorithm consists of five major steps: a) image filtering b) separation of bubbles in solitary and overlapping/bubble clusters based on the roundness of bubbles c) splitting of solitary bubbles into small bubbles (10 to 100 square pixels) and large bubbles (larger than 100 square pixels). This is done by image normalization using CLAHE (contrast limited adaptive histogram equalization) and stretching pixel values over the entire image range resulting in an image with only small bubbles. d) watershed segmentation for processing overlapping bubbles and clusters, and e) combination of solitary and overlapping bubble images. Specific details on the individual image processing steps can be found in the work of Lau et al. (2013a); Sujatha et al. (2015).

The area of each detected bubble object is used to determine the associated sphere equivalent bubble diameter.

$$d_{eq} = \sqrt[2]{\frac{4A}{\pi}} \tag{3.4}$$

Subsequently, the Sauter mean diameter is calculated from the measured equivalent diameters using the following equation. It is commonly used for the calculation of gas holdup and interfacial area.

$$d_{32} = \frac{\sum_{k=0}^{n} d_{eq,k}^3}{\sum_{k=0}^{n} d_{eq,k}^2} \tag{3.5}$$

The integral gas holdup can be calculated from the DIA using the method used by Lau et al. (2013b):

$$\varepsilon_g = \frac{\sum_{k=0}^{n} \frac{\pi d_{32,k}^3}{6}}{(W - 2d_{32})(H - 2d_{32})D} \tag{3.6}$$

where $W \times D \times H$ are the dimensions of the field of view.

The DIA technique is subject to different error sources, such as imaging errors, image filtering errors, separation errors, segmentation error and errors due to a limited resolution. For detected objects between 10-30 pixels, the maximum and minimum errors are estimated to be +2% and -6% respectively. For objects greater than 30 pixels, the error is estimated to be between +0.5% and -1.0%.

3.3 Methods for determination of liquid-side volumetric mass transfer coefficient

There are different methods for measuring the liquid-side volumetric mass transfer coefficient. The measurement of oxygen concentration in an air-water system is a commonly used procedure. Different methodologies have been documented in the literature for the measurement of oxygen transfer rate. They can be broadly classified as steady-state methods and dynamic methods (Clarke, 2013). Steady-state methods involve the determination of the oxygen transfer rate under conditions of constant dissolved oxygen concentration. Dynamic methods (Dunn and Einsele, 1975) are frequently used for determining k_La by measuring the transient change of dissolved oxygen concentration in response to a step change in the input gas (e.g. air). An important point of attention in dynamic methods is the procedure for degassing the liquid. That is, the liquid should be de-oxygenated by flushing it with an inert gas (e.g. nitrogen) before starting the air flow.

In applying the dynamic method it is essential that the sensor response time is negligible. The sensor response time (the time needed to record 63% of a step change in input gas) can be assumed negligible, when it is significantly lower than the reciprocal of k_La (Van't Riet, 1979). When the response time is large though, various models can be applied to account for the response lag, ranging from first-order probe dynamics to more complex models involving diffusion.

Several alternative dynamic methods exist, such as the modified-gassing out method (Chang et al., 1989), the random pulsed dynamic method (Gauthier et al., 1991), the sulfite oxidation method (Ruchti et al., 1985) and the pressure step method (Linek et al., 1989).

3.4 Calculation of volumetric mass transfer coefficient

In this work, the volumetric mass transfer coefficient (k_La) is calculated using the data obtained by dynamic oxygen absorption method. The dissolved oxygen concen-

tration in the liquid phase is measured by using a non-intrusive planar oxygen sensor (PSt3 from PreSens GmBH, Regensburg, Germany). The special sensor does not have any optical isolation and was fabricated as such to provide a fast response times ($t_p \leq 5$ s as reported by the supplier). The working of the oxygen sensor is based on the principle of dynamic fluorescence quenching. The sensor contains a fluorescent dye that is excited by the electromagnetic waves of a specific wavelength. Depending on the concentration of oxygen present in the liquid film, the luminescent response of the sensor varies. The interaction of oxygen molecules with the luminophore in its excited state results in a radiation-less deactivation, and hence decreases its measurable luminescence signal. An optical fiber probe receives the signal and sends it to the Fibox 3 device that transmits the signal to the computer via an RS-232 channel. The dissolved oxygen concentration versus time data is stored in the computer for post-processing. A schematic illustration of the oxygen concentration measurement is shown in Fig. 3.1.

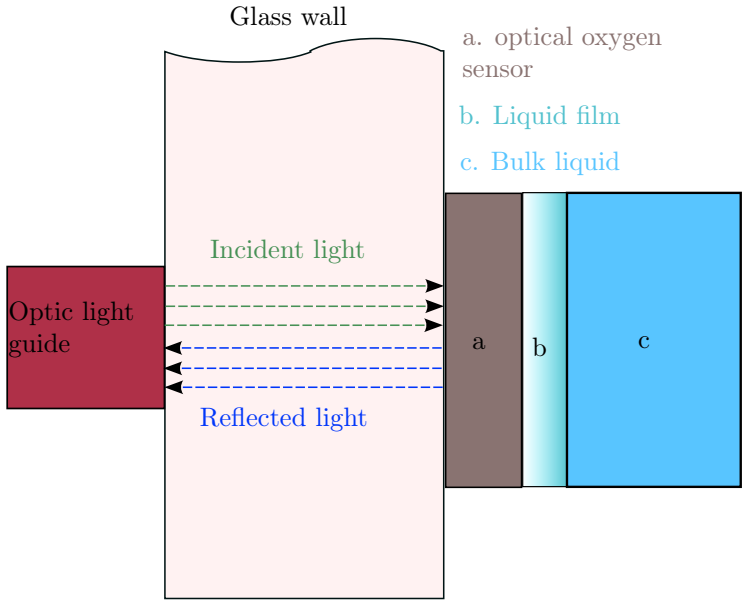

Figure 3.1: Schematic illustration of the oxygen concentration measurement.

3.4.1 Determination of sensor response time

Here, we define the response time of the sensor (t_p) as the time taken to measure 90% change in concentration when the sensor is subjected to a step change from water with 0% oxygen to 100% oxygen saturated water. The response time of the sensor represents the lag of the sensor in measuring the actual oxygen concentration in the liquid phase. The response time can also be expressed as the sensor constant ($k_p = 1/t_p$).

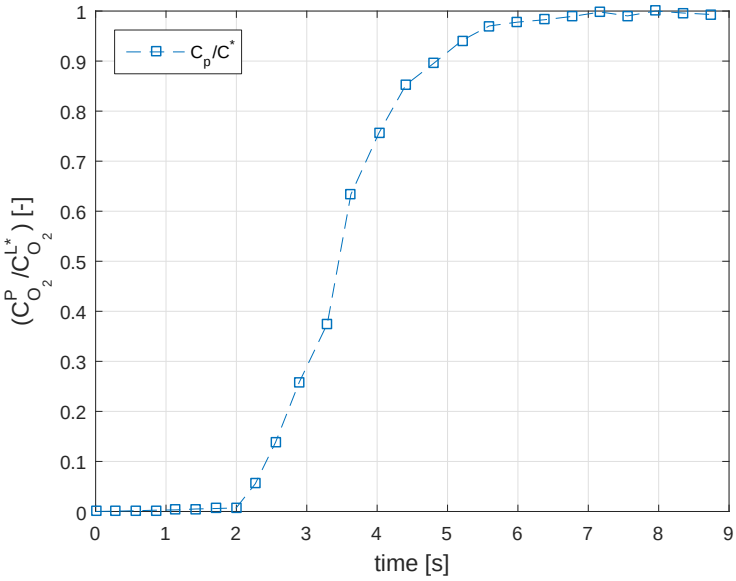

Figure 3.2: Determination of sensor response time, t_p.

The sensor response time is determined from Fig. 3.2. It shows the concentration measured by the sensor on imposing a step change in concentration from 0% oxygen to 100% oxygen saturated water at $t = 2$ s. The time taken for the concentration to reach 90% is approximately 3 seconds. This value is within the range of t_p reported by the manufacturer (i.e.$t_p \leq 5$ seconds). The corresponding sensor constant is $k_p = 1/t_p = 0.33s^{-1}$.

3.4.2 Modeling and assumptions

The k_La values are obtained from the dissolved oxygen concentration using the following assumptions:

1. The system is perfectly mixed.

2. Depletion of oxygen in the gas phase due to mass transfer limitations can be neglected. This condition is valid when the characteristic time for depletion t_d is larger than the characteristic time for mass transfer t_m.

$$t_d = \frac{\varepsilon_g}{1-\varepsilon_g} \frac{(\frac{k_H}{RT})}{k_La} \tag{3.7}$$

$$t_m = (k_La)^{-1} \tag{3.8}$$

3. The rate limiting step for mass transfer is located on the liquid side i.e. gas side resistance is negligible.

4. A first order model can be used to describe the sensor dynamics, when the sensor constant (k_p) is close to the characteristic value for mass transfer coefficient (k_La). If $k_p \gg k_La$, k_p is negligible as there is no sensor lag in measurement of dissolved oxygen concentration.

The dissolved oxygen concentration measured by the sensor, $C^P_{O_2}$ is related to the dissolved oxygen concentration in the liquid, $C^L_{O_2}$ by the following first order model:

$$\frac{d\,C^P_{O_2}}{dt} = k_p\,(C^L_{O_2} - C^P_{O_2}) \tag{3.9}$$

The concentration of oxygen in the liquid is modeled using the following equation.

$$\frac{d\,C^L_{O_2}}{dt} = k_La\,(C^{L*}_{O_2} - C^L_{O_2}) \tag{3.10}$$

Solving the above equations 3.9 and 3.10 results in the following solution:

$$\frac{C^P_{O_2}}{C^{L*}_{O_2}} = 1 - \frac{1}{k_p - k_La}\,(k_p\,e^{-k_La\,t} - k_La\,e^{-k_p\,t}) \tag{3.11}$$

Rearranging and differentiating the above equation with respect to time results in the following equation for k_La.

$$\frac{-d\,ln(1 - \frac{C^P_{O_2}}{C^{L*}_{O_2}})}{dt} = \frac{k_La\,(1 - e^{(-k_p + k_La)\,t})}{1 - \frac{k_La}{k_p}\,e^{(-k_p + k_La)\,t}} \tag{3.12}$$

Typical values of k_La in the bubble columns are $\mathcal{O}(10^{-3})$ and k_p is $0.33s^{-1}$. Under the condition that $k_p \gg k_La$, k_p is negligible in Eqn. 3.12. Hence, the k_La can be determined from the slope of the plot between the logarithm of $1 - \frac{C^P_{O_2}}{C^{L*}_{O_2}}$ versus time as given by Eqn. 3.13.

$$\frac{-d\,ln(1 - \frac{C^P_{O_2}}{C^{L*}_{O_2}})}{dt} = k_La \tag{3.13}$$

Fig. 3.3 shows a typical oxygen concentration profile versus time (left axis) and the natural logarithm of $1 - \frac{C^P_{O_2}}{C^{L*}_{O_2}}$ versus time (right axis). The value of k_La is determined from the slope of the fit through the points and the associated confidence interval is determined.

3.5 Material and methods

3.5.1 Experimental setup

A flat pseudo-2D bubble column reactor of dimensions (width W=0.2 m, depth D=0.03 m, height H=1.3 m) is chosen for experiments. A schematic figure of the

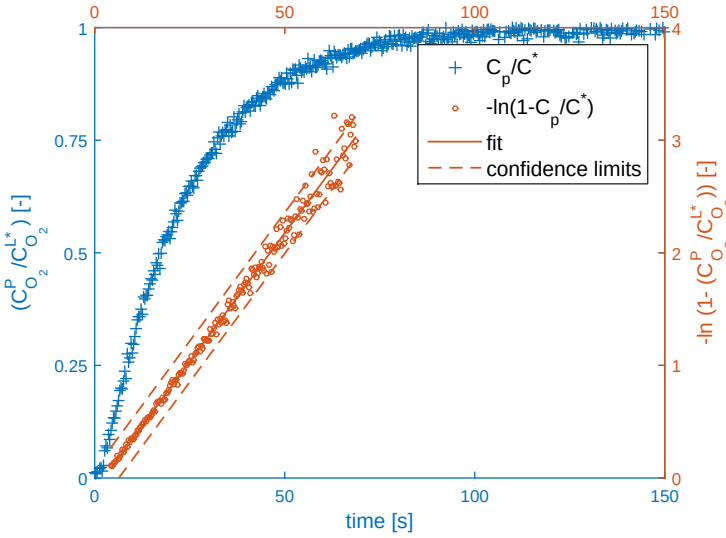

Figure 3.3: Determination of volumetric mass transfer coefficient, $k_L a$. Confidence limits are ± 10%.

experimental setup is shown in Fig. 3.4. Experiments are carried out in the MSBC for an air-water system. The reactor walls are made of transparent glass to enable visual observation. The glass walls have slits on the front and the back faces (the slit dimensions are 200 mm×15 mm) at a height of 1 m from the bottom, to allow for the liquid to overflow to a storage vessel. A liquid pump can be used to recirculate the liquid into the column at a set flow-rate, through a liquid distributor plate. The liquid distributor plate has perforations of 3.2 mm diameter, arranged in a 60 degree staggered configuration with a distance of 4.5 mm between neighboring perforations. The gas is fed into the column via a group of fifteen gas needles centrally arranged in the distributor plate. The needles have a length, L = 50 mm, an inner diameter ID = 1 mm and an outer diameter OD = 1.5875 mm. The needles extend 10 mm above the bottom plate and are spaced with a center-to-center distance of 9 mm. An array of five needles is classified as a group, and each group of nozzles is connected to a mass flow controller. Subsequently, three mass flow controllers are used to control the gas flow rates in the column. The gas is supplied into the column with a quiescent liquid for all experiments, with an initial liquid height of 1 m.

Micro-structuring in the reactor is realized by means of insertion of various square meshes made of thin wires. The wire mesh can be mounted on the column by using the modular insert, designed for this purpose. The modular insert design allows full flexibility to attach one or more wire meshes at different locations of the insert. The dimensions of the column including the insert are as follows: width=0.14 m, depth=0.03 m, height=1.3 m. In this case the location of the wire mesh was fixed at a height of 0.518 m. The oxygen sensor is placed at 0.63 m from the bottom based

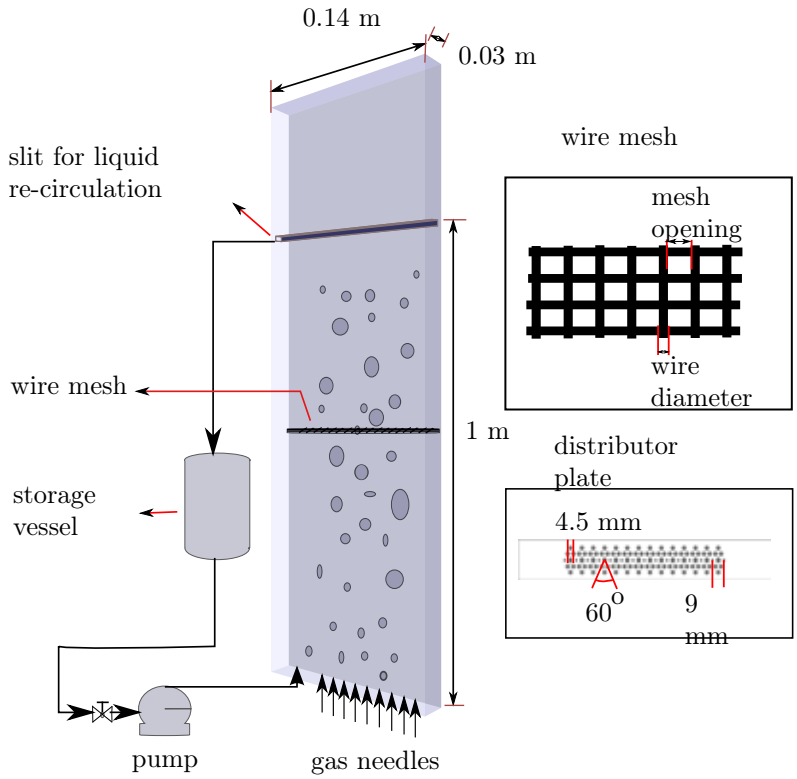

Figure 3.4: Schematic illustration of the micro-structured bubble column used in this work.

on the recommendation of Shioya and Dunn (1978) that the sensor must be placed between 40-80% of the total height. The oxygen concentration measured by the sensor is dependent on the temperature, pressure and salinity of the liquid. A temperature probe is immersed in the liquid to record the temperature during measurement, to compensate for temperature effects on concentration.

3.5.2 Calibration of optical oxygen sensor

Calibration of the sensor is required to relate the measured luminescence intensity signals to the oxygen concentration. A linear two-point method is used for calibration of the optical oxygen sensor. That is, two water solutions are prepared. The first solution is an oxygen-free water solution that is prepared by stripping the oxygen from the water by bubbling nitrogen gas through water for about 30 minutes. The second solution involves a air-saturated water solution, which is obtained by bubbling air through the water for a duration of 30 minutes. The sensor is calibrated by using these two standard solutions and the calibration data is stored in the software.

3.5.3 Experimental procedure

During the start of the experiments, the water is stripped of oxygen by using a constant flow of nitrogen gas until the dissolved oxygen concentration is negligible. Once the oxygen is completely removed the nitrogen gas flow-rate is set to the desired flow-rate for experiments to stabilize the hydrodynamics of the system, and the gas is switched from nitrogen to air. The measurement of the dissolved oxygen concentration is started as soon as the gas is switched to air and the experiment is stopped when the water is saturated with oxygen.

A CMOS camera with resolution of 2016 $\times$ 2016 *pixels* is used to capture images of the two-phase bubbly flow by using back-lighting to obtain maximum contrast between the bubbles and the background. The MSBC is divided into five different sections for the purpose of imaging. Images from each section has a size of 0.21 m$\times$0.14 m and a small overlap of 0.05 m. The resolution of the image is 0.11 mm/pixel. Objects with areas smaller than 10 square pixels cannot be detected properly and are discarded with the aid of a noise filter. The images are processed by the DIA technique discussed in Section 3.2.

3.6 Results and discussion

Experiments were carried out in an air-water system for various superficial gas velocities ranging from 5 mm/s to 40 mm/s. The mass transfer characterization of a micro-structured bubble column is done by obtaining results of volumetric mass transfer coefficient (k_La) and interfacial area (a). These quantities are determined by the dynamic absorption method and digital image analysis respectively. Results of the gas holdup and interfacial area are obtained from DIA (Sujatha et al., 2015) for different wire mesh configurations. Additional DIA experiments are performed to determine the interfacial area for the Sulzer packing and the results are included in this work.

3.6.1 Visual observation

Visual observation of the recorded images provides an insight into the overall behavior of the packing with respect to hydrodynamics and bubble cutting. Figures 3.5, 3.6 and 3.7 are obtained for different internals. All these internals were tested at a superficial gas velocity of 40 mm/s and respectively contain a wire mesh with a 3.7 mm mesh opening, two wire meshes with a 3.7 mm mesh opening stacked at a distance of 10 mm and a Sulzer packing. In the wire mesh with a mesh opening of 3.7 mm the bubbles pass through the mesh easily due to the low hydrodynamic resistance offered by the wire mesh (small wire diameter and large open area) as seen in Fig. 3.5. Small bubbles can be found above and below the wire mesh, due to bubble breakup at high velocity and bubble cutting by the wire mesh. The bubbles that are cut by the wire mesh are dragged down the mesh due to liquid back-mixing. From Fig. 3.6, it is visible that the hydrodynamic resistance increases significantly by stacking wire meshes, as bubbles decelerate and tend to accumulate in the form of gas pockets below the mesh. The Sulzer packing with a small open area and dense packing also offers a higher resistance to bubble flow, as seen in Fig. 3.7 from the formation of gas

pockets and larger gas holdup below the packing. The bubbles tend to re-coalesce above the Sulzer packing leading to a decrease in the interfacial area.

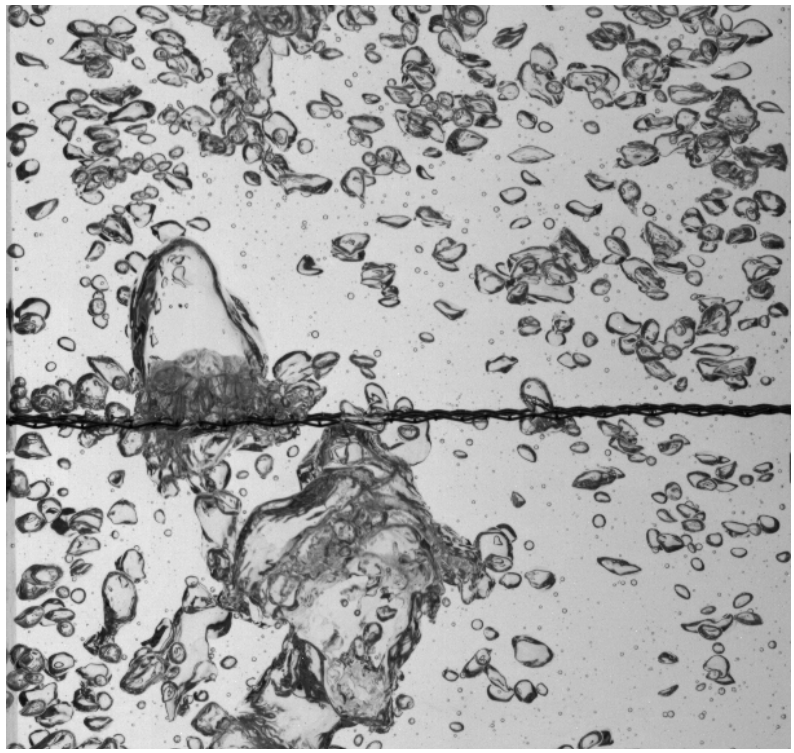

Figure 3.5: Bubble cutting by a single wire mesh with a mesh opening of 3.7 mm at a superficial gas velocity of 40 mm/s.

3.6.2 Interfacial area using Digital Image Analysis (DIA)

The interfacial area (a) can be calculated according to Eqn. 3.14, from the values of the gas holdup and the Sauter-mean diameter determined by digital image analysis. From Fig. 3.8 it can be seen that the interfacial area is a function of the superficial gas velocity and the configuration of the internals. The interfacial area with wire meshes are found to be higher than without a wire mesh, as a result of bubble cutting. The wire mesh with an opening of 3.7 mm has the maximum interfacial area over the entire range of superficial gas velocities. The lower interfacial area for the Sulzer packing can be attributed to the undesirable bubble coalescence above the Sulzer packing, as it significantly reduces the residence time of bubbles in the MSBC reactor. For superficial gas velocities above 25 mm/s, the results of the interfacial area determined by the image analysis technique are unreliable due to poor bubble detection at high

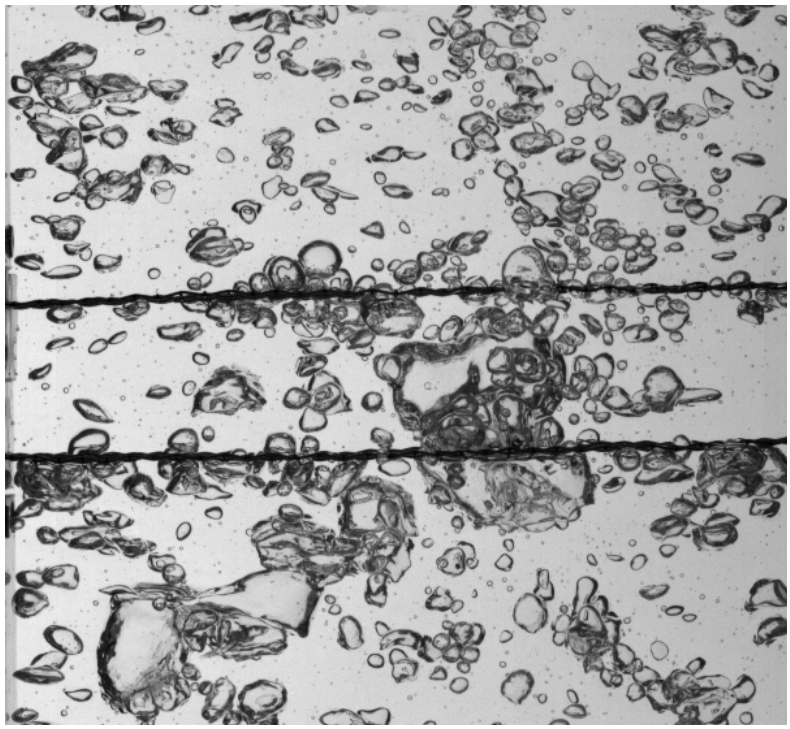

Figure 3.6: Bubble cutting by two stacked wire meshes with a mesh opening of 3.7 mm at a superficial gas velocity 40 of mm/s. The mesh spacing is 10 mm.

gas holdup.

$$a_{DIA} = \frac{6\,\varepsilon_{G,DIA}}{d_{32}} \tag{3.14}$$

It can be seen that the correlation of Akita and Yoshida under-predicts the interfacial area at low superficial gas velocities and it has a reasonable estimate at higher superficial gas velocities. It should be noted that the discrepancy may be due to differences in the reactor geometry, as these may influence the hydrodynamics and the bubble size distribution.

3.6.3 Volumetric mass transfer coefficient using oxygen absorption

The volumetric mass transfer coefficient ($k_L a$) for different wire mesh lay-outs were obtained using the dynamic absorption degassing method and the obtained results are shown in Fig. 3.9. It can be observed that the presence of the wire mesh increases the volumetric mass transfer coefficient in all experiments. This is probably due to bubble oscillations induced by the presence of wire meshes, which leads to higher mass transfer rates due to modification of the concentration profile around the bubble (Martín et al., 2009).

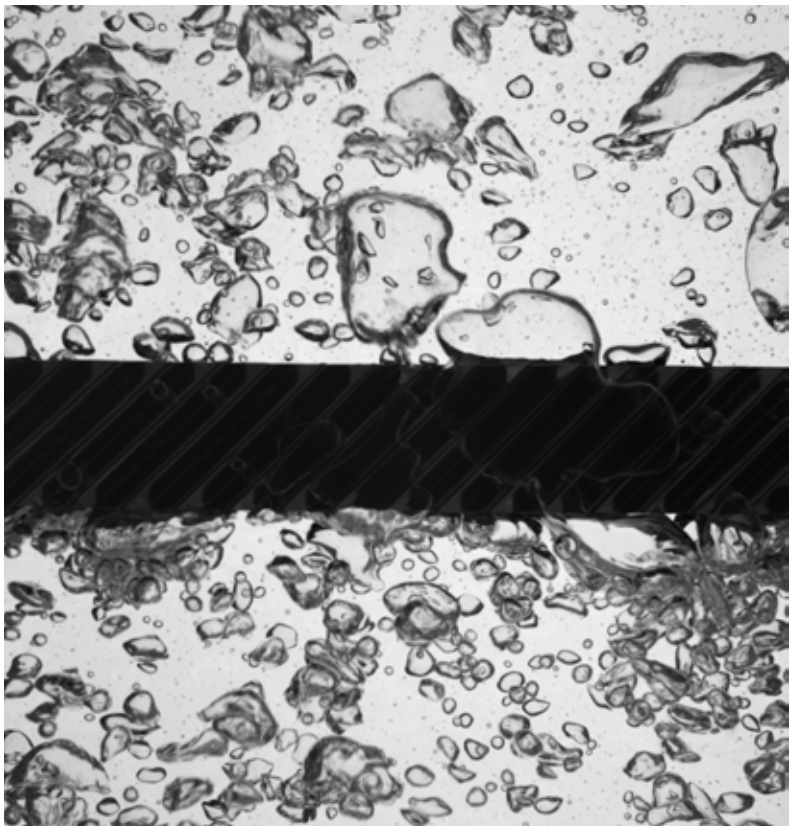

Figure 3.7: Bubble cutting by a Sulzer packing at a superficial gas velocity of 40 mm/s.

In Fig. 3.9, the volumetric mass transfer coefficient for the different forms of micro-structuring are shown as a function of superficial gas velocity. It can be seen that the superficial gas velocity is directly proportional to the volumetric mass transfer coefficient. The increase in k_La with superficial gas velocity is mainly due to the increase in gas holdup and hence in the interfacial area in the bubble column. This trend has also been observed in the past for bubble columns without internals (Akita and Yoshida, 1973, 1974). The experimentally obtained results are compared to the correlation provided by Akita and Yoshida (Eqn. 3.3).

At low superficial gas velocity until 20 mm/s, it can be seen that different internals have almost similar performance. The effect of micro-structuring is mainly visible at higher superficial gas velocities (30 - 40 mm/s), as the wire meshes exhibits a positive effect on mass transfer and the Sulzer packing has a negative impact. It can be seen that the 3.7 mm mesh opening offers the best performance for the range of gas superficial velocities studied. An increase in k_La of 25% is observed at high superficial

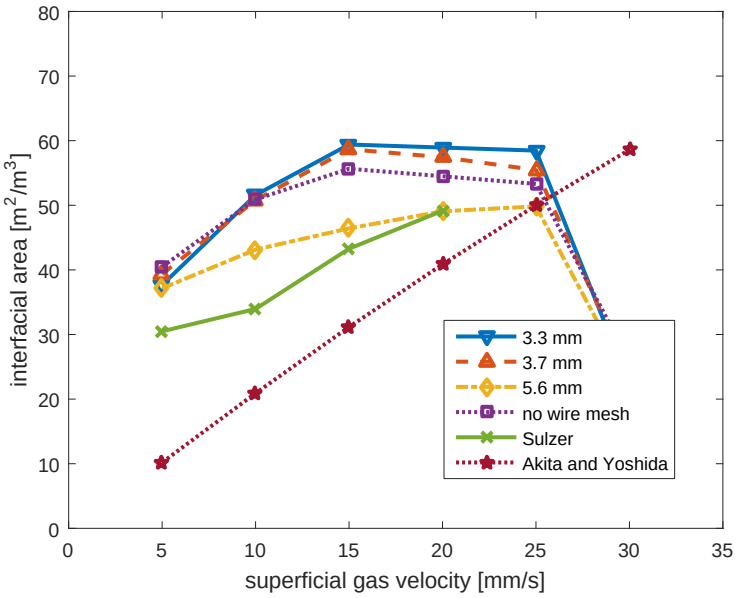

Figure 3.8: Interfacial area: Effect of varying wire mesh.

gas velocity of 40 mm/s with the 3.7 mm mesh opening, which is due to the breakdown of the bubble plume. Better performance of the wire mesh over the Sulzer packing can be explained by its open structure, as it offers a lower hydrodynamic resistance to the rising bubbles. The Sulzer packing has a high resistance to bubbly flow leading to the formation of gas pockets, which reduces the effective area available for bubble cutting.

The effect of stacking two wire meshes with 3.7 mm mesh opening at a distance of 10 mm is shown in Fig. 3.10, where the results of no mesh, and one and two meshes are compared. It can be seen that the bubble cutting in a stacked double mesh configuration is similar to the case with a single mesh at low gas velocities (10 - 30 mm/s). However, at higher gas velocities (40 mm/s) the double mesh configuration performs worse due to bubble re-coalescence and formation of gas pockets on sides of the mesh as seen in Fig. 3.6. The performance of the stacked mesh configuration may be optimized by adjusting the relative distance between the meshes and the mesh design parameters (wire diameter and mesh opening), but this is beyond the scope of this paper.

3.6.4 Individual mass transfer coefficient using oxygen absorption

The 'individual' mass transfer coefficient (k_L) is calculated from the earlier obtained k_La and interfacial area. Figure 3.11 shows the results for two superficial gas velocities (10 and 20 mm/s) and different internals. It can be seen that the value of k_L increases in the presence of the wire mesh. It also increases slightly with increasing

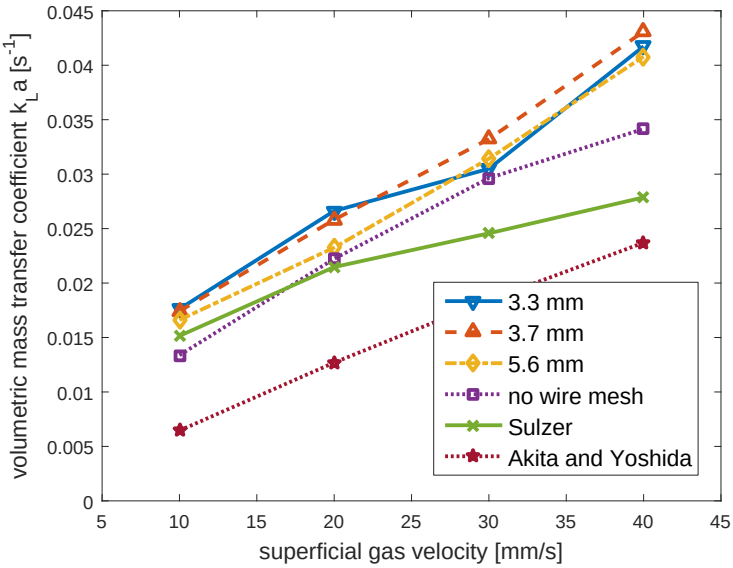

Figure 3.9: Volumetric mass transfer coefficient: effect of wire mesh opening.

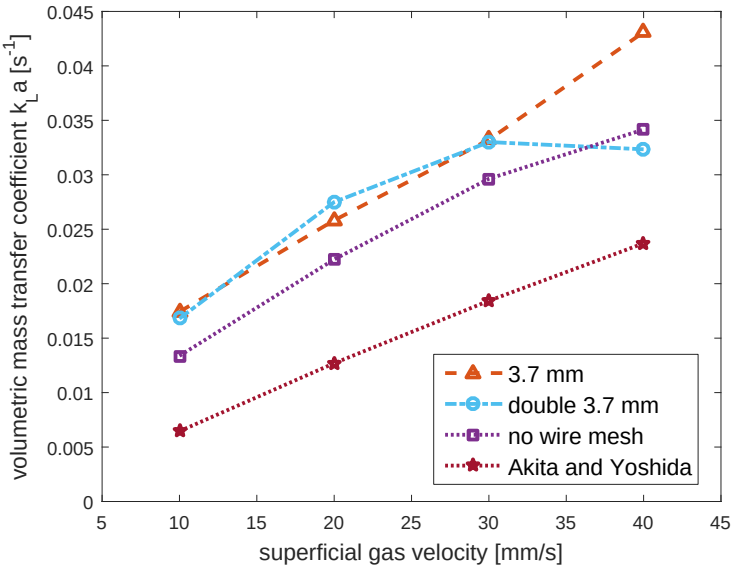

Figure 3.10: Volumetric mass transfer coefficient: effect of number of wire meshes.

superficial gas velocity for the different mesh configurations. This is probably due to the enhancement of the liquid turbulence and the associated bubble shape oscillations.

The individual mass transfer coefficient in a Sulzer packing is found to decrease

with increasing superficial gas velocity, contrary to the behavior of the wire mesh. The decrease of k_L in the Sulzer packing is probably related due to the increase in interfacial area between 10 to 20 mm/s. The k_L determined by Akita and Yoshida correlation (Eqn. 3.2 and Eqn. 3.3) has a similar trend as the Sulzer packing for increasing superficial gas velocities. This reduction in k_L can also be explained by an increment in the interfacial area and gas holdup with increasing superficial gas velocity. More data on k_L for superficial gas velocities above 20 mm/s are required to perform a more detailed analysis. However, this is not possible due to limitations in the DIA technique for the determination of a.

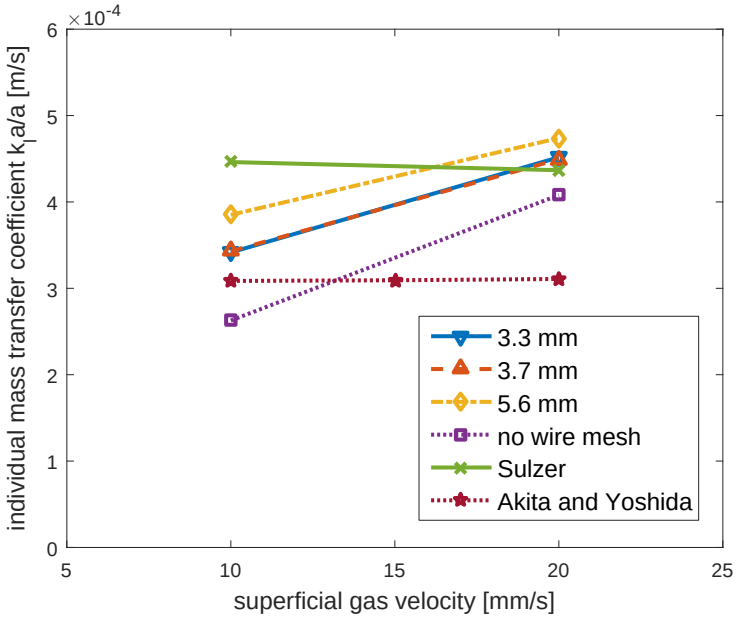

Figure 3.11: Individual mass transfer coefficient using oxygen absorption.

3.7 Conclusions

The effect of bubble cutting on physical absorption is studied for an air-water system, by measuring the volumetric mass transfer coefficient (k_La). It is determined by dynamic oxygen absorption method, which requires the transient measurement of the dissolved oxygen concentration. The latter was measured using a non-intrusive planar optical sensor. The response time of the optical sensor is experimentally determined to be 3 seconds. k_La values are determined by neglecting the sensor constant (k_p), since $k_p \gg k_La$. The measured values of k_La are compared for a bubble column respectively without wire mesh, with one or two wire meshes and Sulzer packing.

It can be seen that the wire mesh and Sulzer packings have comparable performance in terms of k_La, at low superficial gas velocities until 20 mm/s. However,

the wire meshes have a considerably better performance as the velocity is increased above 20 mm/s. The implementation of a single wire mesh (3.7 mm mesh opening) is shown to increase k_La by 25% at a high superficial gas velocity of 40 mm/s. The main advantage of the wire mesh is its open structure in comparison with the Sulzer packing, as it offers lower hydrodynamic resistance to flow of bubbles. Low hydrodynamic resistance is essential for efficient cutting behavior and better performance in terms of mass transfer. The double wire mesh configuration shows a drop in k_La at 40 mm/s, due to bubble re-coalescence and higher flow resistance offered by this configuration.

The individual mass transfer coefficient (k_L) for a wire mesh increases with superficial gas velocity. The reduction of k_L in the Sulzer packing can be mainly attributed to the increase in a with superficial gas velocity. It is not possible to obtain data on k_L for superficial gas velocities above 20 mm/s, due to limitations in the DIA technique for determination of a.

Nomenclature

ε	gas holdup,	$[-]$
d	diameter,	$[m]$
W	width,	$[m]$
H	height,	$[m]$
D	depth,	$[m]$
D_c	column equivalent diameter,	$[m]$
D_{AB}	diffusivity of gas (A) into liquid (B),	$[m^2/s]$
A	area,	$[m^2]$
g	gravity,	$[m/s^2]$
u	superficial gas velocity,	$[m/s]$
h	height of liquid-gas dispersion,	$[m]$
t_d	characteristic time for depletion,	$[s]$
t_m	characteristic time for mass transfer,	$[s]$
t_p	sensor response time,	$[s]$
k_H	Henry's constant,	$[L.atm/mol]$
k_L	individual mass transfer coefficient,	$[m/s]$
k_La	volumetric mass transfer coefficient,	$[1/s]$
k_p	probe constant,	$[1/s]$
R	gas constant,	$[L.atm/K.mol]$
T	temperature,	$[K]$
a	interfacial area,	$[m^2/m^3]$
t	time,	$[s]$
ρ	density,	$[kg/m^3]$
σ	surface tension,	$[N/m]$
μ	dynamic viscosity,	$[kg/m.s^2]$
ν	kinematic viscosity = μ/ρ,	$[m^2/s]$
$C^P_{O_2}$	concentration of oxygen measured by sensor,	$[mol/lit]$
$C^L_{O_2}$	concentration of oxygen in liquid phase,	$[mol/lit]$

$C_{O_2}^{L*}$	concentration of oxygen at saturation,	$[mol/lit]$
eq	equivalent	
G	gas	
L	liquid	
k	index	
H	height expansion	
DIA	Digital Image Analysis	
f	final	
0	initial	
Weber number	$We = \left(\frac{gD_c^2\rho_L}{\sigma}\right)$	
Galileo number	$Ga = \left(\frac{gD_c^3\rho_L}{\nu_L^2}\right)$	
Froude number	$Fr = \frac{u_G}{\sqrt{gD_c}}$	
Schmidt number	$Sc = \left(\frac{\nu_L}{D_{AB}}\right)$	

CHAPTER 4

Hydrodynamics of bubble cutting in dodecane-nitrogen system

Bubble column reactors are one of the most widely used types of multiphase reactors in the chemical industry. They are used for both two-phase (gas-liquid) and three-phase (gas-liquid-solid) processes. Despite the advantages of simple construction and relative ease of operation, they have some inherent disadvantages. To overcome the disadvantages of a conventional slurry bubble column reactor, a novel reactor concept is proposed in this work. It is a micro-structured bubble column reactor (MSBC), where the micro-structuring is realized by immersing a wire-mesh. This mesh is intended to break the gas bubbles and hence increase the gas-liquid contact area in the bubble column, by employing a suitable wire-mesh geometry. In addition the wire-mesh can be coated with a catalyst to perform heterogeneous catalytic reactions.

The scope of this research is to study the effect of the wire-mesh geometry on the bubble cutting process in a dodecane ($C_{12}H_{26}$) - nitrogen (N_2) system. The extent of bubble break-up depends on mesh opening and wire diameter. The objective of the present work is to obtain detailed experimental data to quantify the effect of the wire mesh on the bubble size distribution in a dodecane-nitrogen system. These experimental data can be used for the validation of detailed Euler-Lagrange models for laboratory bubble columns.

Experiments are conducted in the MSBC for different mesh configurations, for several superficial gas velocities. Experiments are performed with wire meshes with an open area exceeding 60%. Bubble cutting takes place at low superficial gas velocity and small mesh openings (2.7 mm) due to the low surface tension in the dodecane-nitrogen system. This is different from aqueous systems where bubbles are larger due to higher surface tension. Upon increasing the number of mesh stages in the MSBC,

the flow regime in the bubble column changes from heterogeneous to homogeneous. This transition is observed due to an increase in gas holdup as a result of bubble cutting or breakup.

4.1 Introduction

Organic chemicals have a great relevance in the chemical industry, involving processes such as absorption, oxidation, alkylation, Fischer-Tropsch synthesis, etc. In particular, oil and gas are the basic raw materials used for the synthesis of organic commodity chemicals. Many of these processes involve conventional or modified bubble column reactors. Although the bubble columns are widely used due to their simple design and ease of operation, scale-up of these reactors is quite difficult due to the complex flow characteristics and partially understood impact of design variables such as column diameter, height, operating pressure, operating temperature, inlet distributor design, etc. However, their undesirable characteristics at high flow-rates including a considerable degree of back-mixing in the gas and liquid phase, low interfacial area due to high coalescence rates and short gas phase residence time. Several alternative configurations are proposed in literature (Shah et al., 1982; Baird, 1992; Deen et al., 2000; Kantarci et al., 2005), to avoid the undesirable effects for industrial operation.

Sujatha et al. (2015) have proposed a novel micro-structured bubble column reactor to overcome the effect of conventional bubble columns. They have performed experiments in a laboratory scale MSBC reactor to study the effect of the wire mesh configuration and superficial gas velocity. Three hydrodynamic regimes were identified for bubbly flow in a MSBC with a wire mesh in an air-water system for superficial gas velocities in the range of 5 to 50 mm/s.

Tang and Heindel (2004) suggested that regular tap water can cause significant reproducibility problems in air-water two-phase studies. They observed the time-dependent variation of gas holdup which was related to water quality, column operation mode, sparger orientation and superficial gas and liquid velocities. They attributed this time-dependency to coalescence inhibition caused by the volatile substances present in tap water. Therefore, presence of contaminants in an aqueous system can inhibit or enhance the frequency of coalescence and breakup (Chaumat et al., 2007). The parameters such as bubble size and gas holdup are dependent on the physico-chemical parameters of the fluid such as density, viscosity and surface tension. The rate of bubble coalescence and breakup is also a function of liquid properties and the prevailing flow regime in the bubble column (Rollbusch et al., 2015). It is clear that contamination of water can alter the flow regime and affect the values of bubble size, gas holdup and mass transfer rates.

Maceiras et al. (2007) observed that bubbles in pure solvents (alcohol and alkanes) are non-spherical. The bubble rise velocity and mass transfer coefficient in such a system is close to the value expected for bubbles with a mobile interface. They also found that the purity of dodecane (90% vs. 99%) did not significantly affect the results. Therefore, dodecane is an ideal alternative to water for hydrodynamic studies in a micro-structured bubble column.

The scope of the current paper is to study the bubble cutting and hydrodynamics

of the micro-structured bubble column in a system with a pure organic liquid (dodecane-nitrogen system). The bubble size distribution is obtained with the aid of digital image analysis (DIA) technique. The effect of the superficial gas velocity and the number of wire mesh stages are investigated for different configurations.

This paper is organized as follows. We first describe the experimental setup and methods used for obtaining the results (i.e. digital image analysis technique, height expansion). Subsequently, the results are presented and discussed.

4.2 Material and methods

A flat pseudo-2D bubble column reactor of dimensions (width W=0.2 m, depth D=0.03 m, height H=1.3 m) is chosen for experiments. Experiments are carried out in the MSBC for an nitrogen-dodecane system. The reactor walls are constructed of transparent glass to enable visual observation by the eye or by using a high speed camera. The glass wall has a slit on the front and the back faces (slit dimensions are 200 mm×15 mm) at a height of 1 m from the bottom plate, to allow for the liquid to overflow to a storage vessel. A liquid pump is used to recirculate the liquid into the column at a set flow-rate, through a liquid distributor plate. The liquid distributor plate has perforations of 3.2 mm diameter, arranged in a 60 degree staggered configuration with a distance of 4.5 mm between neighboring perforations. The gas is fed into the column via a group of fifteen (15) gas needles centrally arranged in the distributor plate. The needles have a length (L) = 50 mm, inner diameter (I.D.) = 1 mm and outer diameter (O.D.) = 1.5875 mm. The needles extend 10 mm above the bottom plate and are spaced with a center-to-center distance of 9 mm. An array of five needles is classified as a group, and each group is connected to a mass flow controller. Subsequently, three mass flow controllers are used to control the gas flow rates in the column. Both the gas and liquid are fed into the reactor from the bottom by means of the distributor assembly. A schematic figure of the experimental setup is shown in Fig. 4.1.

Micro-structuring in the reactor is realized by means of thin wires of various dimensions arranged in a woven mesh structure. The wire mesh can be mounted in the column by using a modular insert, designed for this purpose. The modular insert design allows full flexibility to attach one or more wire meshes at different locations of the insert. The dimensions of the column including the insert are as follows: width=0.14 m, depth=0.03 m, height=1.3 m. The location of the wire mesh was fixed at a distance of 0.518 m from the bottom distributor plate for the single mesh configuration. In the multiple mesh configuration with ten mesh stages, the first mesh is placed at a distance of 0.05 m from the bottom and the consecutive nine meshes are placed at a distance of 0.05 m from each other. Table 4.1 outlines the overview of different wire-mesh lay-outs used for experiments.

Dodecane $CH_3(CH_2)_{10}CH_3$ (Sigma Aldrich ReagentPlus $\geq$ 99% purity) is used for the experiments. Table 4.2 shows the comparison of physico-chemical properties of water vs dodecane. Dodecane is non-polar and therefore has a lower surface tension (approximately one-third of that of water). The viscosity and density of the water and dodecane are however similar.

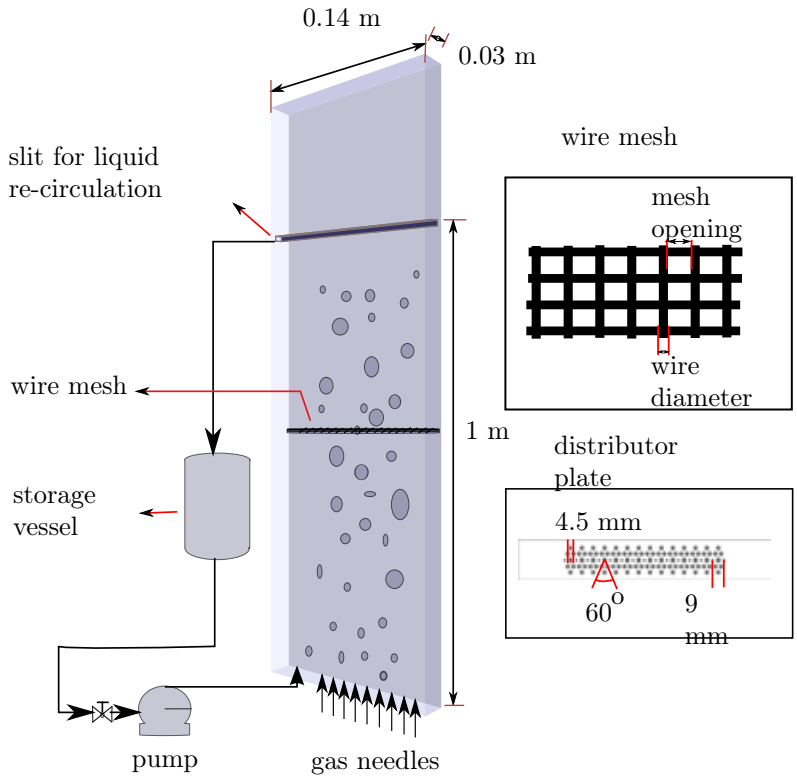

Figure 4.1: A schematic diagram of micro-structured bubble column.

Mesh #	wire diameter (mm)	mesh opening (mm)	open area (%)
6	0.55	3.7	76
8	0.50	2.7	71

Table 4.1: Overview of different wire meshes used for experiments.

4.2.1 Digital image analysis technique to determine bubble size distribution

The DIA technique (Lau et al., 2013a,b) was developed to determine the mean diameter d_{eq}, bubble size distributions and gas holdup in pseudo-2D bubble column reactor. Sujatha et al. (2015) improved the DIA technique to detect very small bubbles. The image analysis algorithm has four main operations: i) Image filtering ii) separation of bubbles into solitary and overlapping bubbles iii) segmentation of overlapping bubbles using a water shedding technique, and iv) combination of solitary and overlapping

property	water	dodecane	units
density @ 20 $°C$	998	749.5	kg/m^3
viscosity @ 20 $°C$	0.001	0.00134	$Pa.s$
surface tension	0.0728	0.0256	N/m
flash point		71	°C
boiling point	100	216.3	°C
freezing point	0	- 9.6	°C
vapor density (vs air)	0	5.96	

Table 4.2: Comparison of physico-chemical properties of water vs dodecane.

bubble images. Image filtering involves operations to remove the inhomogeneous illumination using an Otsu filter (Otsu, 1975). The Otsu filter determines the threshold for separating the bubbles from the background, by thresholding individual blocks of an image. The edges of the bubbles are detected by a Canny edge detection algorithm. The bubbles are separated into solitary bubbles and overlapping bubbles by using roundness as the separation criteria. The images with solitary bubbles are segmented by marking the bubbles, whereas the overlapping bubbles are segmented using the watershed algorithm proposed by Meyer (1994a).

The equivalent diameter was determined from the bubble area as follows:

$$d_{eq} = \sqrt[2]{\frac{4A}{\pi}} \tag{4.1}$$

The Sauter mean diameter of an image is calculated from the equivalent diameter using the following equation:

$$d_{32} = \frac{\sum_{k=0}^{n} d_{eq,k}^3}{\sum_{k=0}^{n} d_{eq,k}^2} \tag{4.2}$$

The probability density function (PDF) for a particular bubble diameter class is the ratio of number of bubbles in a particular diameter class(Δd_{eq}) to the sum of number of bubbles in all size classes. Therefore, the PDF of a particular size class (Δd_{eq}) is calculated from the number of bubbles and average bubble diameter as follows:

$$PDF_{\Delta d_{eq}} = \frac{N_{\Delta d_{eq}}}{\left(\sum_{\Delta d_{eq,min}}^{\Delta d_{eq,max}} N_{\Delta d_{eq,k}} \right) \Delta d_{eq}} \tag{4.3}$$

4.2.2 Height expansion technique for gas holdup

The gas holdup is determined for the dodecane-nitrogen system by liquid height expansion measurements. It is calculated by the following formula:

$$\varepsilon_{(g,H)} = \frac{h_f - h_0}{h_f} \tag{4.4}$$

where h_f is the height of the gas-liquid dispersion and h_0 is the initial height of the liquid.

4.2.3 Procedure

The experimental procedure for the dodecane-nitrogen system is as follows. The nitrogen flow is started first and the column is filled with pure liquid dodecane. The gas flow rate is set to achieve the desired superficial gas velocity. The column dynamics is allowed to stabilize for about five minutes and then 4000 images are recorded using a CMOS camera at a frequency of 50 Hz with a resolution of 2016×2016 $pixels$. The images of the two-phase bubbly flow are captured using back-lighting to enhance the contrast between the bubbles and the background. The entire height of the column is imaged in three sections (top, middle and bottom) for all velocities and mesh configurations. The images from each section have a size of 0.21 m×0.14 m and a small overlap of 0.05 m. Repeatability of the experiments was verified by checking the overlapping regions of images from different sections. The resolution of the image is 0.11 mm/pixel. Objects with an area smaller than 10 square pixels are filtered as noise. For a circular object with an area of 10 square pixels, the bubble diameter can be calculated as 3.6 pixels. Therefore, the minimum detectable bubble size by DIA technique is 0.39 mm at the applied spatial resolution. The height of the liquid surface is measured for all experiments in order to calculate the integral gas holdup.

4.3 Results

Experiments are performed for a dodecane-nitrogen system in a micro-structured bubble column to study the effect of superficial gas velocity, mesh opening and number of mesh stages. The overall hydrodynamics are first qualitatively inspected by using visual observation. Detailed results of the Sauter mean diameter and bubble size distribution are obtained by using an advanced digital image analysis technique. First, the effect of mesh type and superficial gas velocity is studied by comparing two different meshes (2.7 and 3.7 mesh opening) against the benchmark configuration of a bubble column without wire mesh. Then the effect of increasing the number of meshes is studied for a wire mesh with 3.7 mm mesh opening.

4.3.1 Visual observation

The bubbles in the images are observed to be small and non-spherical in shape. Since the surface tension of dodecane is one-third that of water, it is reasonable that bubbles are smaller (3 mm mean diameter) when compared to an air-water system (4 mm mean diameter). The surface tension has a direct effect on the bubble size

and shape. It also has an effect on the coalescence tendencies, as bubbles tend to coalesce to reduce the net surface energy. In liquids with low surface tension such as dodecane, the bubble coalescence rate is less compared to that of water due to the lower surface energies.

No gas pocket formation underneath the wire mesh was observed during experiments in the dodecane-nitrogen system as seen in Fig. 4.2 and Fig. 4.3. The disappearance of gas pockets in dodecane-nitrogen system can be explained by the lower surface tension, as low surface energy corresponds to the high deformability of the bubbles and also lower coalescence tendencies. Cutting without re-coalescence is observed for all superficial gas velocities above 5 mm/s. Increasing the number of meshes in the column reduces the heterogeneity in the bubble sizes. When the number of meshes is increased the flow regime shows a remarkable transition from the heterogeneous bubbly flow back to homogeneous flow with small bubbles rising evenly across the column (see e.g. Figs. 4.3a and 4.3d).

The effect of cutting is clearly observed in Fig. 4.4, especially in the top section of the column. There are many more small bubbles in cases with wire meshes as seen in all three sections of the column. It can be seen that the wire meshes offer a significant resistance to flow, thereby increasing the gas holdup. Images from the top section of the column are almost opaque as observed for all high superficial gas velocities. This indicates higher gas holdups compared to the no mesh case. The increase in gas holdup is due to the presence of small bubbles with low rise velocity and hence large residence times. Formation of froth at the top was observed during experiments with pure dodecane and this is characteristic of a non-coalescing system. (Lemoine et al., 2004).

4.3.2 Effect of mesh configuration

Fig. 4.5 shows that the cutting efficiency of a mesh with 2.7 mm mesh opening is the highest for superficial gas velocities of 10 and 15 mm/s. The bubble size distributions at higher gas velocities (>15 mm/s) for configurations with wire mesh, were difficult to extract due to the large amount of bubble overlaps at the high gas holdup. The detection is better for the case without wire mesh as the holdup is less and the background is clearly visible. In the cases with wire mesh, a cluster of small bubbles is sometimes falsely detected as a large single bubble. The effect of false detection on the Sauter mean diameter and bubble size distribution is suppressed by averaging bubble sizes over 4000 images. But in case the false detection occurs in every image, the accuracy of the results is reduced. In such cases, the actual bubble sizes are smaller than the values the interpreted ones for that particular wire mesh configuration. The present detection algorithm gives clear results until the superficial gas velocity of 15 mm/s. But there is a need for better measurement technique for high superficial gas velocities (>15 mm/s) and high gas holdups.

From the results of the volumetric probability density in Fig. 4.5b and 4.5d, it can be seen that for the cases with wire meshes the bubble diameter distribution is cut off at a bubble size of 6.3 mm. This is done to avoid the detection of large ghost bubbles within a cluster of small bubbles. The detection for configuration with no

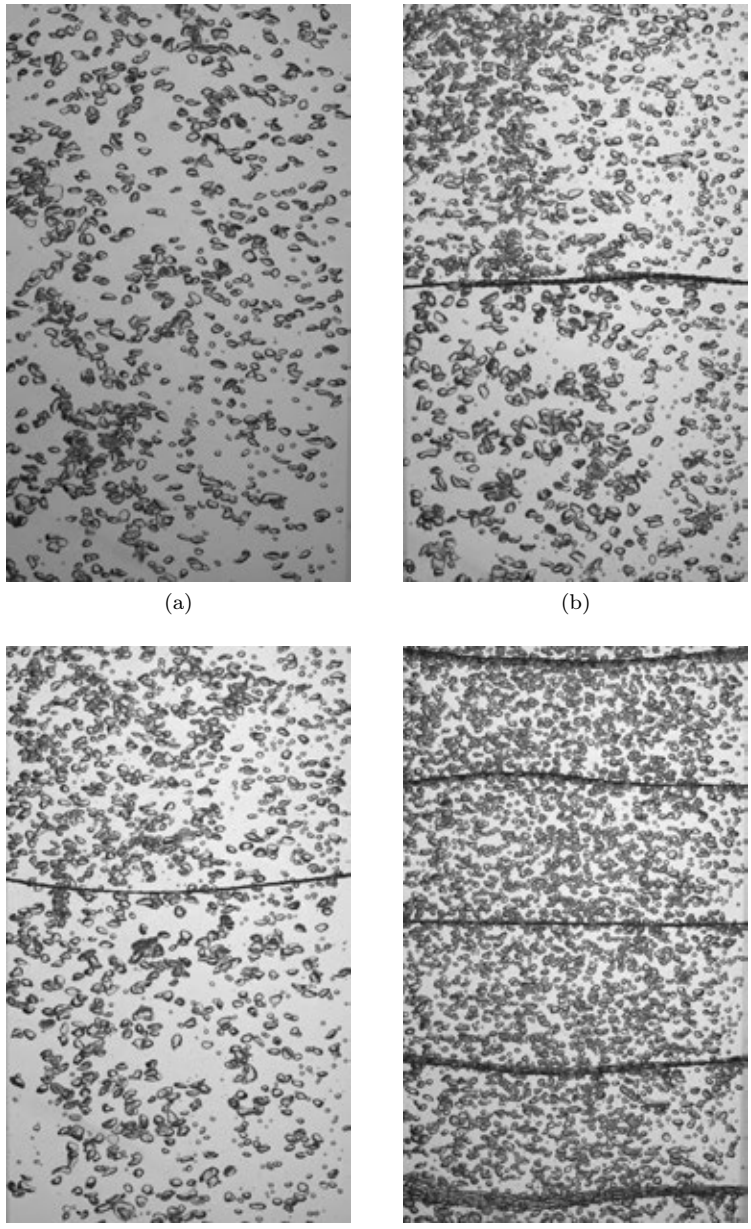

(a) (b)

(c) (d)

Figure 4.2: Images of bubbly flow in the MSBC at superficial gas velocity 10 mm/s: (a) No mesh (b) Mesh opening 2.7 mm (c) Mesh opening 3.7 mm (d) Mesh opening 3.7 mm with 10 stages.

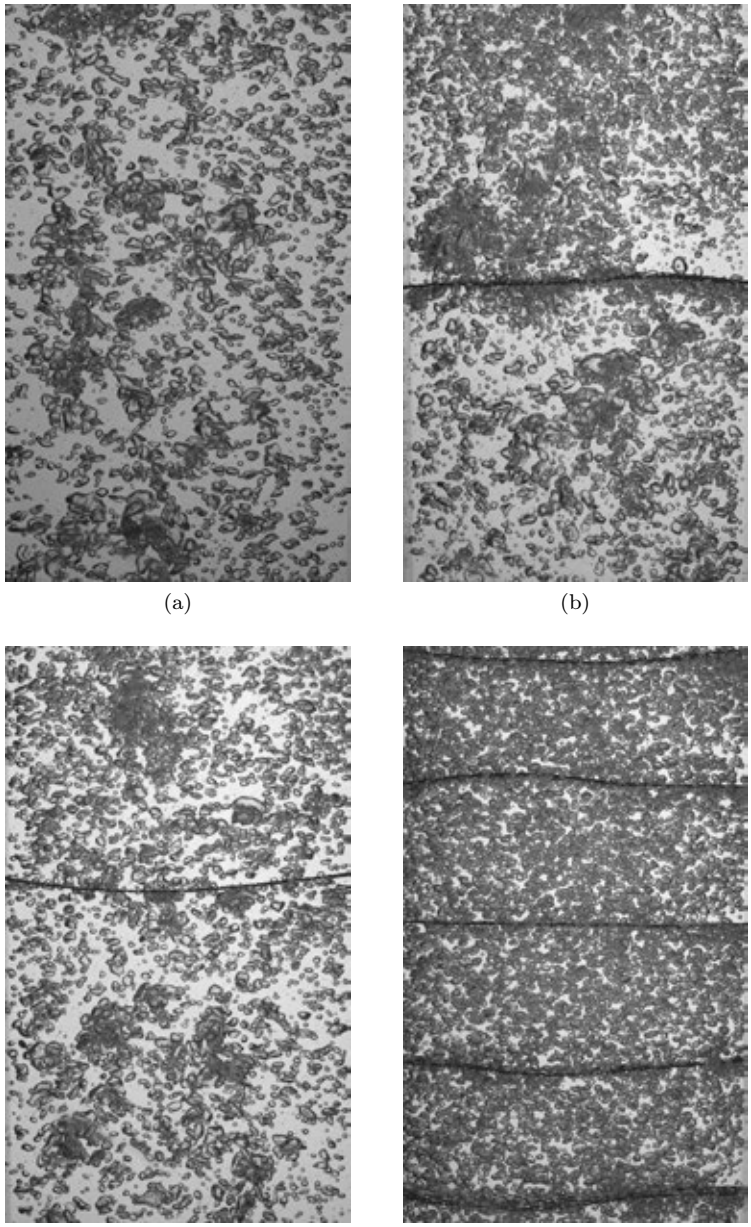

(a) (b)

(c) (d)

Figure 4.3: Images of bubbly flow in the MSBC at superficial gas velocity 20 mm/s: (a) No mesh (b) Mesh opening 2.7 mm (c) Mesh opening 3.7 mm (d) Mesh opening 3.7 mm with 10 stages.

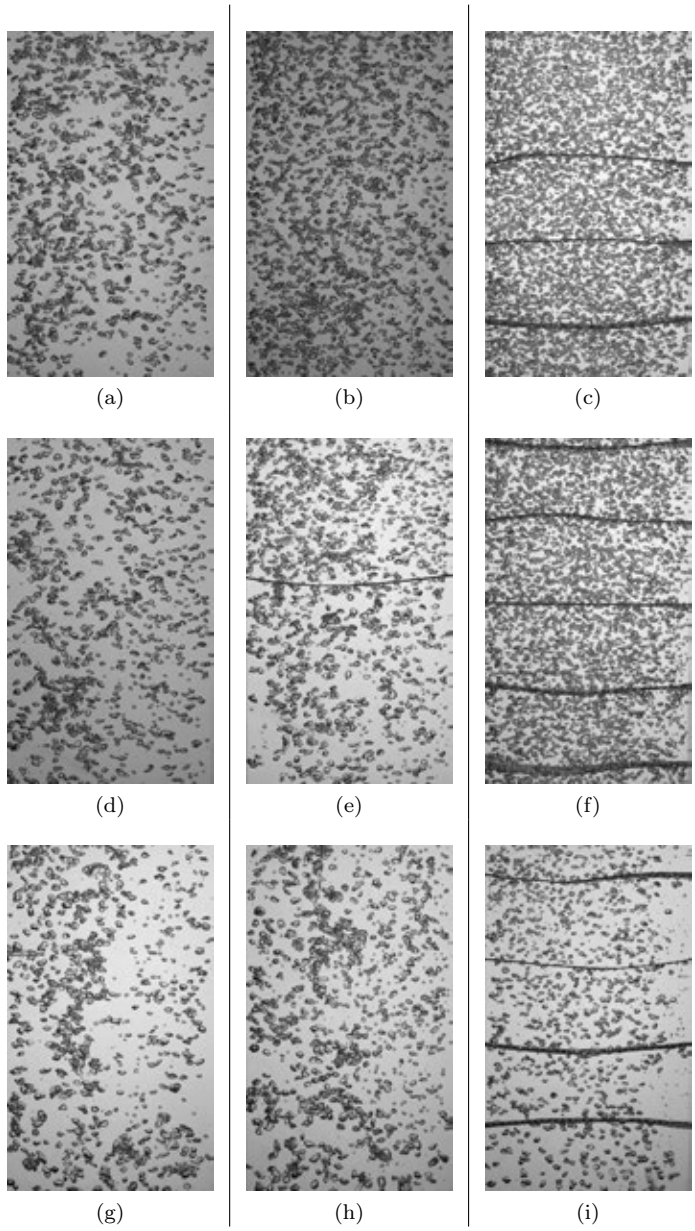

Figure 4.4: Images of bubbly flow in the MSBC at superficial gas velocity 10 mm/s for section top, middle and bottom respectively. Images at left are for no mesh, mesh opening 3.7 mm is at center and mesh opening 3.7 mm with 10 stages are shown on the right.

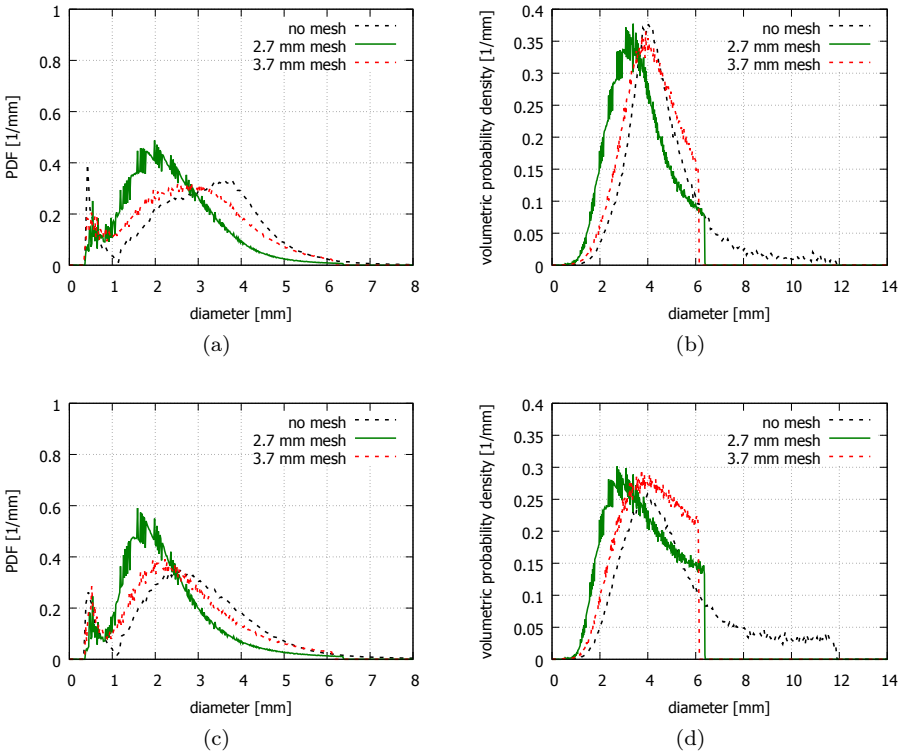

Figure 4.5: Bubble size distribution for the top section of the column for different mesh configurations (no mesh, 2.7 mm mesh opening and 3.7 mm mesh opening). a) probability density function at a superficial gas velocity of 10 mm/s. b) volumetric probability density at a superficial gas velocity of 10 mm/s. c) probability density function at a superficial gas velocity of 15 mm/s. d) volumetric probability density at a superficial gas velocity of 15 mm/s.

mesh is appropriate as large bubbles are detected correctly. The algorithm performs well until superficial gas velocities of 15 mm/s for the configuration with a wire mesh.

Fig. 4.6 shows that the Sauter mean diameter for the wire mesh is lower than the case without mesh. This result indicates that both meshes have a good performance in terms of bubble cutting. The constant bubble size both above and below the wire mesh can be explained by the down-flow of small bubbles through the open area of the wire mesh. The slight discontinuity at the top region of 3.7 mm mesh can be explained due to differences between sections of images.

The gas holdup was measured by the height expansion technique. The results of pure dodecane agree with the observation of Öztürk et al. (1987), that organic liquids always have a higher gas holdup when compared to water. Fig 4.7 shows the

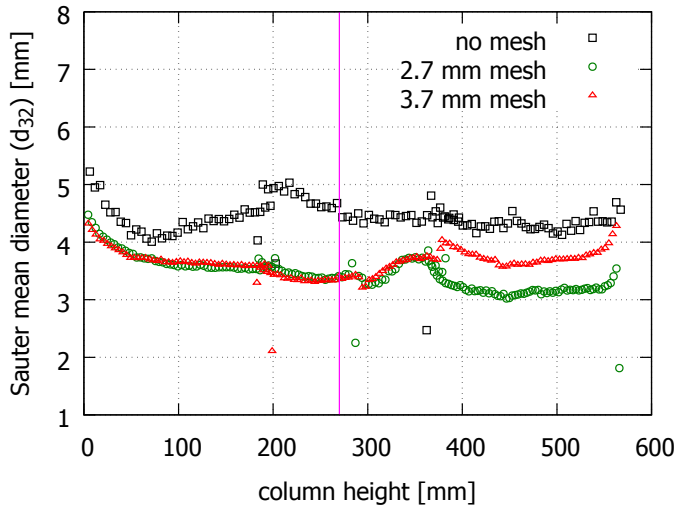

Figure 4.6: Sauter mean diameter vs column height for different mesh configurations (no mesh, 2.7 mm mesh opening and 3.7 mm mesh opening) at a superficial gas velocity of 15 mm/s. The pink solid line indicates the location of the wire mesh in the column at a height of 270 mm.

gas holdup for different superficial gas velocities and different mesh configuration. The gas holdup increases with the superficial gas velocity for all cases. The holdup for the configuration with wire mesh is substantially higher than the benchmark case without mesh for all superficial gas velocities. The mesh with 2.7 mm opening performs slightly better than the mesh with 3.7 mm opening.

Effect of wire mesh staging

The number of wire mesh stages can have a significant impact on the flow structure in the MSBC reactor. This section compares configurations with no mesh, a single mesh stage and ten mesh stages. It should be pointed out that all meshes have a constant mesh opening of 3.7 mm.

Fig. 4.8 shows that the probability of small bubbles with a size ranging between 2-3 mm is higher for the configuration with ten meshes when compared to other cases. The peak which occurs for bubbles less than 1 mm does not appear in the multiple mesh case. This might be due to the occurrence of a homogeneous regime at the top section of the column for multiple mesh case. The bubble size distribution for superficial gas velocities above 15 mm/s were not analyzed due to limitations of the digital image analysis technique.

The Sauter mean diameter as seen in Fig. 4.9 agrees with the observations made for the bubble size distribution. The overall cutting for the superficial gas velocity of 15 mm/s is similar to that of the single mesh case. The configuration with ten

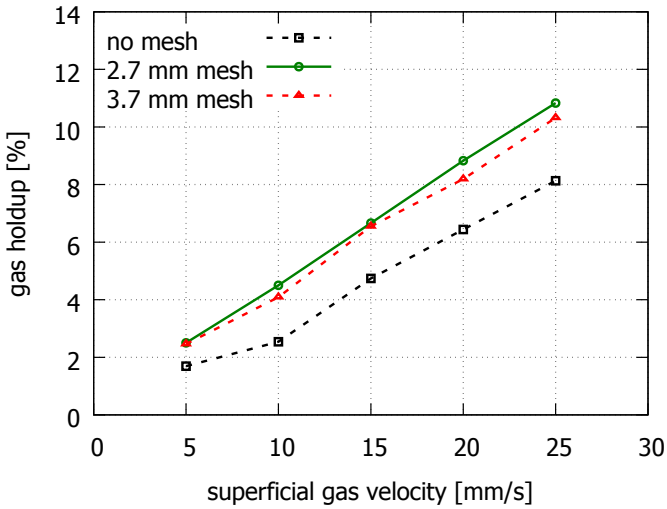

Figure 4.7: Gas holdup obtained by height expansion versus superficial gas velocity for different wire mesh openings.

mesh stages is slightly better when compared visually, but these differences are not captured by the digital image analysis technique.

Fig. 4.10 shows that the gas holdup for the configuration with ten mesh stages is slightly more than the cases with a single mesh and no mesh. It can be seen that the difference in gas holdup increases with increasing superficial gas velocities. The higher gas holdup is attributed to small bubbles which can be formed by bubble cutting or bubble breakup.

4.4 Conclusions

Experiments are performed in the micro-structured bubble column for the dodecane-nitrogen system. Pure dodecane has froth formation at the top due to the formation of small bubbles, typically observed in a non-coalescing system. Bubble cutting takes place even at low superficial gas velocity and small mesh openings (2.7 mm) due to the low surface tension of the dodecane-nitrogen system. This is markedly different compared to the air-water system, where a relatively larger superficial gas velocity and mesh opening (3.7 mm) is required for appreciable bubble cutting. It is recommended to use industrial organic media whenever possible in future pilot plant studies, to assess the effect of coalescing/non-coalescing systems with different physico-chemical properties on the hydrodynamics. The experimental data obtained in the dodecane-nitrogen system can be used for validation of Euler-Lagrange simulation for laboratory scale bubble columns.

Increasing the number of mesh stages in the micro-structured bubble column changes the overall hydrodynamics of the system from heterogeneous to a homo-

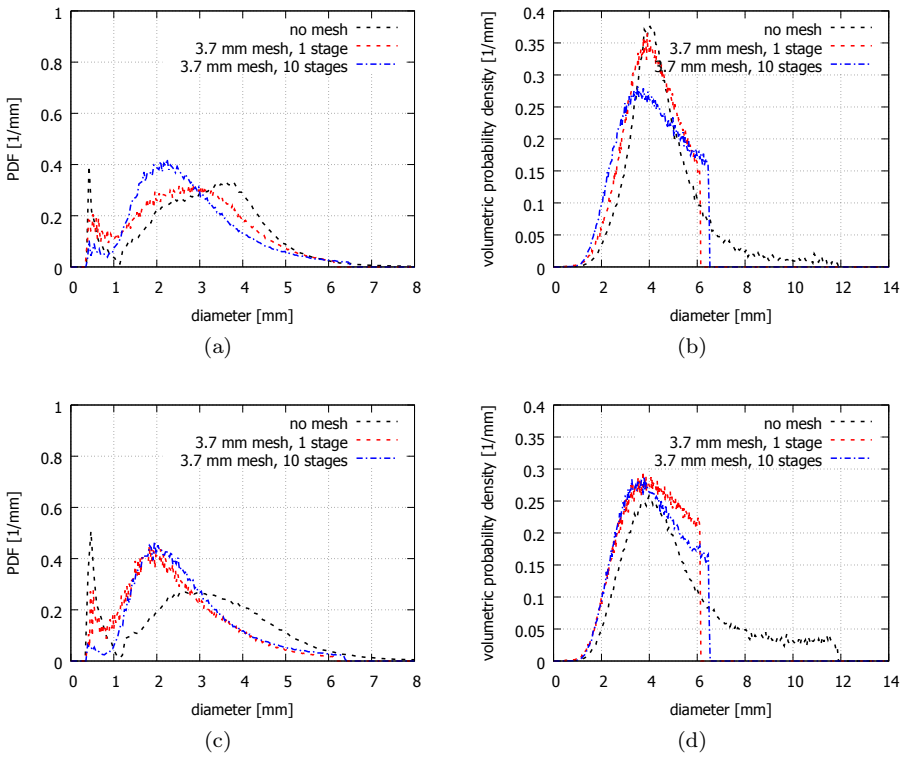

Figure 4.8: Bubble size distribution for the top section of the column for different numbers of wire mesh stages (no mesh, single stage with a 3.7 mm mesh opening, and ten stages with a 3.7 mm mesh opening). a) probability density function at a superficial gas velocity of 10 mm/s. b) volumetric probability density at a superficial gas velocity of 10 mm/s. c) probability density function at a superficial gas velocity of 15 mm/s. d) volumetric probability density at a superficial gas velocity of 15 mm/s.

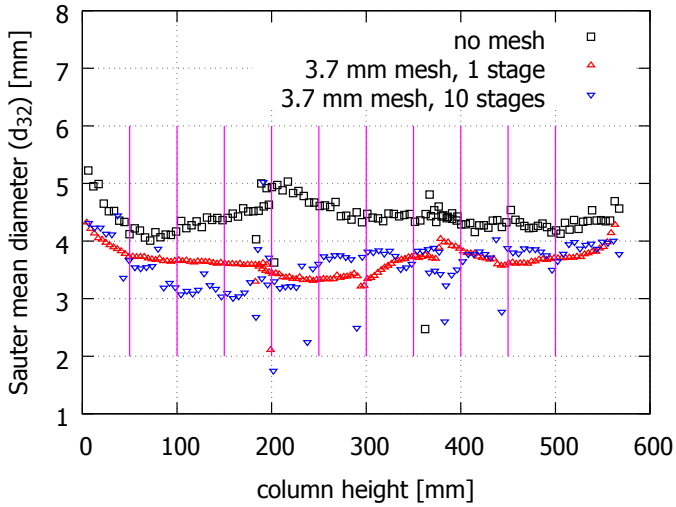

Figure 4.9: Sauter mean diameter vs column height for different number of wire mesh stages (no mesh, 3.7 mm mesh opening with single stage and 3.7 mm mesh opening with ten stages) at superficial gas velocity of 15 mm/s. Pink solid lines indicate location of wire mesh stages, starting at height of 50 mm with 50 mm spacing between consecutive meshes.

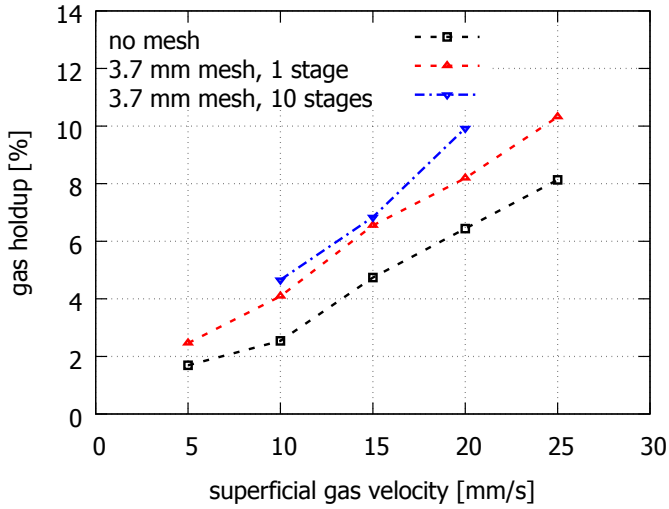

Figure 4.10: Gas holdup obtained by height expansion versus superficial gas velocity for different number of wire mesh stages.

geneous regime. The use of multiple meshes also enhances bubble cutting or breakup which is evident by an increase in the gas holdup.

Nomenclature

ε	holdup	$[-]$
A	area	$[m^2]$
D	depth	$[m]$
d	diameter	$[m]$
d_{32}	Sauter mean diameter	$[m]$
H	height	$[m]$
h	height of gas-liquid dispersion	$[m]$
W	width	$[m]$
PDF	probability density function	$[1/mm]$
0	initial	
eq	equivalent	
f	final	
g	gas	
H	height expansion	
k	index	
DIA	digital image analysis	
MSBC	micro-structured bubble column	

CHAPTER 5

Effect of bubble cutting on chemisorption of CO_2 into $NaOH$

A novel micro-structured bubble column reactor (MSBC) is studied by a combined experimental and simulation approach, for the chemisorption of CO_2 into $NaOH$. To understand the reactor behavior different reactor configurations are tested for chemisorption by varying the internals (single wire mesh, staged wire meshes, Sulzer packing). Bubble size distribution, pH and holdup data are obtained from chemisorption experiments using an advanced digital image analysis technique. The effect of superficial gas velocities ranging from 5 to 25 mm/s and varying number of wire mesh stages (1, 6 and 10) is deduced from the experiments. The experimental results are used for the validation of the detailed VoF-DBM simulations.

5.1 Introduction

Bubble columns are often used in the chemical industry for gas-liquid contacting processes. For instance, in gas-treating processes to remove H_2S and/or CO_2. The limiting step in the chemisorption process is usually the mass transfer from the gas phase to the liquid phase. The mass transfer rate is a function of the interfacial area, the intrinsic mass transfer coefficient and the driving force. The mass transfer rate can be increased by increasing the interfacial area and/or the interfacial mass transfer coefficient. This can achieved by means of adding internals such as sieve plates, porous plates, and static mixers (SMV) (Baird, 1992; Deen et al., 2000). The addition of internals is known to reduce the back-mixing in the bubble column reactor, which can be advantageous in some situations. In our previous work, we have proposed a novel micro-structured bubble column(MSBC) reactor with wire-meshes

as internals (Sujatha et al., 2015; Jain et al., 2013, 2014). Jain et al. (2013, 2014) have developed a combined VoF-DBM model to simulate and study the effect of wire mesh in the MSBC reactor. Sujatha et al. (2015) have done experiments in laboratory scale MSBC reactor to study the effect of wire mesh configuration and superficial gas velocity. Three hydrodynamic regimes were identified for bubbly flow in a MSBC with wire mesh in an air-water system for superficial gas velocities in the range of 5 to 50 mm/s.

The scope of the current paper is to extend the work for the chemisorption of CO_2 into a $NaOH$ solution, by a combined experimental and simulation approach. Bubble size distribution, pH and holdup data are obtained from chemisorption experiments. These data are compared with simulation results obtained from a detailed VoF-DBM model developed by Jain et al. (2014). The effect of the mesh configuration is investigated by varying the mesh opening and the distance between mesh stages for superficial gas velocities ranging from 5 to 25 mm/s.

This paper is organized as follows. The description of the experimental setup and methods used for obtaining the results (i.e. digital image analysis technique and VoF-DBM method) are discussed elaborately. The results and discussion section consists of visual analysis, experimental results and comparison of experiments with simulation.

5.2 Material and methods

A flat pseudo-2D bubble column reactor of dimensions (width W=0.2 m, depth D=0.03 m, height H=1.3 m) is chosen for experiments. The reactor walls are constructed of transparent glass to enable visual observation by the eye or using a camera. The gas is fed into the column via a group of fifteen gas needles centrally arranged in the distributor plate. The needles have a length (L) = 50 mm, inner diameter (I.D.) = 1 mm and outer diameter (O.D.) = 1.5875 mm. The needles extend 10 mm above the bottom plate and are spaced with a center-to-center distance of 9 mm. An array of five needles is classified as a group, and each group of needles is connected to a mass flow controller. Subsequently, three mass flow controllers are used to control the gas flow rates in the column. Micro-structuring in the reactor is realized by means of thin wires of various dimensions arranged in a mesh structure or by using a Sulzer packing (SMV). The wire mesh or Sulzer packing can be mounted onto the column by using a modular insert, designed for this purpose. The modular insert design allows full flexibility to attach one or more wire meshes at different locations of the insert. The dimensions of the column including the insert are as follows: width=0.14 m, depth=0.03 m, height=1.3 m. The location of the wire mesh was fixed for the experiments at a distance of 0.26 m from the bottom distributor plate and the Sulzer packing is fixed at 0.24 to 0.26 m. An overview of the several mesh configurations can be seen in Table 5.1.

The experimental procedure followed for the $CO_2 - NaOH$ system is as follows. The column is filled with a well stirred solution of sodium hydroxide prepared with pH = 12.5. Inert gas nitrogen is used to aerate the column before the starting time of the experiment at desired gas flow rate. The camera is focused to a particular section

Mesh #	wire diameter (mm)	mesh opening (mm)	open area (%)
4	0.80	5.6	76
6	0.55	3.7	76
6	0.90	3.3	62
8	0.50	2.7	71
10	0.31	2.2	75
12	0.31	1.8	73
18	0.22	1.2	71

Table 5.1: Overview of different wire meshes used for experiments.

of the column to capture sharp images. The pH meter is immersed in the $NaOH$ solution, at the top of the column to measure and record local pH for the duration of reaction. The flow is switched to CO_2 and the timer is started. Initial liquid height is noted down at time t = 0 and the high-speed recording of images is started. As the reaction proceeds the change in height of gas-liquid dispersion is noted down. Once there is no relevant change in pH with time the CO_2 flow is switched back to nitrogen flow. The change in the gas holdup is observed via the change in height of the gas-liquid dispersion with time.

5.2.1 Digital image analysis

The DIA technique (Lau et al., 2013a,b) was developed to determine the mean diameter d_{eq}, bubble size distributions and gas holdup in pseudo-2D bubble column reactor. Sujatha et al. (2015) improved the DIA technique to detect very small bubbles. The image analysis algorithm has four main operations: a) Image filtering b) separation of bubbles into solitary and overlapping bubbles c) segmentation of overlapping bubbles using watershedding technique d) combination of solitary and overlapping bubble images. Image filtering involves operations to obtain a desired image involving removal of the inhomogeneous illumination using an Otsu filter (Otsu, 1975). The Otsu filter determines the threshold for separating the bubbles from the background, by thresholding individual blocks of an image. The edges of the bubbles are detected by a Canny edge detection algorithm. The bubbles are separated into solitary bubbles and overlapping bubbles using roundness as a separation criteria. The images with solitary bubbles are segmented by marking the bubbles, whereas the overlapping bubbles are segmented using the watershed algorithm proposed by Meyer (1994a). An example image after bubble detection is shown in Fig. 5.1.

A CMOS camera with resolution of 2016 $pixel$ × 2016 $pixel$ is used to capture the images of two-phase bubbly flow by using back-lighting to obtain maximum contrast between the bubbles and the background. The MSBC is divided into three different sections for the purpose of imaging and 4000 images are made at 50 Hz for each section . Images from each section have a size of 0.21 m×0.14 m and a small overlap

of 0.04 m. The resolution of the image is 0.11 mm/pixel.

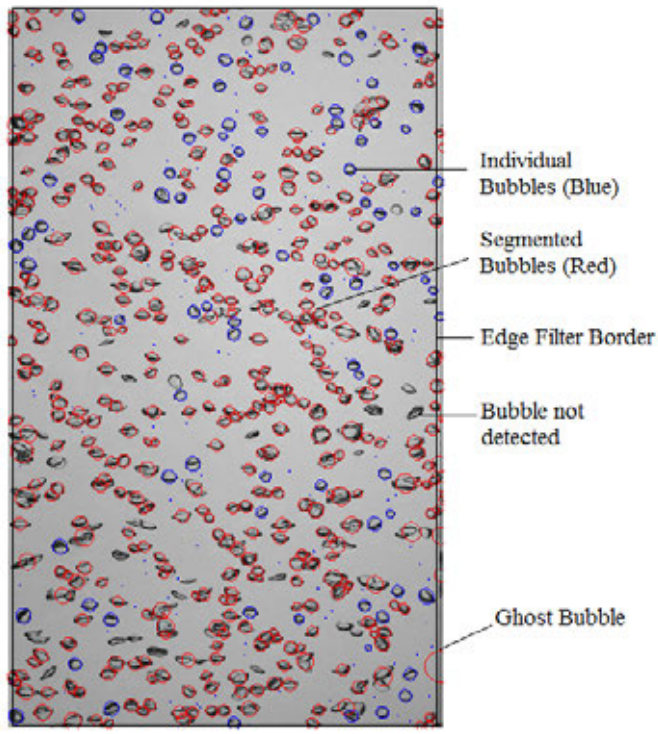

Figure 5.1: Image after detection. Individual bubbles are indicated by blue circles and segmented bubbles are indicated by red circles.

The Sauter mean diameter of an image is calculated from the equivalent diameter using the following equation:

$$d_{32} = \frac{\sum_{k=0}^{n} d_{eq,k}^3}{\sum_{k=0}^{n} d_{eq,k}^2} \tag{5.1}$$

The probability density function (PDF) for a particular bubble diameter class is the ratio of number of bubbles in a particular diameter class(Δd_{eq}) to the sum of number of bubbles in all size classes. Therefore, the PDF of a particular size class (Δd_{eq}) is calculated from the number of bubbles and average bubble diameter as follows:

$$PDF_{\Delta d_{eq}} = \frac{N_{\Delta d_{eq}}}{\left(\sum_{\Delta d_{eq,min}}^{\Delta d_{eq,max}} N_{\Delta d_{eq,k}} \right) \Delta d_{eq}} \tag{5.2}$$

The gas holdup is determined for the air-water system by liquid expansion measurements. It is calculated by the following formula:

$$\varepsilon_{(g,H)} = \frac{h_f - h_0}{h_f} \tag{5.3}$$

where h_f is the height of the gas-liquid dispersion and h_0 is the initial height of the liquid.

5.3 Volume of Fluid - Discrete Bubble model

A Volume of Fluid (VoF) - Discrete Bubble Model (DBM) is used to model the hydrodynamics of the system. This model is an Euler-Lagrangian model. The bubbles are tracked and the liquid phase is treated as a continuum. A force balance is solved for every bubble using Newton's second law of motion. For an incompressible bubble the equations are given by:

$$\rho_b \frac{d(V_b)}{dt} = (\dot{m}_{l \to b} - \dot{m}_{b \to l}) \tag{5.4}$$

$$\rho_b V_b \frac{d(v)}{dt} = \Sigma F - (\rho_b \frac{d(V_b)}{dt}) v \tag{5.5}$$

$$\Sigma F = F_G + F_p + F_D + F_L + F_{VM} + F_W \tag{5.6}$$

The forces considered on the bubble are due to gravity (F_G), local pressure gradients (F_p), liquid drag (F_D), lift forces(F_L), virtual mass forces(F_{VM}) and wall forces (F_W). Closures for these forces are given in the work of Jain et al. (2013).

Fluid phase hydrodynamics

The whole system is divided into four phases, each with its own volume fraction (ε): a) liquid (ε_l), b) bubble (ε_b), c) gas (ε_g, continuous layer above the liquid height), and d) wire-mesh (ε_w solid).

where the sum of all volume fractions equals unity:

$$\varepsilon_l + \varepsilon_g + \varepsilon_b + \varepsilon_w = 1 \tag{5.7}$$

The liquid phase hydrodynamics is described by the volume averaged Navier-Stokes equations, which consists of continuity and momentum equations:

$$\frac{\partial(\rho_f \varepsilon_f)}{\partial t} + \nabla \cdot (\varepsilon_f \rho_f u) = (\dot{M}_{b\to l} - \dot{M}_{l\to b}) \tag{5.8}$$

$$\begin{aligned}\frac{\partial}{\partial t}(\rho_f \varepsilon_f u) + (\nabla \cdot \varepsilon_f \rho_f uu) = \\ -\varepsilon_f \nabla p + \rho_f \varepsilon_f g - \mathbf{f}_\sigma - \mathbf{f_{l\to b}} + \mathbf{f_{w\to l}} \\ +\{\nabla \cdot \varepsilon_f \mu_{eff}[((\nabla u) + (\nabla u)^T) \\ -\frac{2}{3} I(\nabla \cdot u)]\}\end{aligned} \tag{5.9}$$

where

$$\varepsilon_f = \varepsilon_l + \varepsilon_g \tag{5.10}$$

$$\mu_{eff} = \mu_{L,l} + \mu_{T,l} \tag{5.11}$$

$\dot{M}$ represents the rate of mass transfer. $\mathbf{f}_\sigma$ represents the local volumetric surface tension force acting on the free surface at the top of the column and u represents the average fluid velocity. The interface can be seen in Fig. 5.2.

A Volume of Fluid (VoF) method is used to simulate the free surface and the gas above the liquid level in the column. van Sint Annaland et al. (2005) have used this method to successfully show the coalescence of two gas bubbles in a fluid. The grid size used here is larger compared to direct numerical simulations but this is acceptable as the surface only has a small curvature. The local average ρ and μ are calculated using a color function F which is governed by:

$$\frac{DF}{Dt} = \frac{\partial F}{\partial t} + (u \cdot \nabla F) = 0 \tag{5.12}$$

$$F = \frac{\varepsilon_l}{\varepsilon_l + \varepsilon_g} = \frac{\varepsilon_l}{\varepsilon_f} \tag{5.13}$$

It can be easily noted that the grid cells lying completely below the free surface have $\varepsilon_g = 0$ and similarly the grid cells lying completely above the free surface have $\varepsilon_l = 0$. The properties like density and viscosity for the other grid cells that cover the free surface are calculated as follows.

$$\rho_f = F\rho_l + (1 - F)\rho_g \tag{5.14}$$

$$\frac{\rho_f}{\mu_f} = F\frac{\rho_l}{\mu_l} + (1 - F)\frac{\rho_g}{\mu_g} \tag{5.15}$$

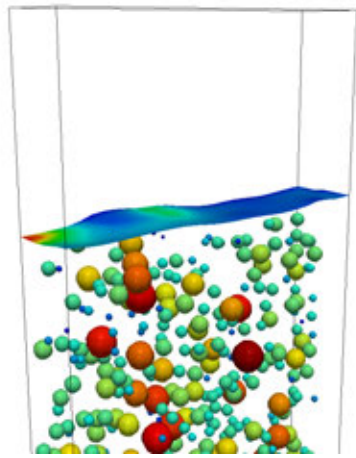

Figure 5.2: Example snapshot of VoF-DBM simulation showing bubbles and free surface.

The boundary conditions are applied using a flag matrix concept. Fig. 5.3 shows the different values of the flags of the pseudo 2-D column. The cells are assigned different flag values indicating different types of boundary conditions that are listed in Table 5.2.

Flag	Boundary conditions
1	Interior cell, none specified
2	Prescribed pressure cell, free slip
3	Impermeable wall, no slip, Neumann conditions for species
4	Corner cell, none specified

Table 5.2: Flag meaning for cell boundary conditions.

The turbulence in the liquid phase due to bubbly flow is taken into account by using a sub-grid scale model proposed by Vreman (2004) for the eddy viscosity.

Bubble coalescence is accounted based on the model proposed by Sommerfeld et al. (2003). The collision time is determined by the relation reported by Allen and Tildesley (1989). Film drainage time for coalescence to occur is calculated based on the model of Prince and Blanch (1990). When the contact time is less than the film drainage time coalescence does not occur and the bubbles simply bounce. Otherwise, they coalesce. A detailed description of the model can be found in Darmana et al. (2005). Bubble breakup occurs if the inertial force exceeds the surface tension forces, the ratio of which can be represented as Weber number. The critical Weber number for breakup to occur is 12 as determined by Jain et al. (2014). Based on this, a binary

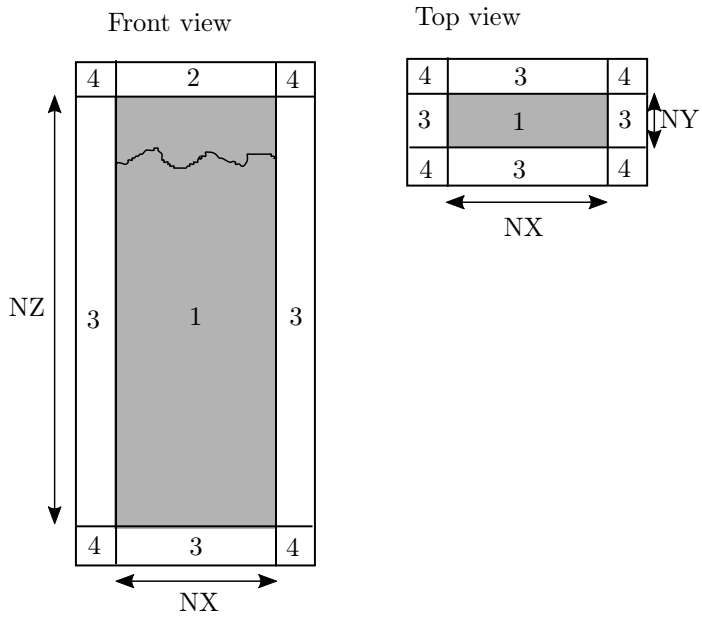

Figure 5.3: Boundary conditions for the VoF-DBM; Front view at j=NY/2 and top view for cells k=2 to k=NZ-1.

breakup model is modeled in which the bigger bubble is placed at the position of the parent bubble and the smaller bubble is placed randomly around the centroid of the bigger bubble.

Wire-mesh and cutting

The wire mesh is present in the middle of the column to cut the bubbles. A simple geometric cutting model proposed by Jain et al. (2013) is incorporated to account for cutting the bubbles when they pass the wire mesh. A stochastic factor called cutting efficiency is introduced into the model to characterize the fraction of bubbles that is actually cut by the wire mesh. A cutting efficiency 0 means there is no cutting and a value of 1 means all bubbles are eligible to get cut. The drag that the wire-mesh exerts on the liquid is taken into account in Equation 5.9 (Jain et al., 2013).

Chemical species equations

The species are accounted by Y_j which is the mass fraction of species j. Species balance for $N_s - 1$ components are solved simultaneously with appropriate boundary conditions, where N_s is number of components present in the system. The fraction

of the last component can be derived from the overall mass balance.

$$\frac{\partial}{\partial t}(F\varepsilon_f \rho_f Y_j) + \nabla \cdot (F\varepsilon_f (\rho_l u Y_j - \Gamma_{j,eff} \nabla Y_j)) = \left(\dot{M}^j{}_{b\to l} - \dot{M}^j_{l\to b}\right) + F\varepsilon_f S_{R,j} \tag{5.16}$$

$$\sum_{j=1}^{N_S} Y_j = 1 \tag{5.17}$$

S_{Rj} is the source term accounting for the production or consumption of species j due to chemical reaction.

The mass transfer is given by:

$$\dot{m}_b^j = E k_l^j A_b \rho_l (Y_l^{j*} - Y_l^j) \tag{5.18}$$

Where the mass transfer coefficient k_l is calculated through a Sherwood correlation. Several mass transfer correlations are available in literature for bubbly flows. Brauer (1981) gives a correlation for ellipsoidal bubbles accounting for the shape of the bubble due to the deformations caused by liquid flow around bubbles:

$$Sh = 2 + 0.015 \times Re_B^{0.89} Sc^{0.7} \tag{5.19}$$

The correlation for the enhancement factor (E) provided by Westerterp et al. (1987) is used as proposed by Darmana et al. (2005).

5.4 Results

5.4.1 Visual observation

Images are obtained using a high-speed camera operated at 50 Hz, for a velocity of 5-30 mm/s for different wire meshes and the Sulzer packing(SMV). Fig. 5.4 shows the images of bubbly flow in a MSBC for different configurations, such as no internals, with mesh (single 3.7 mm mesh opening, 3.7 mm mesh in six stages and 3.7 mm mesh in 10 stages) and Sulzer packing. The images are shown for the mid section at a superficial gas velocity of 15 mm/s. In Fig. 5.4, there are small bubbles present above and below the mesh or Sulzer packing. The presence of small bubbles also increases with increasing superficial gas velocities as a consequence of bubble break-up. In Fig. 5.4a, for the case without internals the bubbles are homogeneously distributed in the column with some big bubbles. When comparing the different images in Fig. 5.4, it is evident that the bubble cutting occurs in the presence of internals.

5.4.2 Effect of internals

It is important to note that for Fig. 5.5 and Fig. 5.6, time-averaging is done for a duration of 4 seconds (i.e. between 10 to 14 seconds after the CO_2 flow starts in the column) for all superficial gas velocities and mesh openings. It is reasonable to assume that the hydrodynamics of the bubbly flow does not change within such a short time

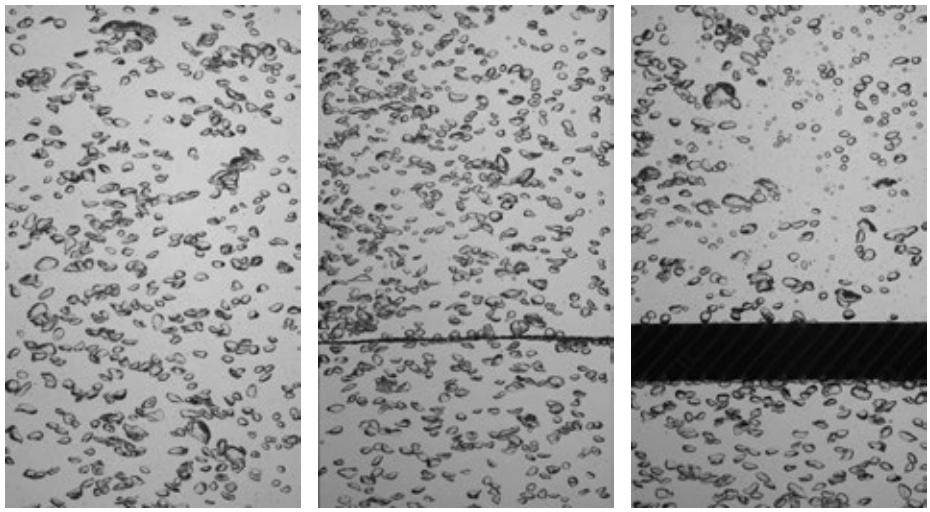

(a) (b) (c)

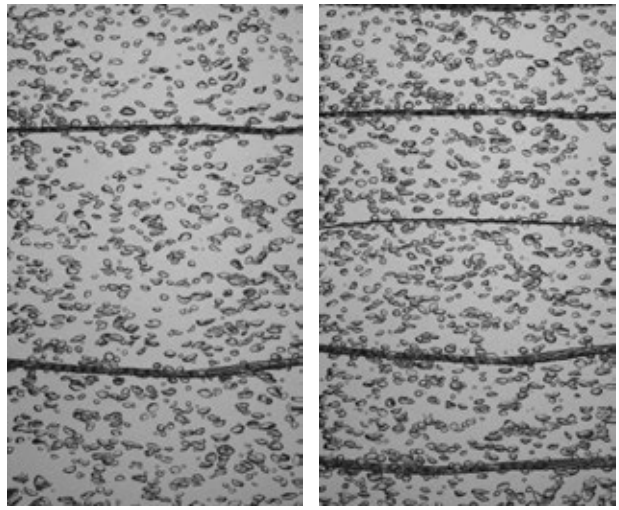

(d) (e)

Figure 5.4: Images of bubbly flow in the MSBC at a superficial gas velocity of 15 mm/s: (a) No mesh (b) Mesh opening 3.7 mm (c) Sulzer packing (d) 6 stage (e) 10 stages .

span, as there is a very small change in pH. This assumption enables comparison of the cutting behavior of different internals at a particular superficial gas velocity.

The effect of mesh configuration is studied for three different wire mesh openings (i.e. for 2.7 mm, 3.3 mm and 3.7 mm) for comparison with the no mesh case and Sulzer packing. The time-averaged Sauter mean diameter and volumetric probability density function are plotted in Fig. 5.5 and Fig. 5.6 respectively. The Sauter mean diameter is ratio of volume to surface area of the detected bubbles from the three different image sections. It is used to evaluate the mass transfer performance of the wire meshes/packing used in the MSBC.

Fig. 5.5 shows the time averaged Sauter mean diameter plotted vs height of the MSBC, for different configurations of internals. The meshes/packings perform much better than the no mesh case, as there is approximately 1 mm drop in bubble diameter after the location of mesh/packing (i.e. 0.26 m).

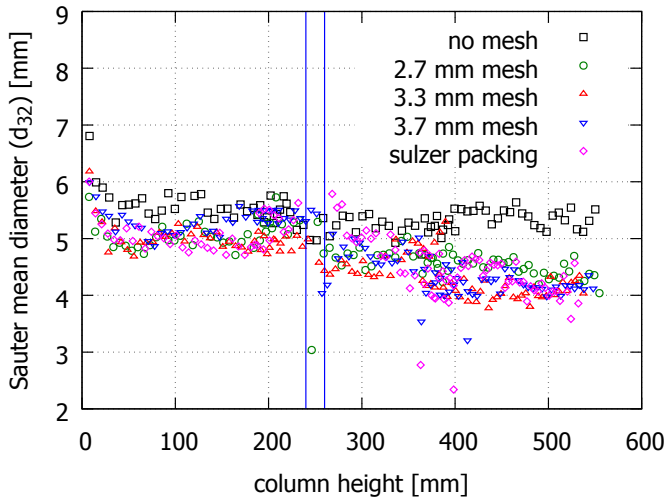

Figure 5.5: Sauter mean bubble diameter vs height for varying mesh types at superficial gas velocity 25 mm/s. The positions of the mesh [0.26 m] and the packing [0.24 to 0.26 m] are indicated by the solid lines.

The bubble cutting is also evident in Fig. 5.6, which shows the time-averaged volumetric probability density vs diameter for different column configurations. Sulzer packing performs the best in terms of resizing the bubbles. Amongst the wire meshes the mesh with 3.7 mm opening performs the best.

This can also be observed in the plot of pH vs time for different cases as shown in Fig. 5.7, as the pH curve for the 3.7 mm mesh opening and Sulzer packing drops fast to reach pH 7 in 70 seconds. The MSBC with no mesh configuration takes almost 90 seconds for reaching pH 7 at same velocity. Hence the pH decay curves show that MSBC with internals perform much better than the configuration with no internals for a reaction limited by gas-liquid mass transfer. It should be observed that although

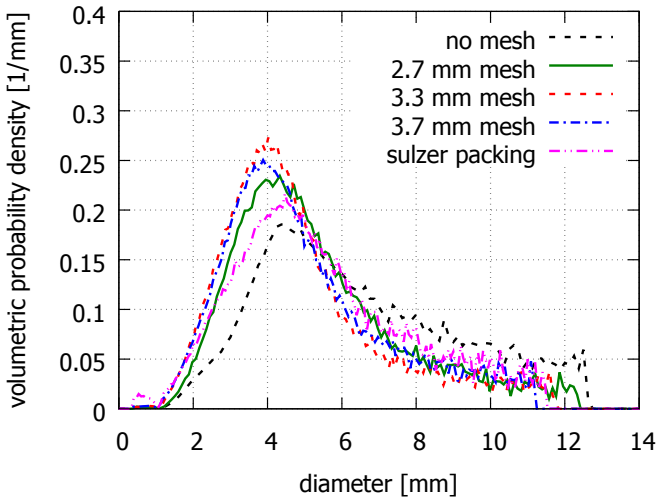

Figure 5.6: Volumetric probability density function vs diameter in varying mesh types at superficial gas velocity 25 mm/s in the top section [0.42 to 0.60 m].

Sulzer packing has better cutting than the 3.7 mm mesh it has a similar performance in terms of mass transfer.

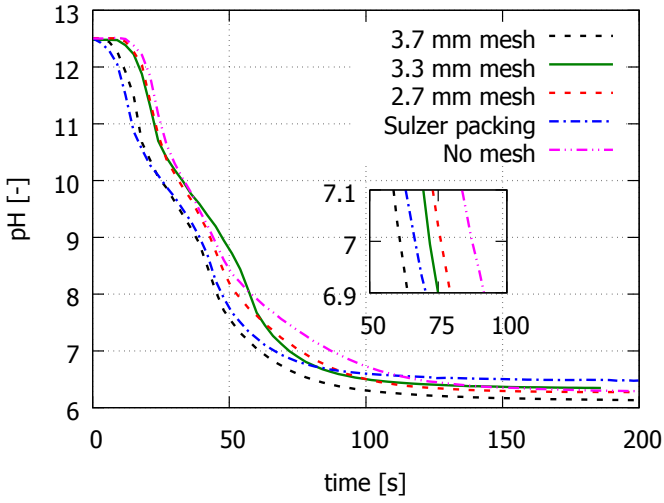

Figure 5.7: pH vs time curve for different mesh types at superficial gas velocity 25 mm/s.

5.4.3 Effect of superficial gas velocity

The time averaging of bubble size distributions are done for a duration of 4 seconds (i.e. between 10 to 14 seconds after the CO_2 flow starts in the column) for all superficial gas velocities and mesh openings. It is reasonable to assume that the hydrodynamics of the bubbly flow does not change within such a short time span, as there is a very small change in pH (see Fig. 5.8).

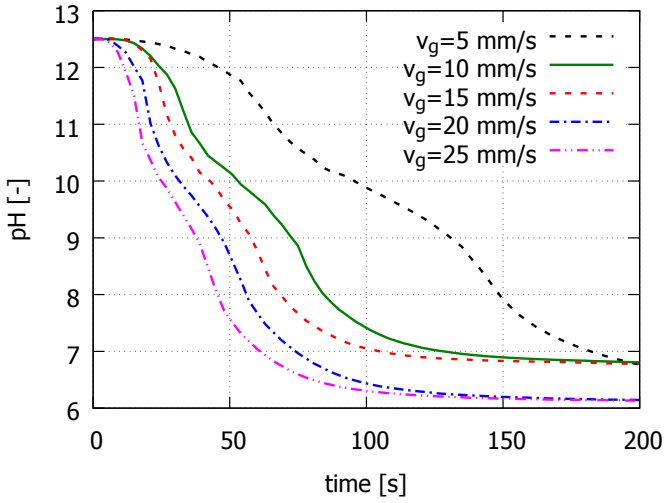

Figure 5.8: pH vs time curve with varying superficial gas velocities [5 to 25 mm/s] for mesh opening 3.7 mm.

The effect of superficial gas velocity on the time-averaged bubble size distribution can be seen in Fig. 5.9. At 5 mm/s, two peaks can be observed. The left peak corresponds to very small bubbles (less than 1 mm in diameter) and the larger peak corresponds to the average bubble size (3 mm diameter). The bimodal nature of distribution is due to the formation of very small bubbles resulting from breakup at the free surface, which are subsequently dragged down into the column by liquid circulation. It can be seen that as the velocity is increased, the distribution becomes flatter due to bubble coalescence and breakup until 15 mm/s. For higher velocities, the distribution of the second peak tends to shift towards smaller bubbles as a result of enhanced bubble cutting and breakup. This trend is general for all cases with and without internals. However with the presence of internals the bubble cutting has an added impact on the bubble size distribution.

5.4.4 Effect of reactor staging

It is observed that in the single mesh configuration, large bubbles are cut by the mesh but they re-coalesce above the mesh. Stacking multiple meshes enables successive cutting of those large bubbles. Moreover, as the number of meshes increases, the liquid back-mixing reduces significantly. The spacing between successive meshes controls the

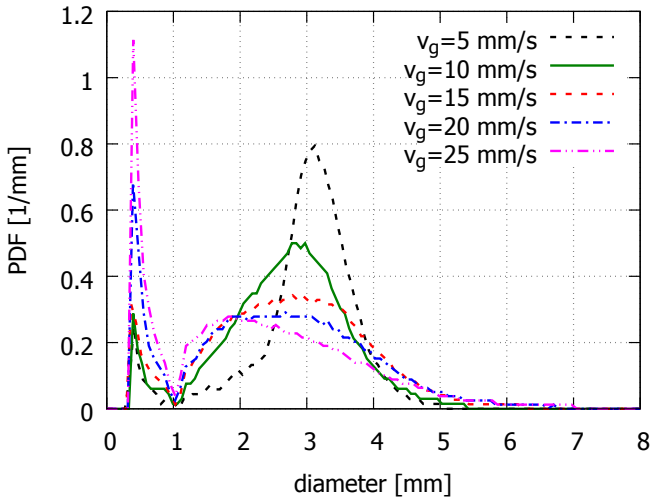

Figure 5.9: Bubble size distribution with varying superficial gas velocities [5 to 25 mm/s] for mesh opening 3.7 mm in the top section [0.42 to 0.60 m].

circulation patterns and the reactor displays more of a plug flow behavior as the mesh spacing is reduced.

Two multiple mesh configurations with six and ten mesh stages are tested by chemisorption experiments for the mesh with mesh openings of 3.7 mm. The reactor with six meshes has a better performance as seen in Fig. 5.10, from the pH decay curves, as compared with the no mesh and single mesh configurations. Increasing the number of meshes to ten, does not have a significant effect on the pH decay curves, as back-mixing is reduced due to a small spacing between consecutive mesh stages in this configuration.

The trends in the gas holdup profiles are similar, as seen in Fig. 5.11. In all cases, the gas holdup profiles show an increase over time. The gas holdup for the multiple mesh cases are much higher in comparison with the no mesh and single mesh cases, mainly due to the large amount of bubble cutting occurring in the column. The reduction in bubble size leads to an increased bubble residence time. The bubbles are also decelerated due to the significant hydrodynamic resistance offered by the multiple mesh stages. Henceforth, this leads to a notable increase in the gas holdup in for the multiple-mesh configuration. The high gas holdup explains the poor performance of the ten-mesh configuration, as bubble swarm effects can also lead to a reduction in the mass transfer rates. Therefore the combined effect of back-mixing and swarm effects counteracts the advantages offered by the reduced bubble sizes in the ten-mesh configuration. This explains the comparable performance of the six-mesh and ten-mesh configuration in terms of pH decay.

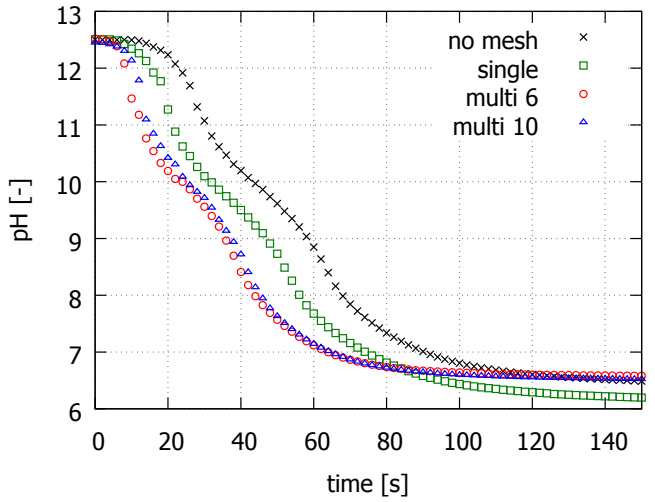

Figure 5.10: pH vs time curve at a superficial gas velocity of 20 mm/s with varying mesh stages for a mesh opening of 3.7 mm.

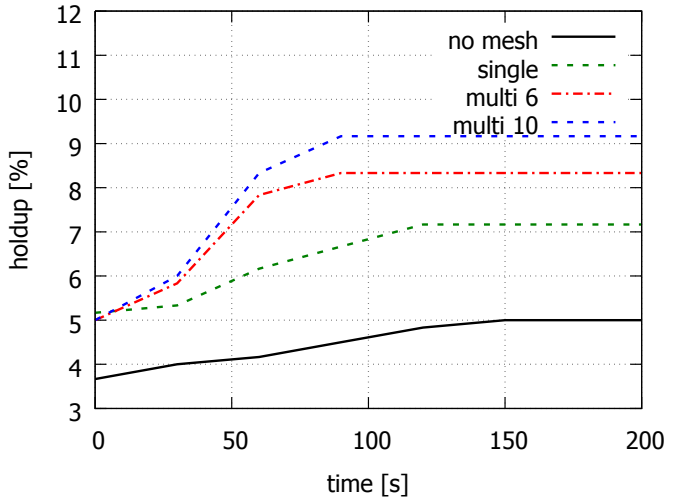

Figure 5.11: Gas holdup vs time curve at a superficial gas velocity of 20 mm/s with varying mesh stages for a mesh opening of 3.7 mm.

5.4.5 Comparison of experiments with VoF-DBM simulation

Single mesh configuration

Simulations were conducted for five superficial gas velocities (5, 10, 15, 20, 25 mm/s) to compare with experiments carried out with a wire mesh of 3.7 mm opening. The

mesh was placed at a height of 0.26 m from the bottom. A cutting efficiency of 0.1 was used for the simulations. The results of Sauter mean diameter, bubble size distribution, pH and gas holdup will now be discussed for a superficial gas velocity of 15 mm/s.

Fig. 5.12a shows the comparison of the Sauter mean diameter between experiments and simulations. The nature of the cutting in the model of Jain et al. (2013) is abrupt and occurs for all cases, whereas in experiments the cutting is gradual. The discrepancy between experiments and simulations is due to the high bubble coalescence rate before the mesh region. It can also be noticed that the initial bubble diameter in the simulations is set to 4 mm and it should be increased.

A comparison of the bubble size distributions is shown in Fig. 5.12b. It can be seen that the first peak of the experiments is not well captured in the simulations, as we do not model the violent breakup at the top interface. Experiments cannot detect bubbles below 0.3 mm whereas the simulation can keep track of these very small bubbles, resulting in a smoother initial curve in the simulations. However, the simulation captures the overall trend of the experiments fairly well.

Fig. 5.12c shows a comparison of the pH histories obtained experimentally and numerically. It can be seen that the two inflection points are well matched, which indicates that the reaction kinetics are a good description of reality. But the model under-predicts the pH decay rate. This could be due to the presence of large bubbles which in turn lead to lower rate of mass transfer. The time taken for neutralization (pH=7) is well captured by the model for all superficial gas velocities.

The gas holdup values match well between experiments and simulations as the error stays below 10% for all cases, except at time t=0 (as shown in Fig. 5.12d). The holdup predicted by simulations is lower than the experimentally determined value at time t=0, as a result of the differences in the startup procedure for chemisorption. In simulations, the hydrodynamics calculations are performed for a N_2 - $NaOH$ system until numerical effects disappear and then the system is switched to chemisorption at time t=0. The gas in reactor is completely switched to CO_2 and it reacts with $NaOH$, leading to disappearance of bubbles throughout the reactor. This causes a decrease in the gas holdup at the onset of chemisorption. However, in the experiments few N_2 bubbles are still present in the bubble column after startup in addition to CO_2 gas. As the N_2 bubbles do not react with $NaOH$, they have an added contribution to the gas holdup until they leave the column. The deviation in gas holdup predicted by simulations and experiments, lowers with time as seen in Fig. 5.12d.

Multiple-mesh configuration: six stages

Simulations were conducted for three superficial gas velocities [15, 20, 25 mm/s] to compare with experiments performed with a six stage multiple-mesh configuration using a mesh opening of 3.7 mm. The first mesh was placed at a distance of 0.05 m from the bottom and the spacings between consecutive meshes were 0.10 m. A cutting efficiency of 0.1 was used for the simulations. The results of the Sauter mean diameter, bubble size distribution, pH and gas holdup will now be discussed for a superficial gas velocity of 15 mm/s.

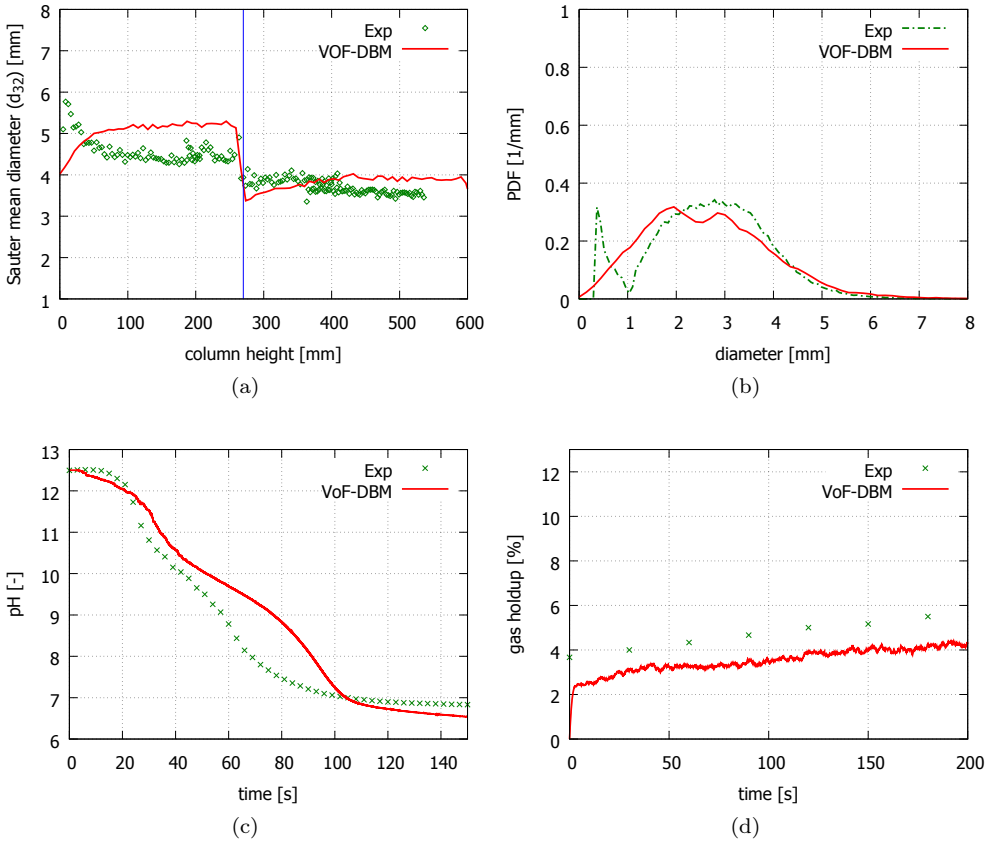

Figure 5.12: Behavior of the system with a mesh opening of 3.7 mm and a superficial gas velocity of 15 mm/s: (a) Sauter mean diameter [time averaged]. The location of the mesh at 0.26 m is indicated by the solid line (b) bubble size distribution [time averaged] in the top section [0.42 to 0.60 m] (c) pH vs time d) gas holdup vs time.

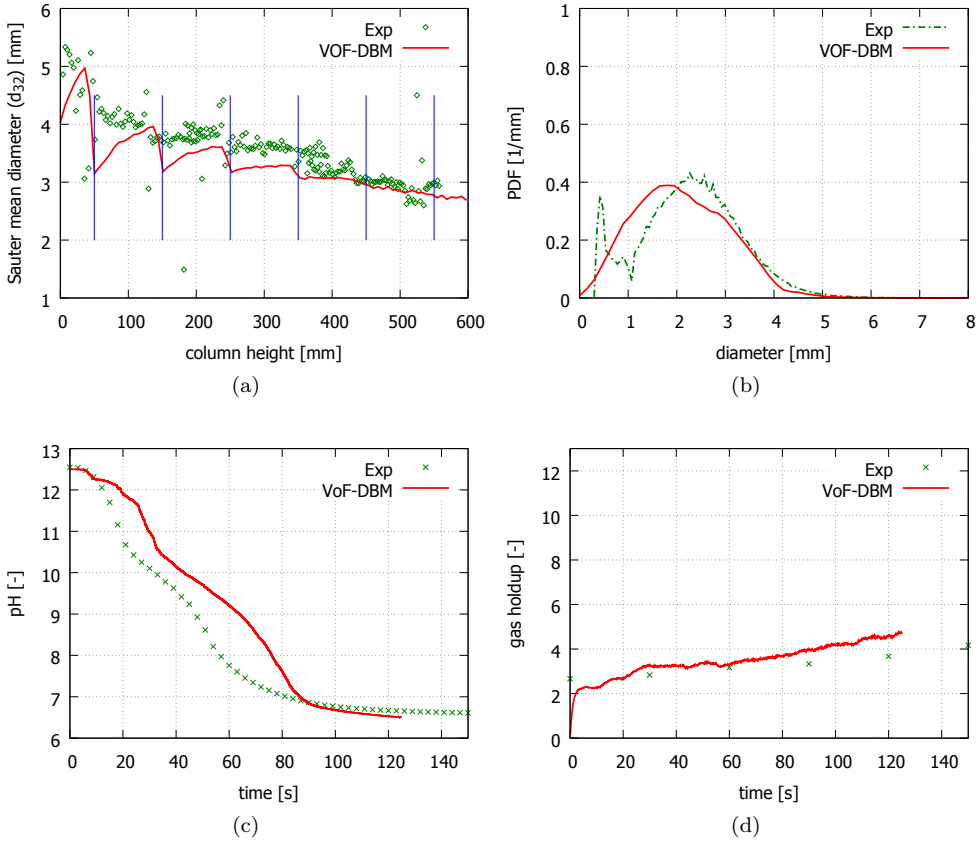

Figure 5.13: Behavior of the system with a mesh opening of 3.7 mm, 6 stages and a superficial gas velocity of 15 mm/s: (a) Sauter mean diameter [time averaged]. The location of the meshes are indicated by solid lines at 0.05, 0.15, 0.25, 0.35, 0.45, 0.55 m respectively. (b) bubble size distribution [time averaged] in the top section [0.42 to 0.60 m] (c) pH vs time (d) gas holdup vs time.

The Sauter mean diameter is well captured by the simulations as seen in Fig. 5.13a. An initial bubble diameter of 4 mm is used in the simulations, whereas a narrow bubble size distribution is generated during the experiments. This explains the mismatch in the Sauter mean diameter at the bottom of the column. In general, the cutting model predicts the overall trend of the Sauter mean diameter with good accuracy for the multiple-mesh configuration.

Fig. 5.13b compares the measured and simulated probability density functions (PDF) for the top section of the column [0.42 to 0.60 m]. The distributions demonstrate a very good match considering the simple model that was employed for the bubble cutting by the wire mesh.

The pH decay curves for the six stage multiple-mesh configuration are shown in Fig. 5.13c. The pH trends and reaction times are fairly well predicted by the VoF-DBM model as compared with the experiments. Fig. 5.13d shows the gas holdup vs time curves for the multiple-mesh configuration with six stages. The gas holdup is slightly over-predicted during the course of the reaction. The expected increase in gas holdup that is due to bubble cutting, is well captured in the simulations.

5.5 Conclusions

In this work, a detailed analysis of the micro-structured bubble column (MSBC) has been performed for the case of chemisorption of CO_2 into $NaOH$. Different internals such as a wire mesh and a Sulzer packing (SMV) have been tested in the MSBC experimentally to characterize the bubble cutting and mass transfer performance. The Sulzer packing and the wire mesh with a 3.7 mm opening shows good cutting characteristics as seen in their bubble size distribution. This increases the interfacial area in turn resulting in an increased gas holdup and better mass transfer performance. Since the chemisorption is mass transfer limited the reaction times are found to decrease significantly in presence of the internals. The multiple-mesh configuration with six staged meshes is seen to have a better performance than a single mesh due to the increased bubble cutting and gas holdup. The performance of the multiple-mesh configuration with ten stages is hindered by the decrease in back-mixing and reduction in mass transfer due to bubble swarm effects.

The VoF-DBM model is integrated with equations for chemisorption and validated with experiments. An optimal value of the cutting efficiency was determined and the simulation results are compared with experiments. The major drawback of the cutting model is that it is independent of the superficial gas velocity. Therefore an effort should be made to improve the cutting model by using closures from direct numerical simulations (DNS).

Nomenclature

Re	Reynolds number	
Sc	Schmidt number	
Sh	Sherwood number	
μ	dynamic viscosity	$[kg.m^{-1}.s^{-1}]$
ρ	density	$[kg.m^{-3}]$
ε	holdup	$[-$
A	area	$[m^2]$
D	depth	$[m]$
d	diameter	$[m]$
d_{32}	Sauter mean diameter	$[m]$
E	enhancement factor	$[-]$
F	color function	
H	height	$[m]$
h	height of gas-liquid dispersion	$[m]$
k_l	mass transfer coefficient	$[m.s^{-1}]$
N_S	number of species	
V	volume	$[m^3]$
v	velocity	$[m.s^{-1}]$
W	width	$[m]$
PDF	probability density function	$[1/mm]$
Y_j	mass fraction of species j	
0	initial	
b	bubble	
eq	equivalent	
f	final	
g	gas	
H	height expansion	
k	index	
l	liquid	
w	solid wire-mesh	
j	species index	
CO_2	carbon-dioxide	
$NaOH$	sodium hydroxide	
DBM	discrete bubble model	
DIA	digital image analysis	
MSBC	micro-structured bubble column	
SMV	Sulzer static mixer	
VoF	volume of fluid	

Chapter 6

Hydrodynamics of bubble cutting in micro-structured square bubble column using ultra-fast X-ray tomography

Bubble column reactors are used in the industry for both two-phase (gas-liquid) and three-phase (gas-liquid-solid) processes. In spite of their prevalence, the reactor performance is limited by the interfacial mass transfer and rate of heat removal. To overcome these disadvantages a novel reactor concept is proposed. It is a micro-structured bubble column reactor (MSBC), where the micro-structuring is realized by a wire-mesh. The wires are meant to efficiently cut the gas bubbles and exert a positive impact on the gas-liquid contact area in the bubble column, depending on the wire-mesh geometry (mesh opening/wire diameter). The scope of this research is to study the effect of the wire-mesh on the bubble cutting in an air-water system using ultrafast X-ray tomography. In this study, the effect of superficial gas velocity ($5 \leq v_g \leq 50$ mm/s) and superficial liquid velocity ($0 \leq v_l \leq 25$ mm/s) on the bubble cutting is investigated in a square micro-structured bubble column. The cross-sectional images show that after passing the wire mesh lamellar liquid film layers are created between the bubbles. From the bubble size distribution, it is seen that at superficial gas velocities exceeding 15 mm/s better cutting behavior is obtained. A cross-correlation technique is applied for superficial gas/liquid velocity until 25 mm/s. The bubble decelerates on approaching the mesh and accelerates on leaving the mesh. No significant effect of superficial liquid velocity on bubble cutting was observed in the experiments.

6.1 Introduction

Bubble columns are often used in the chemical industry for gas-liquid contacting processes. For instance, in gas-treating processes to remove H_2S and/or CO_2. The limiting step in the chemisorption process is usually the mass transfer from the gas phase to the liquid phase. The mass transfer rate is a function of the interfacial area, the intrinsic mass transfer coefficient and the driving force. The mass transfer rate can be increased by increasing the interfacial area and/or the interfacial mass transfer coefficient. This can be achieved by means of adding internals such as sieve plates, porous plates, and static mixers (SMV) (Baird, 1992; Deen et al., 2000). The addition of internals is known to reduce the back-mixing in the bubble column reactor, which can be advantageous in some situations. In our previous work, we have proposed a novel micro-structured bubble column (MSBC) reactor with wire-meshes as internals. Sujatha et al. (2015) have performed experiments in a laboratory scale MSBC reactor to study the effect of the wire mesh configuration and superficial gas velocity. Three hydrodynamic regimes were identified for bubbly flow in the MSBC with wire mesh in an air-water system for superficial gas velocities in the range of 5 to 50 mm/s.

The scope of the current paper is to extend the hydrodynamic study in a micro-structured bubble column from a pseudo-2D bubble column to a 3D square cross-sectioned column. Bubble size distribution and bubble velocity data are obtained from the tomography experiments. The effect of superficial gas velocity and superficial liquid velocity is determined for a wire-mesh with 3.7 mm mesh opening and 0.5 mm wire diameter, which turned out to be the most effective mesh in previous studies.

This paper is organized as follows. A brief literature review of different X-ray tomography scanners used to study multiphase flow is presented in the next section. This is followed by the description of the experimental setup and methods used for obtaining the results, i.e. a digital image analysis technique and cross-correlation method. Finally, we discuss the results of visual analysis and experimental results and present the main conclusions of this work.

6.2 X-ray tomography applied to process equipment

X-ray electron beam computed tomography is a non-invasive technique commonly used in the medical industry to obtain a 2/3 dimensional interior view of a patient. Medical X-ray scanners have a low temporal resolution of 2-3 scans per minute and can only be applied to scan stationary objects such as a patient that is lying still. This technique can be applied to scan a fast moving object by applying some modifications to the existing scanner. In the past decade, medical X-ray scanners have been modified to study the hydrodynamics of high-speed flow inside process equipment, such as bubble columns and fluidized beds. A brief summary of the different X-ray scanner configurations developed to study multiphase flows is presented in this section.

Hubers et al. (2005); Heindel et al. (2008) have developed an X-ray imaging system that consists of two X-ray source-detector pairs (offset 90°from each other) to visualize flow structures in a bubble column with 321 mm inner diameter. A schematic view of the scanner with rotating source-detector configuration is shown in Fig. 6.1. The

source and detectors are mounted on a ring which allows complete rotation around the bubble column. X-ray images are taken every 1°around a 360°path resulting in a time-averaged local phase distribution. Projections from each orientation are collected and reconstructed with standard algorithms. It is possible to acquire multiple slices simultaneously by employing different rows of the detector. The resulting data is reconstructed by using a multi-slice filtered back projection algorithm.

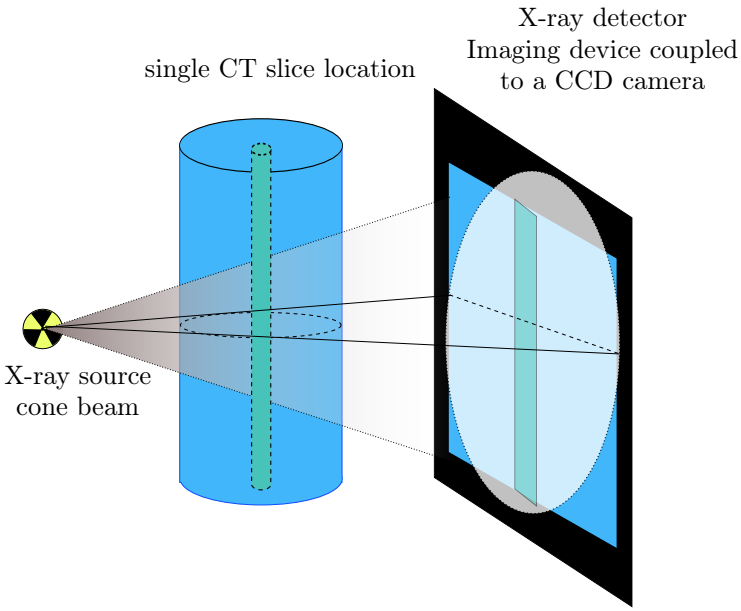

Figure 6.1: Schematic setup of tomography scanner with rotating source-detector configuration.

Mudde (2010) has developed a time-resolved tomography system with an effective temporal resolution of 250 frames per second. It is possible to expand the temporal resolution to 2500 frames per second by making certain modifications to the scanner configuration. The scanner consists of three pairs of source and detector placed around the object. Each detector has an array of 30 elements aligned opposite to the X-ray source. Fig. 6.2 shows the top view of the tomography scanner with three source-detectors placed around the object. The scanner has been used to study a perspex fluidized bed of 230 mm inner diameter filled with 0.56 mm polystyrene particles. The data is reconstructed by using an algebraic reconstruction technique (ART) as it offers more flexibility for limited data sets. They have demonstrated the working principle of the tomographic scanner in a fluidized bed to reconstruct spherical cap bubbles. Brouwer et al. (2012) utilized this scanner to extract bubble size and bubble velocity in a 250 mm diameter fluidized bed. The spatial resolution of the scanner is about 4.5 mm per pixel at a temporal resolution of 250 frames per second. They studied the effect of pressure and fines content on the bubble diameter for Geldart A

and B type particles. They found that increase in fines content and pressure leads to a reduction in the average bubble size.

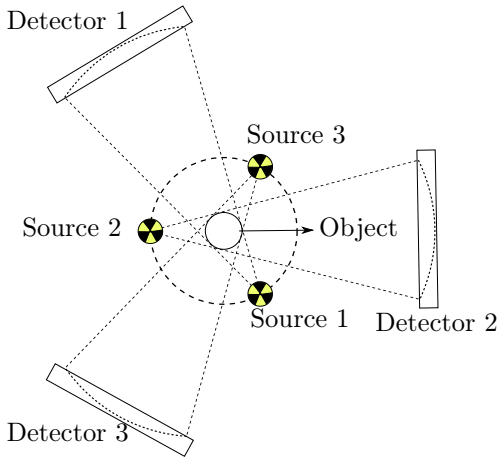

Figure 6.2: Top view of tomography scanner with three fixed source-detector pairs around the object.

Fischer et al. (Fischer et al., 2008; Fischer and Hampel, 2010) have applied fast X-ray tomography to a two-phase flow in a perspex bubble column of 60 mm inner diameter and 500 mm height. They used a single needle sparger to inject air into water and performed measurements at a height of 150 mm above the bottom of the vessel. The scan was performed at 5000 fps for a duration of 0.5 s. They used a filtered back projection method to reconstruct the attenuation data into cross-sectional images. The interfacial area is obtained as pseudo three-dimensional volume plots to prove the functional principle of the fast X-ray scanner.

Rabha et al. (2013a,b) studied the effect of particle size on the flow behavior of a slurry bubble column by using the fast X-ray tomography technique developed by (Fischer et al., 2008). Experiments were conducted in a cylindrical bubble column of 70 mm diameter and a height of 1500 mm. An air-water system with spherical glass particles was used as the gas-liquid-solid system of interest. They calculated the approximate bubble size distribution and gas holdup from the tomographic images based on treating the image sequence as a 3D volume. Note that their assumption of constant bubble velocity is invalid in cases with strong liquid recirculation and wide bubble size distribution. The experimental results are used for the verification of a Euler-Euler model implemented in Ansys CFX 14, for various solid fractions (0.01 to 0.20). Hence, they demonstrate that ultrafast electron beam X-ray tomography is applicable for the measurement of bubble size distribution and can give elaborate data on the hydrodynamics of a slurry bubble column.

Rabha et al. (2015) have also used the ultrafast X-ray tomography technique to study the effect of helical static mixer elements in a vertical bubble column of 80 mm inner diameter and 3.45 m in height. They studied different heights of the

column to visualize the flow structure evolution in a bubble column with internals. Experiments at turbulent operating conditions (0.11≤ v_g ≤0.42 m/s, v_l=0.2 and 0.6 m/s) were conducted for three different static mixer configurations to determine the gas flow structure, gas holdup, bubble size distribution and interfacial area. The number of static mixers strongly affects the gas holdup and interfacial area mainly at higher liquid velocities. The pressure drop is found to be mainly affected by the number of static mixers and the liquid velocity. Tomographic visualization provides detailed insight into the local flow behavior of gas-liquid flow in a bubble column with internals. Hence, X-ray tomography is a suitable technique to study local flow phenomena in reactors with internals as it does not suffer from the disadvantages of conventional imaging technique. It can be used to study reactors for industrial flows with high gas holdup as X-rays are not reflected by the bubbles like visible light.

6.3 Material and methods

6.3.1 Ultra-fast X-ray computed tomography

In this work, an ultra-fast X-ray tomography scanner based on the electron beam technology is used. This scanner was developed by Fischer et al. (2008) and has been used for two-phase flow studies where frame rates of 1 kHz or higher are required. The scanner comprises an electron beam gun with a fast deflection unit to focus the electron beam on a semicircular X-ray production target. The target is a semicircular metal ring made of tungsten alloy plates on a massive copper body. The X-ray detector ring is arranged with a slight offset of 5 mm relative to the plane of the focal spot path. The electron beam is swept across the object during the entire duration of the scan and the data from the detector is stored in a temporary RAM. After each scan, the data from the RAM is read out via a USB interface and the entire data set can be reconstructed offline. The data processing is summarized as follows: 1) Continuous data is broken into sets of size $N_D \times N_T$. N_D denotes the number of detectors and N_T denotes the number of equidistant temporal points for one complete electron beam revolution. This is achieved by evaluation of signals from the two extra detectors. Each of those data sets represents the raw data for one frame of the image sequence. 2) The raw data of each frame are mapped from the temporal domain into the angular domain of the target. The projection data matrix of size $N_D \times N_P$ is calculated. N_P is the number of equidistantly distributed source positions on the target. This transformation is non-linear since the source-trajectory is a cut of a skewed elliptical cone. 3) The projection data matrix is then sorted to a fan beam data. All data from the source positions outside the valid angular scanning range of 240° are discarded. 4) The line integral value for the fan beam data of each frame is calculated according to Eqn. 6.1.

$$E_{l,m} = -log\left(\frac{\phi_{l,m} - \phi_l^{(d)}}{\phi_{l,m}^{(0)} - \phi_l^{(d)}}\right) \tag{6.1}$$

Where ϕ denotes the X-ray intensity (which is represented by the acquired amplifier output voltage), l and m are indices of the detector and projection, superscript

(d) denotes a previously acquired dark reference and (0) a previously acquired reference measurement with no object in the scanned plane. The last step is the image reconstruction by using a filtered back projection technique. Fischer et al. (2008) has described the data processing in detail. Detailed information on different reconstruction algorithms for tomography data can be found in standard textbooks, such as Kak and Slaney (1988).

Digital image analysis technique to determine bubble size distribution

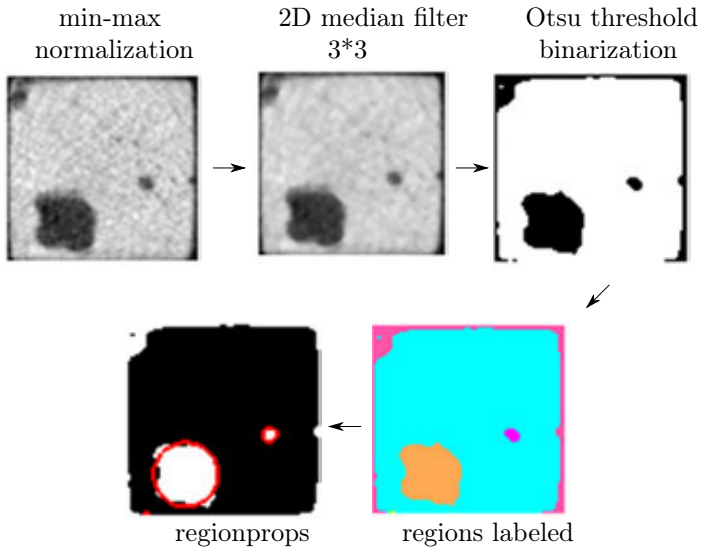

Figure 6.3: Processing steps of digital image analysis algorithm.

The ultra-fast X-ray tomography scanner has a pair of detector rings separated by a vertical distance of 11 mm. The lower plane and upper plane of the detector is also known as ring 0 and ring 1 respectively. Fig. 6.5 shows a schematic illustration of the ultra-fast X-ray tomography scanner. The reconstructed images are obtained for both the lower and upper imaging planes for all heights. Each image has a size of 128×128 pixels, in which each pixel has the value of the local linear X-ray attenuation coefficient that correlates to the local material density. Hence, the liquid phase and the bubbles appear with different gray levels in the cross-sectional images (See Fig. 6.6). The images (from the lower plane) are post-processed using the digital image analysis technique shown in Fig. 6.3. This algorithm is used to segment the bubbles from the background and to identify individual bubbles.

Fig. 6.3 gives a schematic of the major subsequent steps involved in the digital image analysis algorithm. The first step involves normalization of the image using the minimum and maximum intensity of the image over the entire 16-bit range. The second step is to remove noise in the image using a two-dimensional median filter.

The spatial resolution of the scanner is capable of resolving single bubbles larger than 1 mm, as smaller bubbles are eliminated as noise. The image noise is unavoidable as it is produced by the quantum noise of the X-ray source during the very short time acquisition for each projection. The third step is image binarization using a threshold automatically determined by the Otsu method. The resulting binary image consists of black bubbles on a white background. Finally, the objects are labeled and the area of each bubble is determined from the labeled image. Small bubbles that overlap with the image boundary are not detected properly. The equivalent diameter was determined from the bubble area as follows:

$$d_{eq} = \sqrt[2]{\frac{4A}{\pi}} \tag{6.2}$$

The probability density function (PDF) for a particular bubble diameter class is the ratio of number of bubbles in a particular diameter class (Δd_{eq}) to the sum of number of bubbles in all size classes. Therefore, the PDF of a particular size class (Δd_{eq}) is calculated from the number of bubbles and average bubble diameter as follows:

$$PDF_{\Delta d_{eq}} = \frac{N_{\Delta d_{eq}}}{\left(\sum_{\Delta d_{eq,min}}^{\Delta d_{eq,max}} N_{\Delta d_{eq,k}}\right)\Delta d_{eq}} \tag{6.3}$$

6.3.2 Cross-correlation technique to determine bubble velocity

A cross-correlation technique is used to obtain the bubble velocity by correlating images from the lower ring and the upper ring. The vertical distance between the detector rings is kept fixed at 11 mm. The imaging rate is 1000 frames per second for a duration of 10 seconds. Verma et al. (2014) have used a similar technique to determine the velocity of bubbles in a fluidized bed. The images are normalized using a local minimum (I_{min}) and local maximum values (I_{max}) obtained temporally for a particular filter width. An ideal filter width is chosen such that the intensity information of at least one small bubble and a large bubble are located in its domain. The intensity normalization is necessary to avoid bias in the velocity calculation towards large bubbles.

$$I_{k,norm} = \frac{I - I_{min}}{I_{max} - I_{min}} \tag{6.4}$$

The intensity normalized image is used for calculating the correlation strength ($\bar{R}(p,n)$) between the lower ring image $I_{1,norm}$ and the upper ring image $I_{2,norm}$ for various shift values at each pixel according to:

$$\bar{R}(p,n) = \frac{1}{N_f}\sum_{i=1}^{N_f-n} I_{1,norm}(p,i)\cdot I_{2,norm}(p,i+n) \tag{6.5}$$

where $I_{1,norm}$ and $I_{2,norm}$ are the normalized intensity of a pixel in the lower and upper frame, respectively, at the location p (pixel number). N_f is the total number

of frames. The index i indicates a frame number, and n is the number of frames over which the function is shifted. The mean correlation strength ($\bar{R}(n)$) over the entire image is determined for various shift values from:

$$\bar{R}(n) = \frac{1}{N_{pix}} \sum_{i=1}^{N_{pix}} \bar{R}(p,n) \tag{6.6}$$

where and N_{pix} is the total number of pixels in the cross-sectional measurement area. The cross-correlation function shows a maximum for a certain value of n, which we denote as the most probable shift n_D. The measured shift value n_D can be used to calculate the bubble velocity (v_b), given the vertical distance (Δz = 11 mm) and measurement frequency ($\nu = 1000 fps$):

$$v_b = \frac{dz}{dt} = \frac{\nu\ \Delta z}{n_D} \tag{6.7}$$

Fig. 6.4 shows an example of the cross-correlation function, showing a peak at n_D frames corresponding to a bubble velocity of v_b m/s.

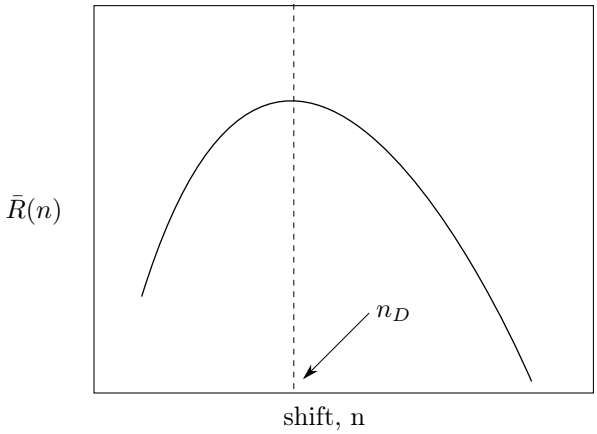

Figure 6.4: Cross-correlation function $\bar{R}(n)$ vs frame shift (n).

The cross-correlation technique does not give proper results when the bubbles change in shape between the lower and upper planes. The in-plane shift of the bubbles can also lead to problems with velocity calculation. Therefore, in practice, the cross-correlation technique only works at low superficial gas velocities.

6.3.3 Experimental setup and procedure

A square bubble column reactor of dimensions (width W=0.07 m, depth D=0.07 m, height H=1.3 m) is chosen for experiments. A schematic figure of the experimental setup is shown in Fig. 6.5. The reactor walls are constructed of transparent plexiglass to enable visual observation by the eye or using a camera. The plexiglass wall has

a slit on two sides (slit dimensions are 60 mm×30 mm.) at a height of 1 m from the bottom plate, to allow for the liquid to overflow to a storage vessel. The liquid recirculation arrangement is illustrated in the side view in Fig. 6.5b. A liquid pump is used to recirculate the liquid into the column at a set flow-rate, through a liquid distributor. The liquid distributor has perforations of 3.2 mm diameter, arranged in a 6×6 square pitch of 10 mm. The gas is fed into the column via a group of twenty-five gas needles arranged in a 5×5 square pitch at the distributor plate. The needles have a length (L) = 50 mm, inner diameter (I.D.) = 1 mm and outer diameter (O.D.) = 1.5875 mm. The needles extend 10 mm above the bottom plate and are spaced with a center-to-center distance of 10 mm. Two mass flow controllers are used to control the gas flow rates in the column. Micro-structuring in the reactor is realized by means of a wire mesh with a 3.7 mm mesh opening and 0.5 mm wire diameter. The location of the wire mesh was fixed for the experiments at a distance of 0.5 m above the bottom distributor plate.

Images are captured at five different heights in the square column using a dual plane fast X-ray tomography technique. The images are captured at a frequency of 1000 Hz for a duration of 10 s. Position P1 and P4 are located at 0.25 m and 0.75 m from the bottom distributor plate respectively. P1 and P4 provide information on the bubble size distribution away from the wire mesh. Position P2 and P3 are placed at a distance of 0.05 m above and 0.05 m below the wire mesh plane respectively (at height 0.5 m) . Wire mesh position (WM) is centered such that the dual ring detector array coincides with the center of the column (at height 0.5 m with the detectors just below and above the wire mesh). The positions P2, P3 and WM provides details on the bubble size distribution and bubble velocity close to the wire mesh. The exact position of dual planes of the X-ray detector at different height (P1, P2, WM, P3, P4) in the column is described in Table 6.1.

Position	lower plane/ring 0	upper plane/ring1
P1	0.25	0.261
P2	0.45	0.461
WM	0.495	0.506
P3	0.55	0.561
P4	0.75	0.761

Table 6.1: Position of dual-planes of the X-ray detector at different height in the column. All dimensions are in meters.

6.4 Results

The visual observation gives a general idea of the hydrodynamics in the MSBC for various superficial gas/liquid velocities. The effect of superficial gas and liquid velocity on bubble cutting is obtained by analyzing the results of bubble size distribution and bubble velocity.

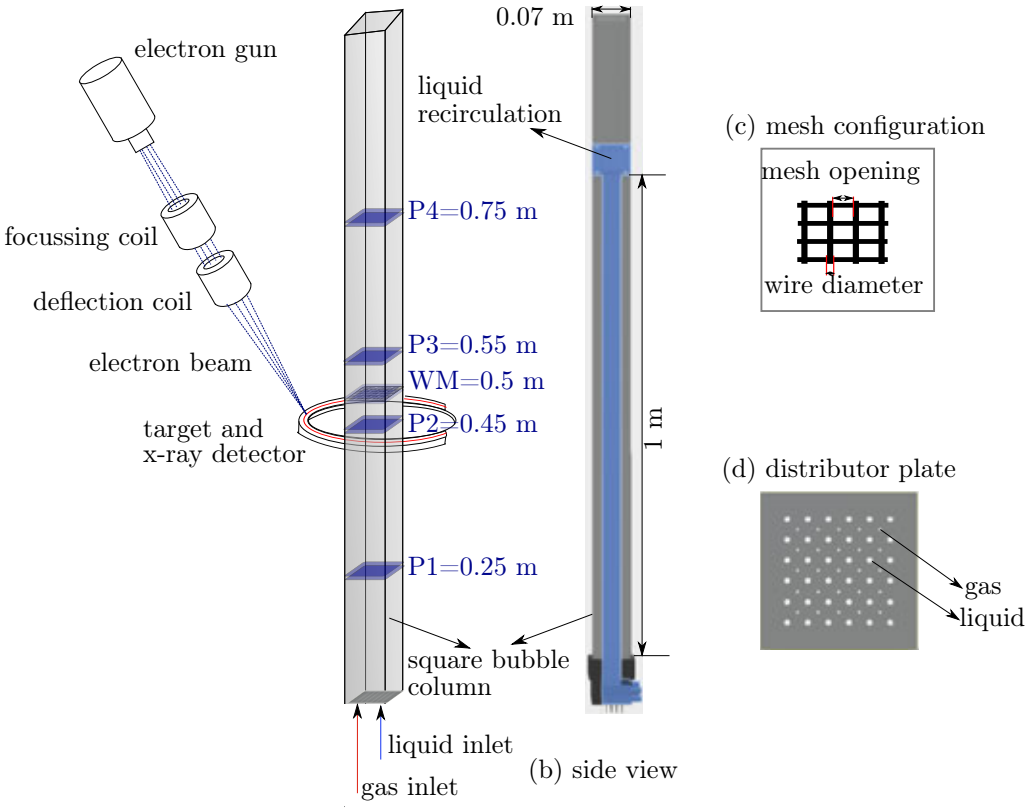

Figure 6.5: Schematic illustration of the micro-structured bubble column under the ultra-fast X-ray tomography scanner. (a) schematic view, (b) side view showing liquid circulation arrangement, (c) mesh configuration, (d) distributor plate.

6.4.1 Visual observation

Images are obtained by reconstruction of the experimental data obtained from the X-ray scanner. The image in Fig. 6.6 (left) shows the bubble before it passes through the wire mesh. The formation of lamellar liquid film layers between large bubbles can be observed in Fig. 6.6 (right). The bubbles are separated by the lamellar film layer and tend to re-coalesce when the contact/interaction time is longer than the film drainage time. In case the contact time is shorter than the film drainage time, the bubbles bounce back or break apart as separate daughter bubbles. It can be inferred from the visual observation that the wire mesh has a clear intrusive effect on large bubbles that pass through. However, a bubble smaller than the mesh opening can pass through the mesh with little or no effect.

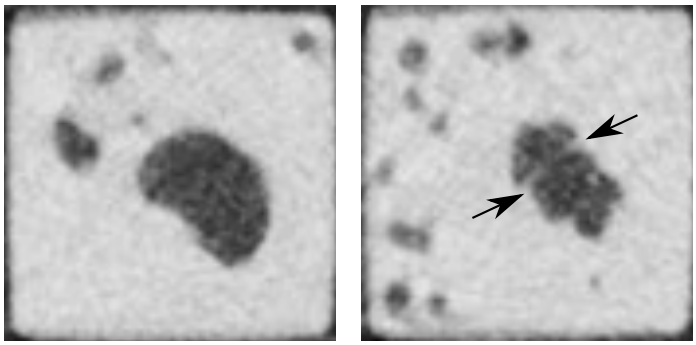

Figure 6.6: Cross-sectional image of micro-structured bubble column at the position of wire mesh (WM). Left: Image shows bubbles just before passing through the wire mesh. Right: Image shows lamellar liquid films (indicated by arrows) after the bubbles have passed through the wire mesh.

6.4.2 Influence of wire mesh at different heights of the column

The bubble size distribution for different heights of the column is plotted for the lower plane in Fig. 6.7 at a superficial gas velocity of 10 mm/s. The positions P2, WM and P3 are located close to the wire mesh. Therefore, the results of the bubble size distribution at these positions offer an insight into the bubble cutting by the wire mesh. It can be seen that small bubbles in the position P2 coalesce when they reach the WM position (below mesh), evidenced by the peak at 5 - 7 mm. The WM position has a bimodal distribution consisting of small and large bubbles. The bimodal distribution in the position below the mesh (WM) leads to a widely varying distribution above the mesh (P3) with a large fraction of small bubbles. At P3 a large peak at a diameter of 2.5 mm can be seen, along with some scattered peaks for bubble sizes of 5 - 13 mm. Hence, it can be concluded that both bubble cutting, as well as (rapid) bubble coalescence, take place when the bubbles pass through the wire mesh.

6.4.3 Effect of superficial gas velocity

The cross-sectional images from subsequent frames are stacked (temporal stacking) to synthesize image sequences. The pseudo-vertical images of the bubbles patterns below (ring 0) and above (ring 1) are obtained to show the effect of superficial gas velocity ($5 \leq v_g \leq 40$ mm/s) at the superficial liquid velocity of 0 mm/s, as seen in Fig. 6.8. The flow structure obtained for $v_g = 5$ mm/s is characterized by small bubbles corresponding to homogeneous flow regime. At $v_g = 10$ mm/s, the flow is dominated by small bubbles with the occurrence of a few large bubbles due to bubble coalescence. Most bubbles can pass through the wire mesh without being cut due to their small size. For $v_g = 20$ mm/s, the bubbles coalesce below the mesh to form large bubbles. These are subsequently cut into small bubbles as they pass through the mesh. The bubble cutting/breakup occurs with little effort at the superficial gas

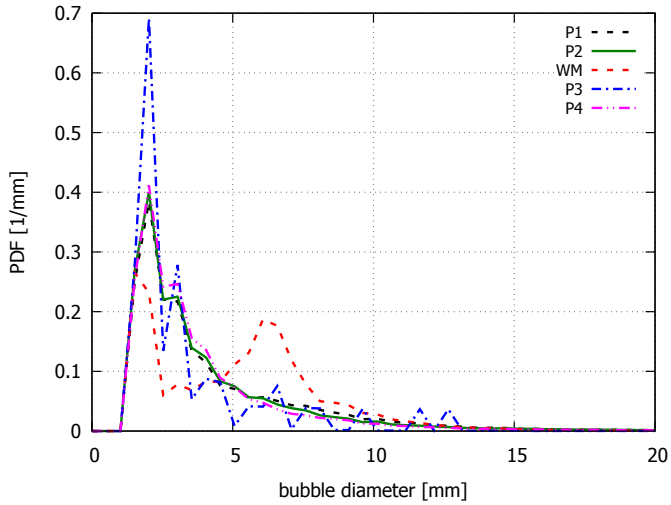

Figure 6.7: Bubble size distribution (PDF) at the superficial gas velocity of 10 mm/s and superficial liquid velocity of 0 mm/s at different heights of column (P1, P2, WM, P3, P4) at lower plane (ring 0).

velocity above 30 mm/s, evidenced by the presence of small bubbles above the wire mesh.

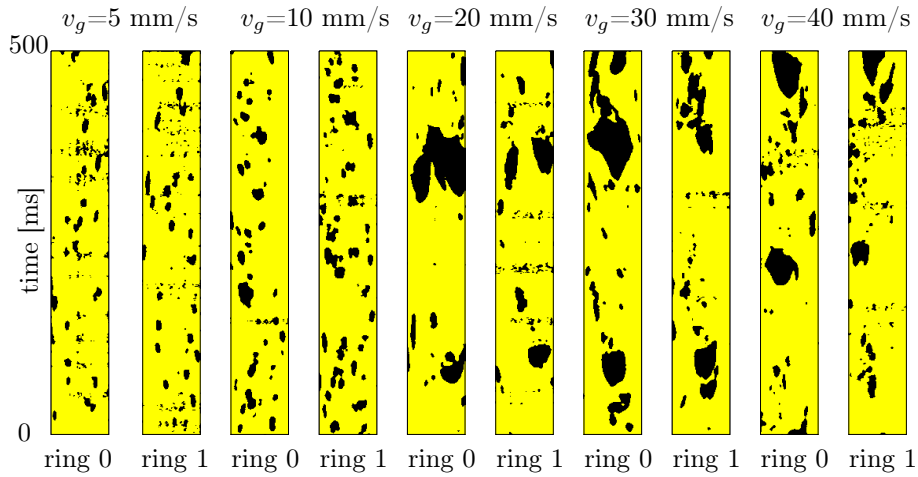

Figure 6.8: Pseudo-vertical images of the bubble patterns below (ring 0) and above (ring 1) to show the effect of v_g at $v_l = 0$ mm/s at wire mesh position (WM). Each image sequence has been synthesized from 500 cross-sectional slice images. Note that the vertical coordinate is the time coordinate.

Fig. 6.9 and Fig. 6.10 show the bubble size distributions for varying superficial gas velocity ranging from 5 to 40 mm/s and superficial liquid velocities of 0 mm/s and 2 mm/s respectively. At the superficial gas velocity of 5 mm/s, a narrow bubble size distribution is found with a mean bubble size of around 2.25 mm. As the velocity is increased to 10 mm/s the regime transition promotes bubble coalescence leading to a bimodal bubble size distribution. This regime transition is also visible in the pseudo-vertical images in Fig. 6.8. For $v_g \geq 10$ mm/s, the bubble coalescence leads to the formation of large slugs and small bubbles in the column. The bubble size distribution in Fig. 6.9 and Fig. 6.10 does not show large slugs (d_{eq} >20 mm) as they are significantly low in number when compared to the small bubbles. It can be seen from the bubble size distribution that the fraction of small bubbles (1 mm <d_{eq} <15 mm) does not change significantly for different velocities (5 mm/s, 20 to 40 mm/s). However, it should be noted that there is a transition from homogeneous bubbly flow to heterogeneous regime within this range of v_g. Therefore, the bubble size distribution (based on the number of bubbles) does not give a clear picture on the hydrodynamics of bubble cutting in the MSBC. Since the experiments were not performed for a bubble column without meshes, there is no benchmark to compare the results of bubble size distribution obtained for the MSBC reactor.

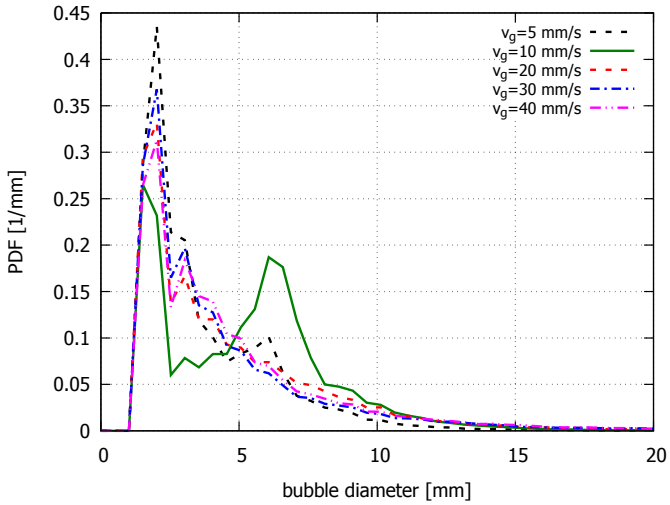

Figure 6.9: Bubble size distribution at constant superficial liquid velocity of 0 mm/s and varying superficial gas velocity ranging from 5 to 40 mm/s at WM position (lower plane).

Bubble velocities were calculated by using the cross-correlation technique for all experiments. It can be seen in Fig. 6.11 and Fig. 6.12, that bubbles tend to decelerate as they approach the mesh (decreasing velocity from P1 and P2 to WM). The mesh is indicated by the blue solid line. The bubble velocity is the lowest when the bubble comes in contact with the wire mesh position (WM). As the bubbles leave the wire

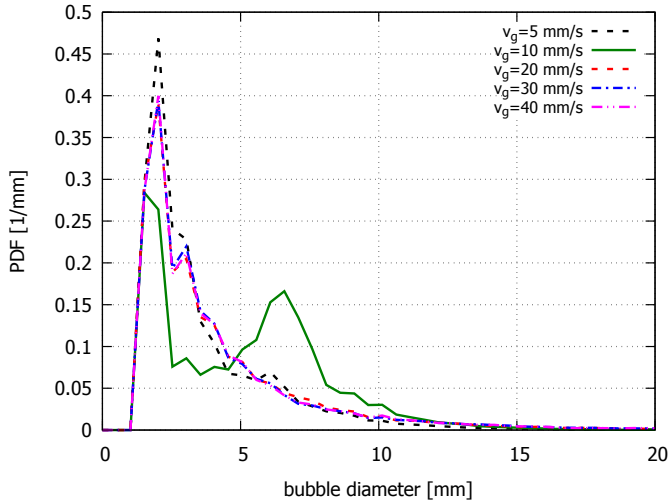

Figure 6.10: Bubble size distribution at constant superficial liquid velocity of 2 mm/s and varying superficial gas velocity ranging from 5 to 40 mm/s at WM position (lower plane).

mesh they accelerate to reach a steady rise velocity as seen in position P3 and P4. Therefore, the wire mesh has a significant effect on the bubble rise velocity and thereby increases the residence time of the bubbles in the reactor. This effect also leads to an increase in the gas holdup in the bubble column with mesh internals. A general increase in bubble rise velocity is observed when the superficial gas velocity is increased from 5 to 25 mm/s.

6.4.4 Effect of superficial liquid velocity

Fig. 6.13 shows the pseudo-vertical images obtained for different superficial liquid velocity ($0 \leq v_l \leq 25$ mm/s) at a superficial gas velocity of 10 mm/s. As the superficial liquid velocity is increased larger bubbles can be seen in the images. The presence of large bubbles leads to a decrease in the gas holdup and henceforth the interfacial area of bubbles in the reactor decreases. The visual observation does not indicate a significant effect of superficial liquid velocity on the bubble cutting in the micro-structured bubble column, except at the superficial liquid velocity of 25 mm/s. The available experimental data is insufficient to establish the relationship between the superficial liquid velocity and the bubble cutting in the MSBC reactor. Therefore, experiments for liquid velocity above 25 mm/s can provide more insight into the effect of liquid velocity on bubble cutting.

Fig. 6.14 and Fig. 6.15 show the bubble size distribution for varying superficial liquid velocity ranging from 0 to 25 mm/s and superficial gas velocity of 10 mm/s and 20 mm/s respectively. A bimodal bubble size distribution is observed for different superficial liquid velocities shown in Fig. 6.14. At $v_l = 0$ mm/s, there exists a bimodal

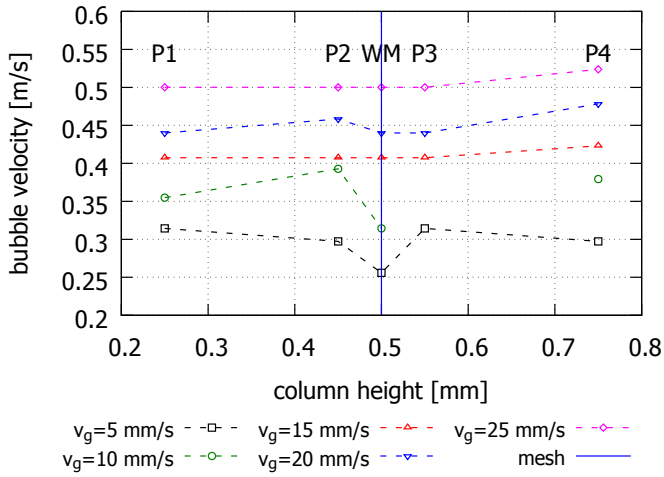

Figure 6.11: Bubble velocity at constant superficial liquid velocity of 0 mm/s and varying superficial gas velocity ranging from 5 to 25 mm/s. The location of the wire mesh is shown by the blue solid line at a column height of 0.5 m.

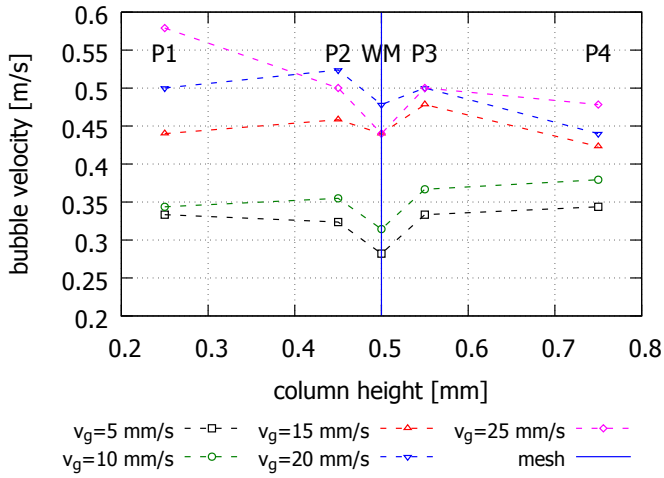

Figure 6.12: Bubble velocity at constant superficial liquid velocity of 20 mm/s and varying superficial gas velocity ranging from 5 to 25 mm/s. The location of the wire mesh is shown by the blue solid line at a column height of 0.5 m.

bubble size distribution characteristic of $v_g = 10$ mm/s. Upon imparting the liquid velocity of 5 mm/s an increase in bubble coalescence occurs. The small peak in Fig.

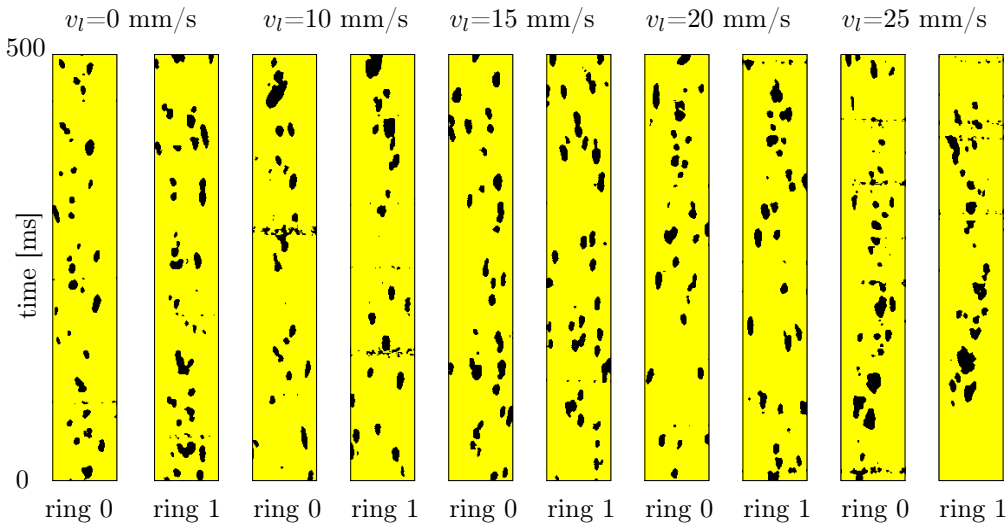

Figure 6.13: Pseudo-vertical images of the bubble patterns below (ring 0) and above (ring 1) to show the effect of v_l at v_g = 10 mm/s at wire mesh position (WM). Each image sequence has been synthesized from 500 cross-sectional slice images. Note that the vertical coordinate is the time coordinate.

6.14 between 16-18 mm proves the increase in bubble coalescence. On increasing the superficial liquid velocity above 5 mm/s, the bubble size distribution is similar to v_l = 0 mm/s with an insignificant change in the number of small bubbles. For superficial gas velocity of 20 mm/s, the liquid velocity has no effect on the coalescence and breakup as a narrow bubble size distribution with overlap is seen for superficial liquid velocity ranging from 0 to 25 mm/s. Hence, it can be concluded that the range of superficial liquid velocity ($0 \leq v_l \leq 25$ mm/s) does not affect the bubble size distribution as expected.

The bubble velocity was calculated by using the cross-correlation technique for all experiments. It can be seen in Fig. 6.16 that increasing the superficial liquid velocity (v_l >0) only has a small effect on the prevailing bubble velocity. This observation agrees with the earlier remark that the superficial liquid velocity does not affect the bubble size distribution in the MSBC equipped with wire mesh (3.7 mm mesh opening).

6.5 Conclusions

This study shows the effect of superficial gas velocity ($5 \leq v_g \leq 40$ mm/s) and superficial liquid velocity ($0 \leq v_l \leq 25$ mm/s) on the hydrodynamics of a square micro-structured bubble column. Results in terms of the bubble size distribution and bubble velocity are obtained by using an ultra-fast electron beam X-ray tomography technique. All the bubbles within different planes in the column can be resolved prop-

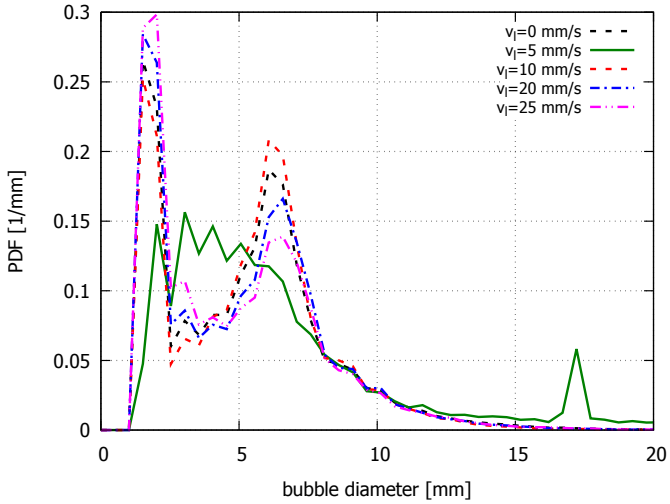

Figure 6.14: Bubble size distribution at the superficial gas velocity of 10 mm/s and superficial liquid velocity ranging from 0 to 25 mm/s at WM position (lower plane).

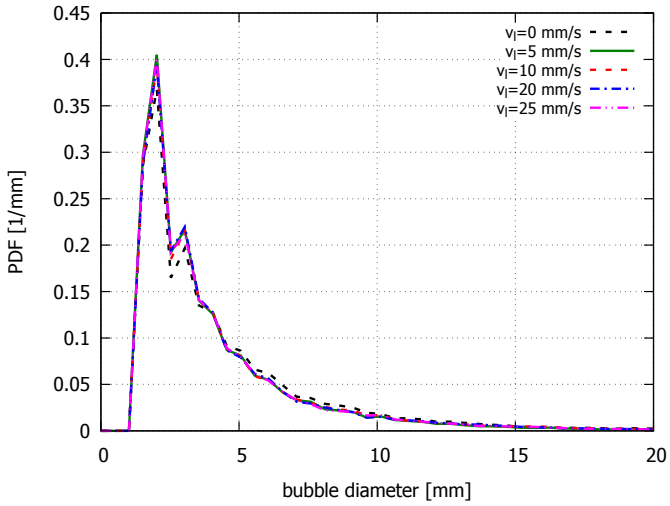

Figure 6.15: Bubble size distribution at the superficial gas velocity of 20 mm/s and superficial liquid velocity ranging from 0 to 25 mm/s at WM position (lower plane).

erly and even the thin liquid film between single bubbles can be discerned. Lamellar liquid film formation is visible when bubbles leave the mesh. This confirms the impact of the wire mesh on the large bubbles in the micro-structured bubble column. From the bubble size distribution, it can be seen that at superficial gas velocities exceed-

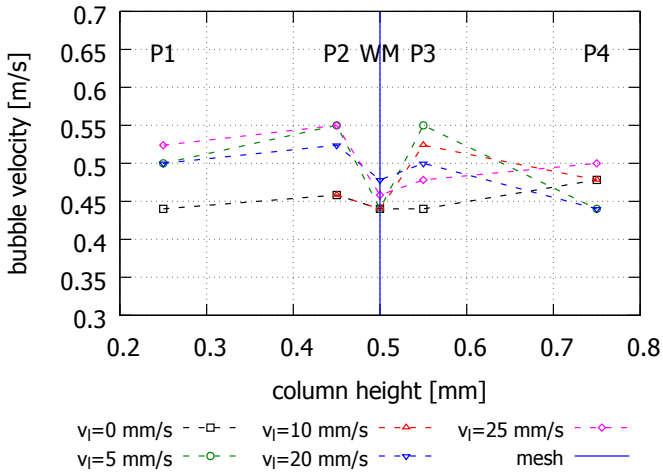

Figure 6.16: Bubble velocity at a fixed superficial gas velocity of 20 mm/s and superficial liquid velocities ranging from 0 to 25 mm/s. The location of the wire mesh is shown by the blue solid line at a column height of 0.5 m.

ing 15 mm/s better cutting behavior is observed. A cross-correlation technique can only be applied at low superficial gas/liquid velocities for the determination of the bubble rise velocity. At high velocities, the technique breaks down due to flow inhomogeneities. The bubble velocity at different heights of the column shows that the bubbles decelerate on approaching the mesh and accelerate after leaving the mesh. The increase of superficial liquid velocity from 0 to 25 mm/s does not enhance the bubble cutting, and only slightly increase the bubble velocity. The present study provides experimental data that can be used for validation of Euler-Lagrange simulations of a micro-structured bubble column with wire mesh internals. Experiments for superficial liquid velocities above 25 mm/s are required to investigate the impact of liquid velocity on bubble cutting.

Nomenclature

d	Diameter	$[m]$
W	Width	$[m]$
H	Height	$[m]$
D	Depth	$[m]$
A	Area	$[m^2]$
eq	Equivalent	
k	Index	
DIA	Digital Image Analysis	
PDF	probability density function	$[1/mm]$
E	Extinction matrix with line integral value for the fan beam data	
l, m	Indices of detector and projection respectively	
N_D	Number of detectors	
N_T	Number of equidistant temporal points per revolution	
N_P	Number of equidistant X-ray source positions	
Δd_{eq}	Size class of bubbles	$[mm]$
$N_{\Delta d_{eq}}$	Number of bubbles in a particular diameter class	$[mm]$
ϕ	X-ray intensity	
ϕ^d	Dark reference	
ϕ^0	Empty reference	
$I_{k,norm}$	Normalized intensity image. k =1 lower ring; k=2 upper ring	
I_{min}	Image local minimum	
I_{max}	Image local maximum	
$\bar{R}(p, n)$	Correlation strength between lower ring and upper ring image	
$\bar{R}(n)$	Cross-correlation function	
N_f	Total number of frames	
N_{pix}	Total number of pixels in the cross-section	
i	Index of image frame	
n	Value of shift between image frames	
p	Pixel number	
n_D	Value of shift for maximum in cross-correlation function	
v_b	Bubble velocity	$[m/s]$
ν	Measurement frequency	$[frames/s]$
Δz	Vertical distance between the image planes	$[m]$
dt	Time difference	$[s]$
v_g	Superficial gas velocity	$[mm/s]$
v_l	Superficial liquid velocity	$[mm/s]$

CHAPTER 7

EPILOGUE

In the previous chapters, the performance of a micro-structured bubble column (MSBC) was studied for different systems of gas-liquid, ranging from physical absorption to chemisorption. The experimental results with chemisorption are also used for the validation of the Euler-Lagrange simulations. The effect of a number of wire meshes on bubble cutting and bubble size distribution has been investigated in the system with chemisorption. The effect of liquid surface tension on bubble cutting is investigated in a dodecane-nitrogen system. In all cases, it can be seen that the wire mesh can be effectively used for the reduction of bubble sizes in a laboratory scale bubble column reactor. Increasing the number of wire meshes leads to a narrow distribution of bubble sizes with the high gas holdup.

In this chapter, some preliminary results are presented, along with recommendations for future work. First the interaction of single bubbles with a wire mesh in a glycerol-water mixture is discussed. Subsequently, the effect of coating the wire mesh with a superhydrophobic layer is explored. Finally, some recommendations are made for alternative wire mesh configurations that can be investigated.

7.1 Hydrodynamic interaction of single bubble with wire mesh in a glycerol-water mixture

Preliminary experiments have been conducted for single bubbles in a glycerol-water mixture. Three different outcomes can arise when a bubble interacts with the wire mesh: a) the bubble is cut by the mesh b) the bubble can get stuck underneath the mesh c) the bubble deforms and squeezes through the mesh opening. The result of the interaction of bubbles with the wire mesh depends on parameters such as bubble size, wire diameter, mesh opening, physico-chemical parameters of the gas and the liquid.

The bubble velocity is also an important parameter that influences the bubble cutting, as the residence time of the bubble at the mesh is controlled by the bubble velocity before it reaches the mesh. Hence, the physical process underlying the bubble cutting is quite complex and a simple phenomenological model with geometrical consideration is insufficient to describe the bubble-mesh interactions. Therefore, the bubble cutting model discussed in Chapter 5 requires improvement and could be replaced by a better closure derived from direct numerical simulation (DNS) studies.

The main problem in performing reliable single bubble measurements in glycerol mixtures is the contamination of the mixture over time. Another problem is the variability involved with the impact of the bubbles with the wire mesh. Fig. 7.1a shows the current setup used for single bubble experiments in a glycerol-water mixture. A square bubble column of 20 cm in diameter and a height of 1.3 m is used for experiments. The wire mesh is placed at a distance of 0.3 m from the bottom of the column and the column is filled with a glycerol-water mixture up to a height of 0.5 m. A cylindrical spoon movable in the horizontal direction is used for releasing a single bubble into the column. The bubble is released into the column by rotating the spoon slowly. The impact location of the bubbles on the wire mesh in the current experimental setup is somewhat arbitrary due to the oscillatory motion of the bubbles in the liquid. By using an inverted funnel at the bubble inlet as shown in Fig. 7.1b, more control can be obtained over the exact impact location of the bubble at the wire mesh. By performing reliable experiments, a relationship can be derived for the daughter bubble size distribution as a function of parent bubble size, velocity, impact location and the physico-chemical properties of the gas and liquid.

Fig. 7.2 shows the image sequence of a bubble which has its centroid aligned with the wire mesh rib. It can be seen that two asymmetrical daughter bubbles are generated when the bubbles pass through the mesh. The asymmetry in bubble cutting can be explained by a Laplace pressure effect. According to Laplace's law, the pressure increment of a curved surface is inversely related to the radius of the bubble. The smaller bubble has a higher pressure than the large bubble, resulting in air from the small bubble to transfer to the large bubble until the pressure gradient vanishes. The contact time of the bubbles with the wire mesh and the pressure gradient between the bubble parts dictates the extent of asymmetry in the daughter size distribution. If the bubble impacts the wire mesh at reasonably high velocity, a 'perfect' symmetric cut can be expected.

7.2 Effect of a coated wire mesh on bubble cutting

To check the influence of the surface properties of the wire mesh, a hydrophilic mesh was made of stainless steel wires with a contact angle of 64°. The wire mesh was coated by using galvanic deposition of silver on the copper wire mesh. Larmour et al. (2007) has described the procedure to prepare superhydrophobic coating on a copper substrate. The copper wires are to be cleaned mechanically and chemically to remove any oily residues. The meshes are immersed in silver nitrate solution for 60 s and then washed with water. Subsequently the meshes are immersed in a solution of 1 mmol L-1 3,3,4,4,5,5,6,6,7,7,8,8,9,9,10,10,10-heptadecafluoro-1-decanethiol (HDFT)

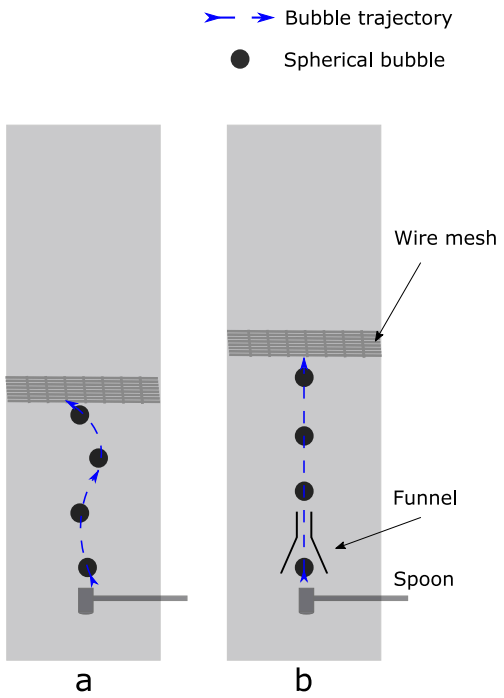

Figure 7.1: Schematic front view of experimental setup used for single bubble cutting a) current setup b) new setup.

Figure 7.2: Image sequence of a bubble which has its centroid aligned with the wire rib. The time interval between the images is 0.12 s.

in dichloromethane for 5 min and dried with compressed air. It is not possible to measure the contact angle on the cylindrical mesh, therefore a coated copper plate is used instead to obtain an approximate value. The contact angle of a coated copper plate was found to be 150°. Fig. 7.3 shows the single bubble impacting the mesh at the same location for the case of coated and uncoated copper mesh. It can be seen that there is no influence of the hydrophobic coating on the time scale of the bubble cutting process, which appears to be faster than the time scale for draining the liquid film between the bubble and the wire mesh. Hence, it can be concluded that the length scale of the coating (micro and nanometers) is too small to have any effect on

the bubble cutting process.

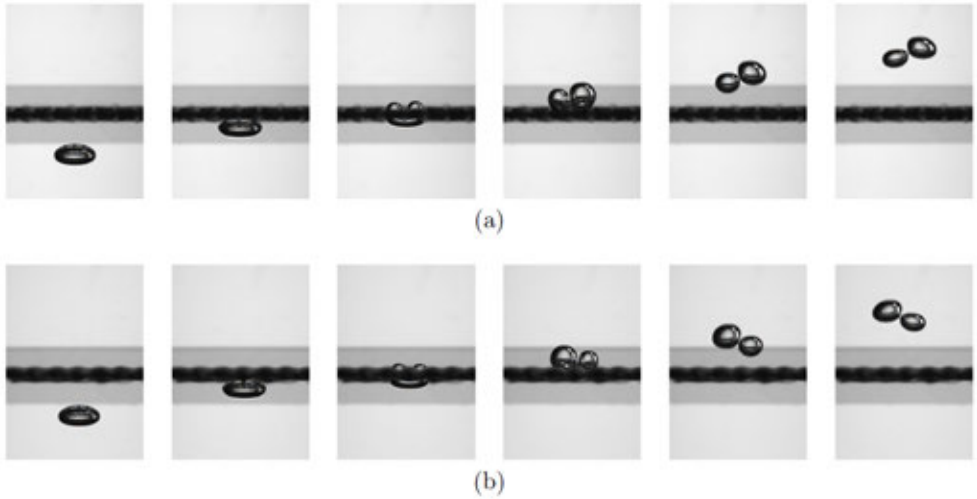

Figure 7.3: Image sequence of two bubble cutting experiments. (a) uncoated mesh (b) coated mesh with a superhydrophobic layer. The time interval between images is 0.03 s.

7.3 Alternate configurations of wire mesh

Several alternate wire mesh configurations that can be investigated are shown in Fig. 7.4. The uniform mesh with constant mesh opening has been investigated in this work. Alternate configurations including rhombus, hexagonal and triangular meshes are commercially readily available in various dimensions. However, it is recommended to perform future experiments with 3D printed wire meshes to have precise control over the wire mesh geometry, on the basis of mesh variables such as wire diameter, mesh opening or pitch of the mesh.

The mesh with refinement is a special case, where small mesh openings are concentrated at the center of the column to cut or disturb especially the large bubbles. The mesh with refinement is expected to have a positive effect on the performance of an industrial bubble column reactor. The shape of the mesh opening (rhombus, hexagonal or triangular) is expected to have an impact on the daughter bubble size distribution due to difference in bubble-wire interactions. The pressure drop of the different mesh type can elucidate the amount of hydrodynamic resistance offered by the wire-mesh structure. It is worthwhile to investigate the extent of shape oscillations induced when the bubbles pass through the mesh for different configurations. The frequency and the duration of the bubble shape oscillations can have an effect on the overall rate of gas-liquid mass transfer and hence have an impact on the performance of the MSBC.

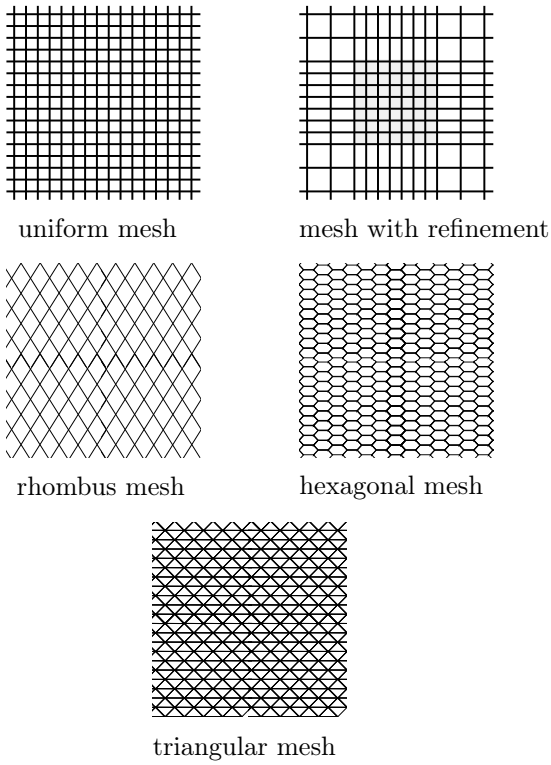

Figure 7.4: Various mesh configuration.

Further understanding of the micro-structured bubble column at laboratory scale is required before the MSBC can be scaled up to larger dimensions. The possibility of coating the wire mesh with catalyst as an alternative to a slurry bubble column is not yet investigated. Direct numerical simulation and single bubble cutting experiments can provide a wealth of information on the physics of bubble cutting at the wire mesh.

References

Akita, K., Yoshida, F., 1973. Gas Holdup and Volumetric Mass Transfer Coefficient in Bubble Columns. Effects of Liquid Properties. Industrial & Engineering Chemistry Process Design and Development 12 (1), 76–80.

Akita, K., Yoshida, F., 1974. Bubble Size, Interfacial Area and Liquid-phase Mass transfer Coefficient in Bubble Columns, Industrial and Engineering Chemistry. Process Design and Development 13 (1), 84–91.

Allen, M. P., Tildesley, D. J., 1989. Computer simulation of liquids. Oxford university press.

Baird, M. H. I., 1992. Bubble column reactors. By W.-D. Deckwer, Wiley, New York, 1991. AIChE Journal 38 (8), 1305–1305.

Baltussen, M. W., 2015. Bubbles on the cutting edge: direct numerical simulations of gas-liquid-solid three-phase flows. Ph.D. thesis, Technische Universiteit Eindhoven.

Baten., J. M. V., Krishna, R., 2003. Scale up studies on partitioned bubble column reactors with the aid of CFD simulations. Catalysis today 79, 219–227.

Boyer, C., Duquenne, A.-M., Wild, G., 2002. Measuring techniques in gas–liquid and gas–liquid–solid reactors. Chem. Eng. Sci. 57 (16), 3185–3215.

Brauer, H., 1981. Particle/fluid transport processes. Progress in Chemical Engineering 19, 81–111.

Brouwer, G. C., Wagner, E. C., van Ommen, J. R., Mudde, R. F., 2012. Effects of pressure and fines content on bubble diameter in a fluidized bed studied using fast X-ray tomography. Chem. Eng. J. 207-208, 711–717.

Chang, H. N., Halard, B., Moo-Young, M., 1989. Measurement of KLa by a gassing-in method with oxygen-enriched air. Biotechnology and bioengineering 34 (9), 1147–1157.

Chaouki, J., Larachi, F., Dudukovic, M. P., 1997. Non-invasive monitoring of multiphase flows. Elsevier.

Chaumat, H., Billet, A. M., Delmas, H., 2007. Hydrodynamics and mass transfer in bubble column: Influence of liquid phase surface tension. Chem. Eng. Sci. 62 (24), 7378–7390.

Chen, B. H., Yang, N. S., 1989. Characteristics of a cocurrent multistage bubble column. Industrial & engineering chemistry research 28 (9), 1405–1410.

Clarke, K. G., 2013. Bioprocess Engineering Principles,solution.pdf. Woodhead Publishing Limited.

Darmana, D., Deen, N. G., Kuipers, J. A. M., Jun 2005. Detailed modeling of hydrodynamics, mass transfer and chemical reactions in a bubble column using a discrete bubble model. Chemical Engineering Science 60 (12), 3383–3404.

Deen, N. G., Mudde, R. F., Kuipers, J. A. M., Zehner, P., Kraume, M., 2000. Bubble Columns. In: Ullmann's Encyclopedia of Industrial Chemistry. Wiley-VCH Verlag GmbH & Co, p. 34.

Dreher, A. J., Krishna, R., sep 2001. Liquid-phase backmixing in bubble columns, structured by introduction of partition plates. Catalysis Today 69 (1-4), 165–170.

Dunn, I. J., Einsele, A., 1975. Oxygen transfer coefficients by the dynamic method. Journal of Applied chemistry and Biotechnology 25 (9), 707–720.

Fischer, F., Hampel, U., 2010. Ultra fast electron beam X-ray computed tomography for two-phase flow measurement. Nucl. Eng. Des. 240 (9), 2254–2259.

Fischer, F., Hoppe, D., Schleicher, E., Mattausch, G., Flaske, H., Bartel, R., Hampel, U., 2008. An ultra fast electron beam x-ray tomography scanner. Meas. Sci. Technol. 19 (9), 094002.

Fortescue, G., Pearson, J. R., 1967. On gas absorption into a turbulent liquid. Chemical Engineering Science 22 (9), 1163–1176.

Gauthier, L., Thibault, J., LeDuy, a., 1991. Measuring kLa with randomly pulsed dynamic method. Biotechnology and bioengineering 37 (9), 889–893.

Heindel, T. J., Gray, J. N., Jensen, T. C., Apr. 2008. An X-ray system for visualizing fluid flows. Flow Meas. Instrum. 19 (2), 67–78.

Höller, V., Radevik, K., Kiwi-Minsker, L., Renken, A., 2001. Bubble Columns Staged with Structured Fibrous Catalytic Layers: Residence Time Distribution and Mass Transfer. Industrial & Engineering Chemistry Research 40 (6), 1575–1579.

Höller, V., Wegricht, D., Kiwi-Minsker, L., Renken, A., 2000. Fibrous structured catalytic beds for three-phase reaction engineering: Hydrodynamics study in staged bubble columns. Catalysis today 60 (1), 51–56.

Hubers, J. L., Striegel, A. C., Heindel, T. J., Gray, J. N., Jensen, T. C., Nov. 2005. X-ray computed tomography in large bubble columns. Chem. Eng. Sci. 60 (22), 6124–6133.

Ito, D., Prasser, H.-M. M., Kikura, H., Aritomi, M., Aug. 2011. Uncertainty and intrusiveness of three-layer wire-mesh sensor. Flow Meas. Instrum. 22 (4), 249–256.

Jain, D., Kuipers, J.A.M., Deen, N. G., Nov 2014. Numerical study of coalescence and breakup in a bubble column using a hybrid volume of fluid and discrete bubble model approach. Chemical Engineering Science 119, 134–146.

Jain, D., Kuipers, J. A. M., Deen, N. G., 2015. Numerical modeling of carbon dioxide chemisorption in sodium hydroxide solution in a micro-structured bubble column. Chem. Eng. Sci. 137, 685–696.

Jain, D., Lau, Y. M., Kuipers, J. A. M., Deen, N. G., 2013. Discrete bubble modeling for a micro-structured bubble column. Chemical Engineering Science 3681.

Kak, A., Slaney, M., 1988. Principles of Computerized Tomographic Imaging. Engineering, 344.

Kantarci, N., Borak, F., Ulgen, K. O., 2005. Bubble column reactors. Process Biochemistry 40 (7), 2263–2283.

Koynov, A., Khinast, J. G., Tryggvason, G., 2005. Mass transfer and chemical reactions in bubble swarms with dynamic interfaces. AIChE Journal 51 (10), 2786–2800.

Lakota, A., Jazbec, M., Levec, J., 2001. Impact of structured packing on bubble column mass transfer characteristics: Part 1. Back mixing in the liquid phase. Acta Chim. Slov 48, 453–468.

Lakota, A., Jazbec, M., Levec, J., 2002. Impact of structured packing on bubble column mass transfer charasteristics. Part 2. Analysis of gas-liquid mass transfer measurements. Acta Chimica Slovenica 49 (3), 587–604.

Lamont, J. C., Scott, D. S., 1970. An eddy cell model of mass transfer into the surface of a turbulent liquid. AIChE Journal 16 (4), 513–519.

Larmour, I. A., Bell, S. E., Saunders, G. C., 2007. Remarkably simple fabrication of superhydrophobic surfaces using electroless galvanic deposition. Angewandte Chemie 119 (10), 1740–1742.

Lau, Y. M., Deen, N. G., Kuipers, J. A. M., May 2013a. Development of an image measurement technique for size distribution in dense bubbly flows. Chemical Engineering Science 94, 20–29.

Lau, Y. M., Sujatha, K. T., Gaeini, M., Deen, N. G., Kuipers, J. A. M., Jul 2013b. Experimental study of the bubble size distribution in a pseudo-2D bubble column. Chemical Engineering Science 98, 203–211.

Lemoine, R., Behkish, A., Morsi, B. I., 2004. Hydrodynamic and Mass-Transfer Characteristics in Organic Liquid Mixtures in a Large-Scale Bubble Column Reactor for the Toluene Oxidation Process. Ind. Eng. Chem. Res. 43 (19), 6195–6212.

Linek, V., Benes, P., Vacek, V., 1989. Dynamic pressure method for kla measurement in large-scale bioreactors. Biotechnology and bioengineering 33 (11), 1406–1412.

Lo, C., 2012. Hydrodynamics , Mixing , and Mass Transfer in Bubble Columns with Internals. Ph.D. thesis, Washington University in St. Louis.

Maceiras, R., Santana, R., Alves, S. S., 2007. Rise velocities and gas-liquid mass transfer of bubbles in organic solutions. Chemical Engineering Science 62 (23), 6747–6753.

Martín, M., Montes, F. J., Galán, M. A., 2009. Mass transfer from oscillating bubbles in bubble column reactors. Chem. Eng. J. 151, 79–88.

Meikap, B. C., Kundu, G., Biswas, M. N., 2001. Prediction of the interfacial area of contact in a variable-area multistage bubble column. Industrial & engineering chemistry research 40 (26), 6194–6200.

Meikap, B. C., Kundu, G., Biswas, M. N., 2002. Prediction of dispersed phase holdup in a modified multi-stage bubble column scrubber. The Canadian Journal of Chemical Engineering 80 (2), 306–312.

Meikap, B. C., Kundu, G., Biswas, M. N., 2004. Mass transfer characteristics of a counter current multi-stage bubble column scrubber. J. Chem. Eng. Jpn. 37 (10), 1185–1193.

Meyer, F., 1994a. Topographic distance and watershed lines. Signal processing 38 (1), 113–125.

Mudde, R. F., 2010. Time-resolved X-ray tomography of a fluidized bed. Powder Technology 199 (1), 55–59.

Otsu, N., 1975. A threshold selection method from gray-level histograms. Automatica 11 (285-296), 23–27.

Öztürk, S. S., Schumpe, a., Deckwer, W.-D., 1987. Organic liquids in a bubble column: Holdups and mass transfer coefficients. AIChE Journal 33 (9), 1473–1480.

Powell, R. L., 2008. Experimental techniques for multiphase flows. Physics of Fluids (1994-present) 20 (4), 40605.

Prasser, H. M., Böttger, A., Zschau, J., 1998. A new electrode-mesh tomograph for gas–liquid flows. Flow Measurement and Instrumentation 9 (2), 111–119.

Prasser, H. M., Scholz, D., Zippe, C., 2001. Bubble size measurement using wire-mesh sensors. Flow Meas. Instrum. 12 (4), 299–312.

Prasser, H.-M. M., Misawa, M., Tiseanu, I., Apr. 2005. Comparison between wire-mesh sensor and ultra-fast X-ray tomograph for an airï£¡water flow in a vertical pipe. Flow Meas. Instrum. 16 (2-3), 73–83.

Prince, M. J., Blanch, H. W., 1990. Bubble coalescence and break-up in air-sparged bubble columns. AIChE Journal 36 (10), 1485–1499.

Rabha, S., Schubert, M., Grugel, F., Banowski, M., Hampel, U., 2015. Visualization and quantitative analysis of dispersive mixing by a helical static mixer in upward co-current gas-liquid flow. Chem. Eng. J. 262, 527–540.

Rabha, S., Schubert, M., Hampel, U., 2013a. Intrinsic flow behavior in a slurry bubble column: A study on the effect of particle size. Chem. Eng. Sci. 93, 401–411.

Rabha, S., Schubert, M., Wagner, M., Lucas, D., Hampel, U., 2013b. Bubble size and radial gas hold-up distributions in a slurry bubble column using ultrafast electron beam X-ray tomography. AIChE J. 59 (5), 1709–1722.

Rollbusch, P., Bothe, M., Becker, M., Ludwig, M., Grünewald, M., Schlüter, M., Franke, R., 2015. Bubble columns operated under industrially relevant conditions - Current understanding of design parameters.

Ruchti, G., Dunn, I., Bourne, J., von Stockar, U., 1985. Practical guidelines for the determination of oxygen transfer coefficients (KLa) with the sulfite oxidation method. The Chemical Engineering Journal 30 (1), 29–38.

Segers, Q. I. E., 2015. Cutting bubbles using wire-mesh structures: direct numerical simulations. Ph.D. thesis, Technische Universiteit Eindhoven.

Segers, Q. I. E., Kuipers, J. A. M., Deen, N. G., 2013. Immersed Boundary Method applied to single phase flow past crossing cylinders. Chem. Eng. Sci. 100, 33–38.

Shah, Y. T., Kelkar, B. G., Godbole, S. P., Deckwer, W.-D., 1982. Design parameters estimations for bubble column reactors. AIChE Journal 28 (3), 353–379.

Shioya, S., Dunn, I., 1978. A Dynamic oxygen transfer coefficient measurement method for column reactors.

Sommerfeld, M., Bourloutski, E., Bröder, D., 2003. Euler/Lagrange calculations of bubbly flows with consideration of bubble coalescence. Canadian Journal of Chemical Engineering 81 (3-4), 508–518.

Sujatha, K. T., Meeusen, B. G. J., Kuipers, J. A. M., Deen, N. G., 2015. Experimental studies of bubbly flow in a pseudo-2D micro-structured bubble column reactor using digital image analysis. Chemical Engineering Science 130, 18–30.

Tang, C., Heindel, T. J., 2004. Time-dependent gas holdup variation in an air-water bubble column. Chemical Engineering Science 59 (3), 623–632.

van Sint Annaland, M., Deen, N. G., Kuipers, J. A. M., 2003. Multi-level modeling of dispersed gas–liquid two-phase flows. Heat and Mass Transfer. Springer, Berlin.

van Sint Annaland, M., Deen, N. G., Kuipers, J. A. M., 2005. Numerical simulation of gas bubbles behaviour using a three-dimensional volume of fluid method. Chem. Eng. Sci. 60 (11), 2999–3011.

Van't Riet, K., 1979. Review of Measuring Methods and Results in Nonviscous Gas-Liquid Mass Transfer in Stirred Vessels. Industrial & Engineering Chemistry Process Design and Development 18 (3), 357–364.

Verma, V., Padding, J. T., Deen, N. G., Kuipers, J., Barthel, F., Bieberle, M., Wagner, M., Hampel, U., 2014. Bubble dynamics in a 3-d gas–solid fluidized bed using ultrafast electron beam x-ray tomography and two-fluid model. AIChE Journal 60 (5), 1632–1644.

Vreman, A. W., 2004. An eddy-viscosity subgrid-scale model for turbulent shear flow: Algebraic theory and applications. Physics of Fluids 16 (10), 3670.

Wangjiraniran, W., Motegi, Y., Richter, S., Kikura, H., Aritomi, M., Yamamoto, K., 2003. Intrusive effect of wire mesh tomography on gas-liquid flow measurement. J. Nucl. Sci. Tech. 40 (11), 932–940.

Westerterp, K. R., Van Swaaij, W. P. M., Beenackers, A., 1987. Chemical reactor design and operation. Vol. 84. Wiley Chichester.

Yang, J. H., Hur, Y. G., Lee, H. T., Yang, J. I., Kim, H. J., Chun, D. H., Park, J. C., Jung, H., Park, S. B., oct 2012. Interaction between partitioning porous plate and rising bubbles in a trayed bubble column. Chemical Engineering Research and Design 90 (10), 1457–1466.

Youssef, A., 2010. Fluid Dynamics and Scale-up of bubble columns with internals. Ph.D. thesis, Washington University in St. Louis.

List of publications

Publications

Thiruvalluvan Sujatha, K., Meeusen, B.G.J., Kuipers, J.A.M., Deen, N.G. Experimental Studies of Bubbly Flow in a Pseudo-2D Micro-Structured Bubble Column Reactor Using Digital Image Analysis. Chemical Engineering Science , Vol. 130, p. 18-30, 2015.

Thiruvalluvan Sujatha, K., Jain, D., Kamath, S., Kuipers, J.A.M., Deen, N.G. Experimental and numerical investigation of a micro-structured bubble column with chemisorption (Submitted for CFD 15 special issue of Chemical Engineering Science).

Thiruvalluvan Sujatha, K., Kamath, S., Kuipers, J.A.M., Deen, N.G. Cutting bubbles in a micro-structured column for dodecane-nitrogen system (To be submitted).

Thiruvalluvan Sujatha, K., Kuipers, J.A.M., Deen, N.G. Absorption of oxygen into water in a micro-structured bubble column reactor (To be submitted).

Thiruvalluvan Sujatha, K., Kuipers, J.A.M., Lau, Y.M., Hampel, U., Barthel, F., Schubert, M., Deen, N.G. Hydrodynamic studies of cutting bubbles in micro-structured square bubble column using ultrafast X-ray tomography (To be submitted).

Lau, Y.M., *Thiruvalluvan Sujatha, K.*, Gaeini, M., Deen, N.G., Kuipers, J.A.M. Experimental Study of the bubble size distribution in a pseudo-2D bubble column. Chemical Engineering Science, Vol. 98, p. 203-211, 2013.

Conference papers & presentations

Thiruvalluvan Sujatha, K., Kuipers, J.A.M., Lau, Y.M., Barthel, F., Hampel, U., Schubert, M., Deen, N.G. Hydrodynamic studies of cutting bubbles in micro-structured square bubble column using ultrafast X-ray tomography 9^{th} International Conference on Multiphase Flow (ICMF 2016), Florence, Italy, 2016.

Thiruvalluvan Sujatha, K., Jain, D., Kamath, S., Kuipers, J.A.M., Deen, N.G. Experimental and numerical investigation of a micro-structured bubble column with chemisorption 11^{th} International Conference on CFD in Oil & Gas, Metallurgical and Process Industries (CFD 2015), Melbourne, Australia, 2015.

Thiruvalluvan Sujatha, K., Kuipers, J.A.M., Deen, N.G. Hydrodynamic studies of bubble cutting in a microstructured bubble column reactor for a dodecane-nitrogen

system. 12^{th} International Conference on Gas-Liquid & Gas-Liquid-Solid Reactor Engineering (GLS12), New York, USA, 2015.

Thiruvalluvan Sujatha, K., Kuipers, J.A.M., Deen, N.G. Absorption of oxygen into water in a micro-structured bubble column reactor. Netherlands Process Technology Symposium (NPS 14), Utrecht, The Netherlands, 2014.

Thiruvalluvan Sujatha, K., Kuipers, J.A.M., Deen, N.G. Experimental studies of bubbly flow in a micro-structured bubble column reactor using digital image analysis. 10^{th} International Conference on CFD in Oil & Gas, Metallurgical and Process Industries (CFD 2014), Trondheim, Norway, 2014.

Thiruvalluvan Sujatha, K., Lau, Y.M., Kuipers, J.A.M., Deen, N.G. Development and application of digital image analysis to gas-liquid flows in a pseudo-2D bubble column. 10th Multiphase flow conference and short course, Dresden, Germany, 2012.

Acknowledgments

> " Life and Time are the world's best teachers. Life teaches us to make good use of Time and Time teaches us the value of Life.
>
> *A.P.J. Abdul Kalam*

The last four years have been truly memorable with colleagues, friends and family providing me their full support in my every small step to reach the finish line. Therefore, many people have contributed either directly or indirectly to the making of this dissertation and I would like to thank them in the following text.

I am highly indebted to both my professors: prof. Niels Deen and prof. Hans Kuipers for trusting and guiding me for the past 4 years on this novel project. Their critical remarks on this thesis and journal/conference articles have made this work achieve its current quality and quantity. I hope I have fulfilled some of your expectations.

I would like to specially thank prof. Hans Kuipers for his patient guidance and sincere feedback as it has enriched my technical and inter-personal skills. I am very thankful for his insight into the research methodology, topics to be investigated and the critical comments on interpretation of results.

I would like to convey my heartfelt gratitude to prof. Niels Deen, my daily supervisor for the past four years. He has been extremely helpful and supportive of all my endeavors during the project. I am very thankful that Niels always made time for impromptu meetings to provide guidance and discussion on problems I faced during the project. Under his guidance, I have developed into an independent researcher who can handle and solve problems confidently. The most important concept, I learned from him about research is to "keep things simple", which helps to provide simple solutions to difficult problems. I have learned quite a lot from him about non-intrusive experimental techniques, which has been applied quite extensively in this thesis.

Then I want to thank Professor Uwe Hampel and dr. Markus Schubert for allowing me to perform experiments at Helmholtz-Zentrum Dresden Rossendorf (HZDR), Germany and to use the ROFEX ultra-fast X-ray tomography scanner facility. The assistance of technicians Frank Barthel and Uwe Sprewitz is highly appreciated as they spent several late evenings to help complete my experiments within our tight schedule. I would also like to thank Yuk Man Lau for his help with X-ray data processing and analysis.

I am very grateful to the technicians Lee McAlpine, Thijs van Moll, Joris and Joost for all the help in building and fixing my experimental setup and the enjoyable conversations. I should mention special thanks to Thijs for his instantaneous help in fixing problems with a big smile. Joris and Joost often helped me troubleshoot small problems encountered during experiments. I also like to thank dr. Fausto Galluci for all the support and advice he provided regarding safety arrangement for experiments.

During my research, a number of students worked on their MSc thesis under my supervision. Their work has been a significant contribution to this project. Therefore I would like to thank Benny Meeusen (tested the experimental setup and performed hydrodynamics and particle image velocimetry experiments), Satish Kamath (assisted in chemisorption experiments to validate the Euler-Lagrange model and performed dodecane-nitrogen experiments), Martin Teley (single bubble cutting experiments in glycerol-air system for hydrophilic and hydrophobic mesh), Michelle Raven (assisted in validation of oxygen sensor) and finally Max Kuiper (evaluated the effect of liquid circulation on bubble cutting and the effect of wire-mesh on liquid mixing).

For three months, Esko Lahdenpera (Lapperenta University, Finland) visited our research group. During these months he worked on a numerical model for reaction in a droplet and I have enjoyed many discussions we had on chemical engineering, numerical modeling, paper & pulp technology.

I would like to thank the secretaries Ada, Judith, Marianne for helping in all the administrative matters at the university.

Just as important as the people mentioned above are those who kept my spirits high during my time at SMR. My officemates Deepak, Yali, Martin, Sushil and Sathish have always maintained a 'gezellig' atmosphere at the office. Thanks to you all for making office hours enjoyable with non-technical and technical discussions. I would like to thank Ramon, Saurish, Shauvik, Alvaro, Mohammad, Lizzy, Lucia, Nhi, Alvaro, Alessandro, Ildefonso, Vincenzo, Arash and all other (former) PhD students and postdocs for making my stay at the group memorable.

I am nothing without my family and friends (Bagesh, Rajesh-Sneha, Lakku-Uma, Mohan, Paula, Theo-Silvia, Sander, Katalin, Salsa friends, AEGEE friends, ...), who have supported me throughout the years.

This list would be incomplete without thanking my wife; Sandhiya, without you my last year of the PhD would have never been so easy and wonderful. Thanks for your patience, love and support.

Krushnathej Thiruvalluvan Sujatha,
Eindhoven, September 2016.

About the author

Krushnathej Thiruvalluvan Sujatha was born on 7th May 1989 in Tiruvallur, India. He completed his high school in St. John's MHSS Babanagar, Chennai, India in 2006. In August 2006, he joined a four-year undergraduate program in Chemical Engineering at Coimbatore Institute of Technology an autonomous institution affiliated to the Anna University. He was awarded the diploma Bachelor of Technology in Chemical Engineering on successful completion of his undergraduate program in April 2010.

In August 2010, Krushnathej started his Master's program at Eindhoven University of Technology in the Chemical Engineering department and specialized in "Process Engineering". He was a recipient of the TU/e Talent Scholarship Program awarded by Eindhoven University of Technology that funded his master's education. He worked on his Master thesis in the Multiphase Reactors group under the supervision of prof. Kuipers and dr. Deen. In April 2012, he defended his Master's thesis titled "CO_2 Chemical Absorption into NaOH (aq) solutions in dense bubbly flow". He did his internship at the Urban Environment and Safety group, TNO, Utrecht from April 2012 - July 2012 on the topic "Thermodynamics of multi-phase multi-component mixtures for safety and risk assessment models". In August 2012, he completed his post-graduation at Eindhoven University of Technology earning the title MSc in Chemical Engineering.

In October 2012, Krushnathej started his PhD project "Cutting Bubbles" under the guidance of prof. Deen and prof. Kuipers in the Multiphase Reactors group at the Eindhoven University of Technology. The research project was funded by a grant from the European Research Council. The results of this research are presented in this dissertation.